Performance of Fluid-Structure Interaction based on Analytical and Computational Techniques

A thesis submitted in fulfilment of the requirements for for the degree of Master of Engineering

Pongpat Thavornpattanapong
BEng

Supervisor: Prof. Jiyuan Tu

Associate Supervisor: Dr. Sherman C.P. Cheung

School of Aerospace, Mechanical and Manufacturing Engineering
RMIT University
March, 2011

to my MOTHER and FATHER with love

Contents

List of Tables

List of Figures

Performance of Fluid-Structure Interaction based on Analytical and Computational Techniques

Pongpat Thavornpattanapong, Bachelor of Engineering
pongpat.thavornpattanapong@rmit.edu.au
RMIT University, 2011

Supervisor: Prof. Jiyuan Tu
Associate Supervisor: Dr. Sherman C.P. Cheung

Abstract

Solving coupling of fluid and solid governing equations in fluid-structure interaction (FSI) is a common computational problem well known to mathematicians, scientists and engineers. Several algorithms exist for solving this problem. However, when the approach for the FSI solution is *Partitioned approach* (i.e., separated solvers for fluid and solid domains), the problem may not be solvable and obtain meaningful results. In fact, it has been shown that the general problem of solving the FSI system with partitioned approach is "Added mass instability", i.e., extremely difficult and (it is believed) inefficient; thus, it is not suitable to be adopted for solving wide range of applications.

It turns out, though, that the time integration schemes used for structural acceleration have a strong impact on the efficiency of solving FSI system of equations. It is found that amount of numerical damping can change the performance considerably. In particular, efficiency of solutions with less numerical damping in structural integration schemes are found to be superior than those with greater numerical damping. It is found out that in some cases, the value of critical relaxation factor can be increased up to approximately 30 percent by varying value of applied numerical damping. This in turn leads to a considerable reduction in computational time. However, the improvement depends largely on the density ratio. The critical

value of relaxation factor becomes almost invariant with the amount of the numerical damping when density ratio is very high. Therefore, the improved efficiency can be negligible in some cases whereby working fluid is much denser than solid. Moreover, it is also discovered that the critical value of relaxation factor can be also influenced by some other factors such as fluid time integration schemes, time step size, and geometric properties.

Although the FSI performance that can be improved by varying numerical damping used in the discretization schemes for structural acceleration, the change in performance is limited, especially when density ratio is quite high. Therefore, it is concluded that only a narrow range of problems can be solved by this technique. To be of practical use, *Artificial compressibility* is introduced for a better efficiency for a wider range of appliations. It is found that this technique can speed up the solution process significantly when compared to the appication of relaxation factor, regardless of the density ratio of fluid and solid.

Thus, we desire to adopt *Artificial compressibility* for solving an realistic engineering application. A study of artherosclerosis in carotid bifurcation is achieved with this technique. Apart from the illustration of the applicability of artificial compressibilty technique, the main goal of solving this particular engineering application is to answer the following questions:

> *What is the influence of the degree of stenosis on mechanical stress experienced in carotid bifurcation? How does the pattern of blood flow change with the presence of stenosis with different sizes? Is there any relationship between blood pressure, strucutural stress and deformation of the lesion?*

From our results, the degree of stenotic plaque can radically change the blood flow pattern and mechanical stress on the apex of stenosis. As a result, this significantly affects wall shear stress and deformation. The relationship among blood pressure, stenotic compression and deformation shows that high level of compression occurs at the stenotic apex, and can potentially be responsible for plaque progression.

Performance of Fluid-Structure Interaction based on Analytical and Computational Techniques

Declaration

I certify that except where due acknowledgement has been made, the work is that of the author alone; the work has not been submitted previously, in whole or in part, to qualify for any other academic award; the content of the thesis is the result of work which has been carried out since the official commencement date of the approved research program; any editorial work, paid or unpaid, carried out by a third party is acknowledged; and, ethics procedures and guidelines have been followed.

Pongpat Thavornpattanapong
September 14, 2011

Acknowledgments

I would like to express my deep-felt gratitude to my advisor, Prof. Jiyuan Tu of School of Aerospace, Mechanical and Manufacturing at Royal Melbourne Institute of Technology at Bundoora,Melbourne, for his advice, encouragement, enduring patience and constant support.

He was never ceasing in his belief in me (though I was often doubting in my own abilities), always providing clear explanations when I was (hopelessly) lost, constantly driving me with energy when I was tired, and always giving me his time, in spite of anything else that was going on. His response to my verbal thanks one day was a very modest, "It's my job." I wish all students the honor and opportunity to experience his ability to perform at that job.

I also wish to thank my secondary supervisor, Dr. Sherman C.P. Cheung of School of Aerospace, Mechanical and Manufacturing at Royal Melbourne Institute of Technology at Bundoora,Melbourne. His suggestions, comments and additional guidance were invaluable to the completion of this work.

Additionally, I want to thank Dr. Jon Watmuff and my colleages at Royal Melbourne Institute of Technology at Bundoora,Melbourne for all their hard work and dedication, providing me the means to complete my degree and prepare for a career as an engineer. This includes (but certainly is not limited to) the following individuals: Dr. Kelvin K.L. Wong, Dr. Sura Tundee, Dr. Zhang Kai, Dr. Jie Yang.

I also want to thank the Commonwealth of Australia, through the Cooperative Research Centre for Advanced Automotive Technology (Project: Developing Numerical Model for Flow-Induced Vibration Excitation Mechanisms towards Virtual Laboratory Simulation,C4-503) for providing funding for conductiong this research.

And finally, I must thank my dear family for putting up with me during the development of this work with continuing, loving support and no complaint.

Pongpat Thavornpattanapong

RMIT University
March 2011

List of Publications

The followings are papers completed during this study of Master degree.

- **P. Thavornpattanapong**, K.K.L. Wong, S.C.P. Cheung and J.Y. Tu, 2011, Mathematical Analysis of Added-Mass Instability in Fluid-Structure Interaction, International journal of mathematics and statistics.(In press, this journal paper is a part of Appendix B)

- **P. Thavornpattanapong**, S.C.P. Cheung, K.K.L. Wong and J.Y. Tu, 2011, Fluid structure interaction applied to carotid bifurcation flow, Journal of Mechanics in Medicine and Biology.(Minor revision, this journal paper is a part of from Chapter 6)

- K.K.L. Wong, **P. Thavornpattanapong**, S. C.P. Cheung, Zhonghua Sun , Stephen Grant Worthley, and J.Y. Tu , 2011, Influence of Calcification Agglomerate on Plaque Vulnerability in Atherosclerotic vessels, Annals of Biomedical Engineering.(Submitted)

- K.K.L. Wong, **P. Thavornpattanapong**, T. Chaichana, Z. Sun, and J.Y. Tu, 2010, Analysis on Intra-aneurysmal Flow Influence By Stenting, The 3rd International Conference on BioMedical Engineering and Informatics (BMEI 2010), Paper ID: P0612, Yantai, China.

Nomenclature

Solid density	ρ_s
Fluid density	ρ_f
Thickness of flexible tube	h_s
Displacement relative to previous mesh location	δ
Mesh stiffness	K_{mesh}
Stiffness exponential constant	C_{stiff}
Displacement at interface	Γ
Displacement at i node (on interface)	d_i
Added-mass operator matrix	M_a
Time	t
Spatial coordinate	x
Fluid load on interface	Γ
Fluid load on interface at pseudo time n	$P^n_{ext,\Gamma}$
Fluid load at node i at pseudo time n	$P^n_{ext,i}$
Structural acceleration	$\ddot{d}$
Structural velocity	$\dot{d}$
Structural displacement	d
Velocity	$\mathbf{v}$
Grid Velocity	$\mathbf{v}_c$
Eigen value of the added-mass operator	μ
Structural displacement	d
Reference radius of flexible cylindrical tube	r
Area	$\mathbf{A}$

Volume	$\mathbf{V}$
Center point of control volume	$\mathbf{P}$
Pseudo time step level (coupling iteration)	m
Physical time step level	n
Pressure	P
Upper limit of expected pressure	P_a
Lower limit of expected pressure	P_b
Young modulus	E
Shear stress modulus	B
Poisson coefficient	ν
Timoshenko shear correction factor	K_T
Speed of sound	c
Growth factor	G
Real part of complex growth factor	$Re(G)$
Imaginary part of complex growth factor	$Im(G)$
Radius of growth factor	R
Stress	τ
Structural mass matrix	$\mathbf{M}$
Structural damping matrix	$\mathbf{C}$
Structural stiffness matrix	$\mathbf{K}$
Structural force matrix	$\mathbf{F}$
Outward-pointing face area vector	S_c
Mass flux through element face	F_c
Element face	f_c

Chapter 1

Introduction

1.1 Background

In past decades, significant improvement in development and use of numerical simulation for solving fluid and solid engineering problems has been achieved. Many specialized techniques (such as turbulent models in fluid mechanics and structural mechanic models for composite material) have been proposed to realistically model complex flows and structural mechanical behaviours. In addition, the advance of computational science has enabled the computer to become more valuable and efficient for analyzing many real world engineering applications. With this tremendous computating power, we reached the stage where not only fluid or solid problems can be numerically solved, but also the interaction between the two states, which are important when it comes to analysing complex phenomenon. The method of solving interaction between fluid and solid is generally called Fluid-Structure Interaction (FSI), which is also known as Flow Induced Vibration Excitation (FIV). These are used in automotive, aerospace and biomedical engineering applications such as hydraulic engine mount, oscillation of rear windshield of the convertible car, vibration of marine riser as well as blood-vessel flow. The important engineering applications which require FSI analysis are

- Automotive engineering: Analysis of airbag deployment (e.g. Sinz and Hermann, 2008), analysis of hydraulic engine mount (e.g. Daneshmand et al., 2005; Shangguan and Lu, 2004), analysis of roof of the convertible car (e.g. Knight et al., 2010), analysis of tyre hydroplaning (e.g. Cho et al., 2006);

- Aerospace engineering: Analysis of wing flutter (e.g. Eloy et al., 2007; Silva and Bartels, 2004; Storti et al., 2009; Dang et al., 2010);

- Biomedical engineering: Analysis of atherosclerosis (e.g. Tang et al., 2008; Tada and Tarbell, 2005; Samuel et al., 2008; Thubrikar and Robicsek, 1995; Lee and Xu, 2002), analysis of heart disease (e.g. Nobili et al., 2008; Lau et al., 2010; Hart et al., 2003; Xia et al., 2009; Hart et al., 2003);

- Civil engineering: Analysis of high rise building (e.g. Braun and Awruch, 2009), analysis of long bridge (e.g. Bai et al., 2010; Sun et al., 2008), analysis of marine riser (e.g. Borazjani et al., 2008; Sagatun et al., 2002; Yamamoto et al., 2004);

In these applications, the most challenging task is to deal with large deformation of solid structures which interact with highly complex flows. A good example is the Tocoma bridge disaster which happened in 1940 as shown in Figure 1.1.

The second example is the large deformation, which occurs due to interaction between organic tissue of human blood vessel and the pressurized blood flow. This can be seen in Figure 1.2

Another important engineering application of FSI is the oscillation of the convertible car roof. The performance of the roof is influenced by FSI between the canopy and flow over the roof. The interaction between the canopy and surrounding flow field is a necessary component of a realistic convertible roof simulation and the ability to solve it is recognized as an important challenge of the automotive research community. The vortical flow surrounding the roof and the dynamics of the roof structure at a specific point of time during simulation is shown in Figure 1.3

Numerical analyses of engineering applications are highly important to industrial success. This is because the interplay between numerical FSI simulation and analysis

Figure 1.1: The collapse of the Tocoma narrow bridge(Hatamura, 1996).

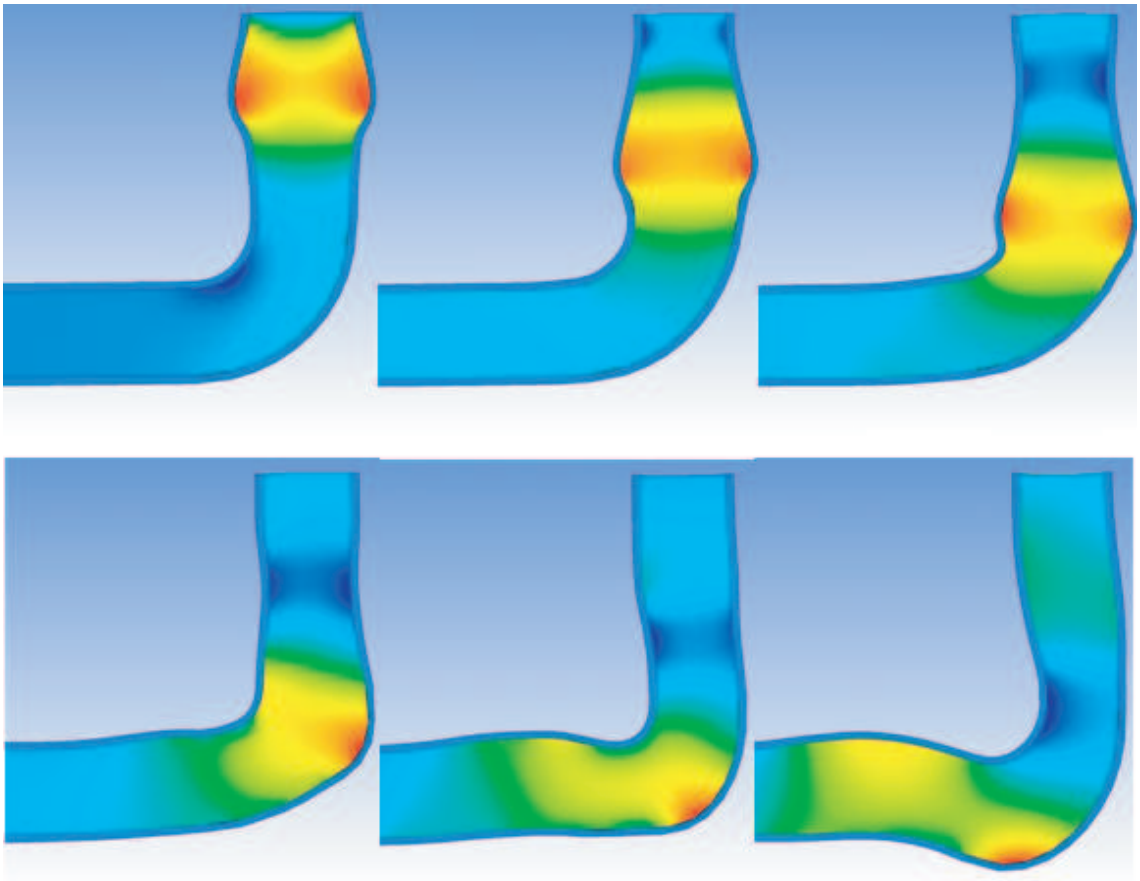

Figure 1.2: Fluid-structure interaction of human blood vessel

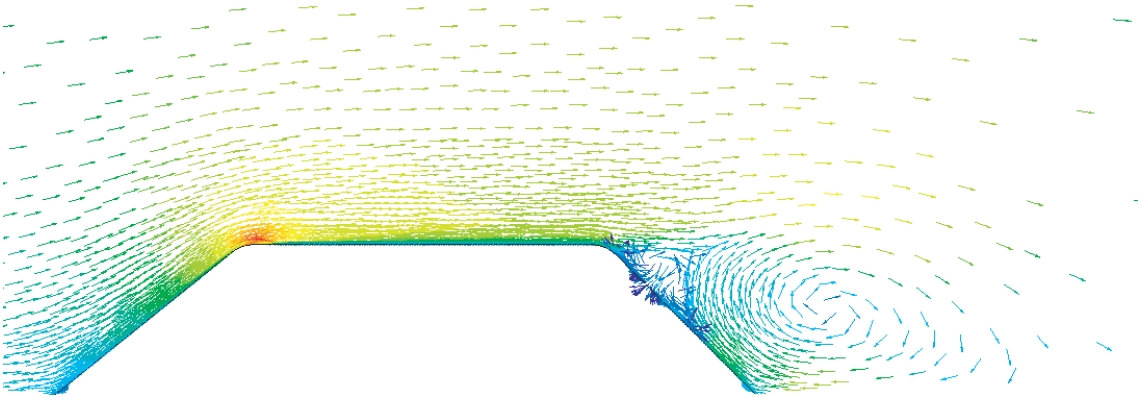

Figure 1.3: Fluid-structure interaction of oscillating rear windshield of convertible car

with the recognition and understanding of new physical phenomena will advance our knowledge of each engineering applications. This will eventually lead to increasingly better engineering products. Based on current technology and realistic expectations of FSI algorithm, a bright future for its applications lies ahead.

It is well known that flow-induced vibration analysis can be done in mainly two approaches, which are "Monolithic" and "Partitioned" approach. Firstly, monolithic approach is sometimes called the "direct" method. It basically solves a system of governing equations for both fluid and solid fields. Although monolithic approach gives strong coupling between the fields, it is impractical for real world applications. This is not only because of its very demanding computational power for solving such a large system of equations but also the need for the development of preconditioning. In this approach, it is also likely that one has to develop new software and solution methods for each coupled application, which is undoubtedly an enormous task to achieve. Secondly, partitioned approach, which is sometimes also called the "iterative" method, is attractive due to the advantage of software modularity, and allowing selection of an appropriate solver among well-established solvers for each field. Within the scope of our study, only the partitioned approach is used. In this approach, fluid solution (such as pressure, velocity and turbulent quantities) is calculated and then transferred to the solid solver. This fluid solution will be used to calculate solid solution (such as displacement, acceleration and stress). After that, the solid solution is transferred back to the fluid solver to start the next calculation. This process is repeated until the convergence of coupling is reached by monitoring the change of displacement and pressure during coupling iteration. Figure 1.4 illustrates the system of calculation in FSI.

In the partitioned approach, fluid is normally modelled using an appropriate Navier-Stokes equation. This equation is then coupled with a dynamic one which governs motion of solid structure. The coupling between a fluid and solid solver is governed by a set of conditions which ensure that the dynamic and kinematic relationship of the two sub-domains is correct.

In FSI simulation, governing equations that are involved can be derived in Lagrangian, Eulerian and Arbitrary Lagrangian-Eulerian (ALE) frame of references.

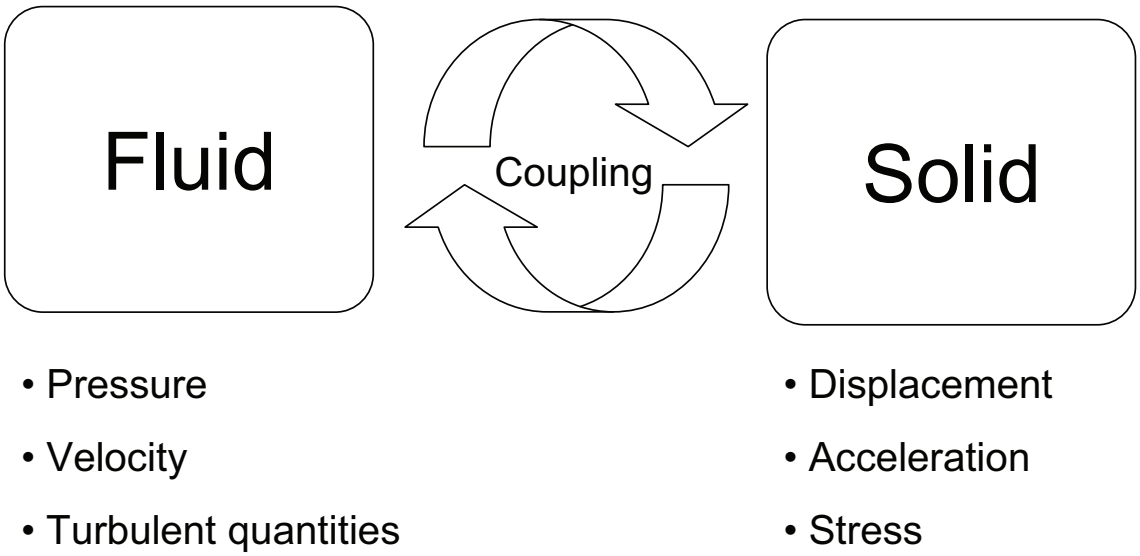

Figure 1.4: Introduction to fluid-structure interaction

Firstly, Lagrangian frame is based on the idea that the material points coincide with the same grid points during the whole motion. This results in no convective effects in calculation. The main advantage is that it provides history-dependent constitutive relations. But its drawback is its inability to follow large distortions of the computational domain without expensive remeshing operations. Eulerian frame, on the other hand, is based on the idea that material point moves with respect to fixed computational grid. This allows large distortions in the continuum motion to exist in computational domain. However, this also leads to a decrease in the accuracy of solution. Thirdly, Arbitrary Lagrangian-Eulerian frame is developed to incorporate the desirable feature of Lagrangian and Eulerian frame. In this frame of reference, the computational grid can either be fixed or moved with continuum. This is the reason why ALE can prove to have large distortion and also the accuracy of solution is not degraded. Therefore, ALE is the frame of reference used to formulate the Navier-stoke equation for solving fluid-structure interaction in CFX, while governing equation for solid domain is formulated in Lagrangian frame.

Despite the advantages of partitioned approach, the efficiency of partitioned approach, especially for applications involving large deformation, must be improved.

This is because of the "added mass effect" instability. This instability usually occurs in problems with large deformation and light weight structure. The main reason why this instability exists in the FSI solution system is the lack of implicitness of FSI solution algorithm of partitioned approach. Information which is used for calculating FSI solution in this approach only comes from the solution of the previous coupling step. This makes the solution explicit and likely to fail. To eliminate this instability, there are many developed techniques available. The most widely used technique is the application of under-relaxation factors. By using this technique, small values of coupling relaxation factors of interface loads must be used. This leads to a significant increase in computational time. Therefore, it is not suitable for industrial usage where time is of importance. Other techniques are "reduced order model" and accelerators (Aitken's or Steepest descent). However, to the best of our knowledge, none of these techniques is used in existing commercial software (such as ANSYS) which can efficiently improve the stability of FSI system for a wide range of engineering applications. Therefore, it is important that an efficient method must be developed so that FSI simulation can be conducted efficiently and conveniently by engineers in various industries.

Four main objectives are accomplished in the thesis. The first aim of the research is to derive theoretical proof of the existence of added-mass instability in fluid structure interaction. This mathematical analysis can also indicate important parameters, which significantly influence the stability of FSI simulation. Secondly, an efficient technique for analysing real world engineering applications is developed based on the information obtained from the mathematical analysis. Thirdly, creation of an add-on code is achieved by constructing a user routine in FORTRAN language to work internally with CFX. This allows an additional capability to the commercial software to handle instability of fluid-structure interaction. The technique implements the idea of artificial compressibility. It is validated with well defined numerical and physical experiments. The last objective of the research is to compare the performance of artificial compressibility to the under-relaxation technique. This is done by considering the time consumption for simulating the same physical phenomenon with different techniques.

The four main objectives of this work can be summarized as follows:

- To provide a theoretical analysis of added-mass instability that focuses on improving the performance of FSI using the partitioned approach;
- To develop an efficient and stable tool to analyze applications that are relevant to FSI;
- To validate the techniques with well defined analytical solutions;
- To evaluate the performance of artifical compressibility and compare it to the under-relaxation technique.

1.2 Outline of thesis

The contents of the remaining six chapters are as follows. In Chapter 2, the basic concepts of FSI are reviewed. The fundamental knowledge of FSI, such as the description of monolithic and partitioned approach as well as frame of reference in continuum are explained. Next, the existence of added-mass instability in partitioned approach is discussed. This is followed by the review of the existing techniques for treating the instability, i.e. the under-relaxation factors and artificial compressibility. The literature review also covers other important topics in FSI such as fixed grid algorithm and automatic remeshing.

Chapter 3 governing equations and discretization schemes are presented. Next, the fundamental conditions for FSI coupling, namely dynamic and kinematic, are discussed, followed by the implementation of artificial compressibility is explained. Then, the description of computing procedure with under-relaxation factors and artificial compressibiltiy are described. In addition, the best practices and general procedure of simulation set up and construction of computation meshes in ANSYS-CFX, which are used throughout this project, are provided.

Chapter 4 addresses the theoretical analysis of added-mass instability in fluid-structure interaction. Firstly, the instability of fluid-structure interaction calculation

that utilizes the generalized-α time integration schemes involving minimum numerical damping and backward Euler schemes are described. Then, a similar analysis of instability of fluid-structure interaction calculation that employs the generalized-α time integration schemes involving minimum numerical damping and backward Euler schemes are discussed.

Chapter 5 covers validations and numerical results that are used to confirm the validity of theoretical analysis provided in Chapter 4. The validations are conducted against well-defined analytical solutions of the wave-propagation along a flexible tube. The numerical results are presented to prove the influence of amplitude decay factor, time step size, density ratio and geometric properties of the FSI problem when the under-relaxation technique is used. This is then followed by the demonstration of the efficiency of the under-relaxation technique and compare its perfomance with the artificial compressibility.

In Chapter 6, the utilization of artificial compressibility to real world engineering applications are presented. A FSI study of atherosclerosis in carotid bifurcation is presented in order to demonstrate the applicability of our method.

Finally, the concluding remarks are made in Chapter 7. Further research direction is also suggested.

1.3 Summary of contributions

- **An intensive investigation of the influence of numerical damping in structural discretization schemes on the instability of FSI coupling by using theoretical and numerical tools**. The outcome of this provides researchers an understanding of the impact of numerical schemes and therefore can help them to conduct FSI numerical experiments in a more efficient way in the future.

- **Performance comparision between under-relaxation technique and artificial compressibility**. It is shown in this work by comparing requried

computational time of each technique that the performance of artificial compressibility is considerably superior than that of under-relaxation technique.

- **A study of fluid-structure interaction of atherosclerosis in carotid bifurcation**. The results of the study can be used as a platform for future work in atherosclerotic researches aiming for thoroughly understanding the complicated process of the disease.

Chapter 2

Literature review

In this chapter, we provide a brief introduction to the theory of fluid-structure interaction(FSI) and necessary prerequsite for the rest of this thesis.

2.1 Frame of reference

Numerical modelling of continuums often involves discretization of these multi-dimensional domains into finite grids. Each grid satisfies the relevant equations governing the kinematics of the continuum. Fundamental to these governing equations are how the continuum distortions are related to the computational grids. The followings are types of reference frame used for describing the kinematic of the continuum:

- Lagrangian frame;
- Eulerian frame;
- Arbitrary Lagrangian-Eulerian frame.

2.1.1 Lagrangian frame

By using Lagrangian frame of reference, computational grids deform completely following the distortion of the continuum material. This implies that the convective

term is negligible (Price, 2006), and the computational demand can be greatly reduced. The reason for this is that a partial derivative with respect to time, which represents the rate of change observed at a grid node in space, becomes zero since the material particle is strictly followed by the computation node. This also links to another advantage which is its ability to do a precise tracking of material position in the continuum. In other words, the exact displacement of the deforming grid is defined. This advantage comes with the inability to handle large material distortion in continuum. Therefore, it is commonly used in solid analysis rather than fluid analysis where large distortion of material in continuum often occurs because fluid particles are not strongly bonded together and tend to move in highly chaotic ways in space. However, it can be useful for describing fluid flows with complicated free surface structure whereby the free surface boundary must be accurately determined. Ramaswamy et al. (1986) modeled fluid domain using this frame of reference such that the computational grid moves with fluid particles. By using this method, large displacement of the mesh can inevitably occur, but this problem can be handled by adopting automatic rezoning techniques. Another difficulty that arises when using Lagrangian frame is that during calculation, the volume of each finite element must be constant since the grids moves with fluid particles and the element boundary changes in a way that fluid inside each element remains unchanged. This constraint can be satified by employing a velocity correction procedure introduced by Chorin (1968). Similar approaches can be found in numerous works (Schneider et al., 1978; Mizukami and Tsuchiya, 1984; Kawahara and Ohmiya, 1985; Kawahara and Ohmiya, 1985; Hirt et al., 1970). Hirt et al. (1970) conducted a computational stability analysis of this correction method and found that timestep size, the surface tension coefficient, fluid density, the volume and width of the surface cells are the important parameters that restrictively determine the success of this method.

2.1.2 Eulerian frame

By using Eulerian frame of reference, computational grids are fixed in space and the continuum deforms with respect to the grids (Shabana, 2008). This means that

the rate of change observed at a fixed grid node in space is nonzero and therefore the convective term cannot be ignored, unlike that in Lagrangian frame (Jacobson, 1999; Donea et al., 2004). Its main advantage is the ability to handle large distortion of material in continuum. This is because the grids remain unchanged throughout calculation and the mass conservation is forced by checking the balance of fluxes at surfaces of each elements (Carlton, 2004). However, its drawback is the inability of material tracking of interfaces and boundary in continuum as mentioned above. Therefore, it is commonly used in pure fluid analysis whereby continuum can be significantly distorted due to strong vortical flow.

2.1.3 Arbitrary Lagrangian-Eulerian frame

In FSI, Arbitrary Lagrangian-Eulerian(ALE) frame of reference has been increasingly popular and detailed infomation can be found in numerous studies (Richter and Wick, 2010; Souli et al., 2000; Zhang and Hisada, 2001; Takashi, 1994; Boffi and Gastaldi, 2004). The ALE computational grids are allowed to move arbitrarily relative to the material deformation. This characteristic gives both the precise material tracking and also the ability to handle large distortion of material in the continuum (Donea et al., 2004). The FSI interface can be tracked accurately whereby the computational nodes move completely with their material particles. It follows that ALE frame is reduced to Lagrangian frame at the interface. On the contrary, the interior computational nodes of fluid domain move arbitrarily according to the mesh adaption methods which will be mentioned later in this chapter. For these interior nodes, the ALE description is used and the grid velocity is taken into account when evaluating the relative fluid velocity at moving nodes. However, in some cases, it is possible that there may be some regions in fluid domain where computational nodes do not move at all. In these regions, it is arguable that the ALE form of the governing equation is reduced to the Eulerian form. The formula of fluid transport equation in the established Eulerian differential form of the mass and momentum conservation equations in fluid dynamics can readily be recast into the ALE form as can be found in the work of Donea et al. (2004). The main disadvantage of ALE

frame is the limitation of having large deformation of structure which leads to folded mesh in fluid mesh while there is no such limitation when using Eulerian frame because the grid is fixed and the deformed FSI interface does not directly attach to the computational nodes as studied by (Richter and Wick, 2010). A number of methods for handling this limitation will be discussed later in this chapter.

2.2 Fluid-structure interaction

There are two main approaches to solving problems in fluid-structure interaction as follows:

- Monotithic approach;
- Partitioned approach.

The classification of analysis types in fluid-structure interaction can be summarized in Figure 2.1.

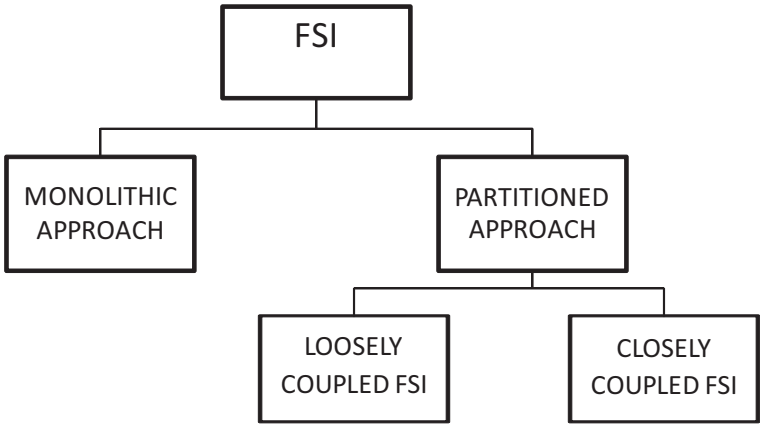

Figure 2.1: Classification of analysis types in fluid-structure interaction.

2.2.1 Monolithic approach

Monolithic approach is sometimes called the "direct" method. Monolithic fluid-structure interaction simulations are solved where both fluid and solid domain are formulated in a single system of equations (Rifai et al., 1999; Bletzinger et al., 2006; Wood et al., 2008). This characteristic of monolithic approach allows the system to be solved without the occurance of added-mass instability since the system is fully coupled and solved in a single iteration loop with consistent time integration schemes for both domains (Bendiksen, 1991; Alonso and Jameson, 1994; Grohmann et al., 1997). In the work done by Blom (1998), a simple piston problem is used to analyse the stability of the coupling. The consistency in time integration in monolithic solver has proven to provide the ability to avoid numerical energy production which may lead to the failure of the solution.

Although monolithic approach gives strong coupling between the fields, it is commonly considered to be impractical for real world applications. This is because it is also unlikely that one has to develop new software and solution methods for each coupled applications, which is undoubtedly an enormous task to be achieved. Moreover, it is not practical for industrial purposes due to time constraints. It also demands enormous computational power for solving such a large system of equations since it has to incorporate the behaviour of both fluid flow and solid structure. Additionally, further development of preconditioning is still needed since the formulation of a single equation system may result in an ill-conditioned system matrix which includes zero entries on the diagonal (Hubner et al., 2004). Further information of monolithic approach can be found in the work by Michler et al. (2004).

2.2.2 Partitioned approach

Another approach to fluid-structure interaction is to use two distinct solvers to model both fluid and solid domains (Matthies et al., 2006). This technique allows the coupling of the fluid and solid solution by applying coupling iterations. Some common

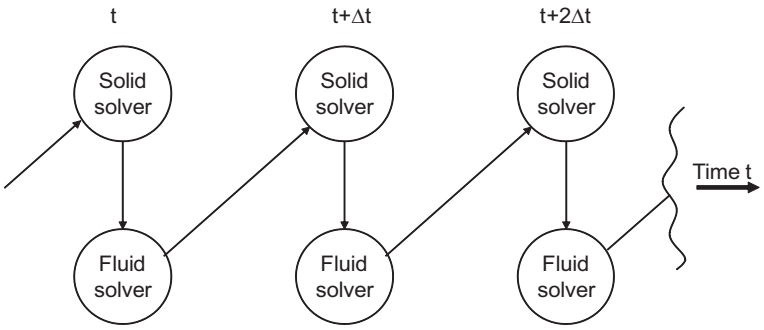

(a) Sequential partitioned approach

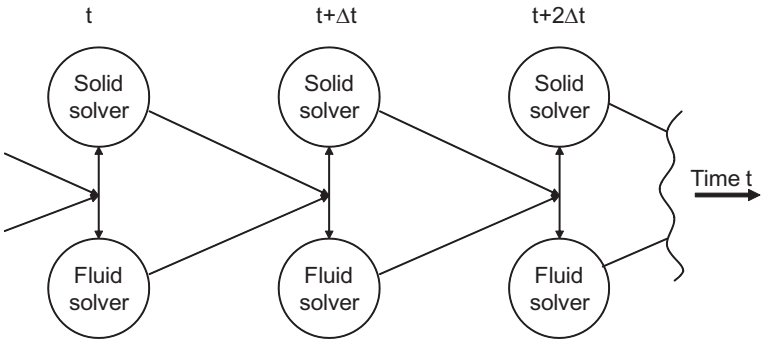

(b) Paralell partitioned approach

Figure 2.2: Diagram of partitioned approach

coupling algorithms were suggested by numerous studies (Piperno et al., 1995; Felippa et al., 2001; Farhat and Lesoinne, 2000) as shown in Figure 2.2. This soluiton coupling allows the reuse of existing codes that have been developed for each field. By coupling two distinct solvers, only interface information is transferred between codes as suggested by Wood et al. (2008). Figure 2.2(a) presents the sequential partitioned approach whereby only one solver is executed at a particular time in sequential manner. Figure 2.2(b) demonstrates the paralell type of partitioned approach where both solvers are run simultaneously. More information about how solid and fluid domains can be coupled in partitioned approach can be found in the work by Felippa et al. (2001). This flexible modularity treatment of partitioned approach is the main reason why it becomes increasingly popular in fluid-structure interaction (Badia et al., 2008). Partitioned approach can be categorized into two main categories, namely the Loosely and Closely coupling.

Loosely coupling

For loosely coupling. the fluid and solid load are transfered only at the end of the solution or each time step (Felippa and Park, 1980; Masud and Hughes, 1997; Farhat and Lesoinne, 2000). This could mean that the convergence of interface load is not ensured. Degroote et al. (2010) suggests that the equilibrium of FSI interface within a time step is not enforced in FSI simulation, which employs loosely coupling. Speed of calculation using this method is very high as there is no iteration of the coupling. However, its accuracy and stability can be very poor if the problem being solved has strong interaction between fluid and solid as suggested by Guidoboni et al. (2009) and l Farhat et al. (2006). This method has been widely used in problems (such as wing fluttering), which involve light compressible flow and stiff solid structure. This is because these problems do not have strong interaction between fluid and solid.

The main disadvantage of loosely coupled is the loss of conservation properties of the FSI continuum. That is, it maintains some conservation properties in only asymptotic sense such as the compatibility of fluid and solid mesh at the interaction interface. Even though the force and displacement between fluid and solid domain can be transferred with a very minimal loss, the energy in solution system and this

method is not perfect energy conservation. Its inability to conserve energy has been proven by various works such as those by Piperno (1997), Piperno (2001), Piperno et al. (1995), Farhat et al. (1998) and Michler et al. (2004). It is believed that the use of different discretization schemes (due to the difference in time and length scale) for fluid and solid domain is the key factor that leads to the failure in conserving energy. It is shown by Michler (2005) that trapezoidal rule can be used in solid analysis to yield a perfectly energy conserved solution but it cannot be used to provide energy conserved FSI. They suggest that this problem can be eliminated by adopting a new discretization scheme which is introduced by van Brummelen et al. (2003) as a time-discontinuous Galerkin discretization. They categorizes this new discretization scheme as conservative type and the trapezoidal rule as non-conservative type. In their work, the coupling between trapezoidal rule for solid solution and the time-discontinuous Galerkin discretization for fluid solution was compared to the coupling, which uses the time-discontinuous Galerkin discretization for both fluid and solid solution, was compared both in term of accuracy and stability. By doing this, it is concluded that the solution of the conservative kind is superior to that of the non-conservative in term of accuracy. They also show that the solution of the non-conservative type eventually results in numerical instability and failure. In particular, the coupling between trapezoidal rule for solid solution and the time-discontinuous Galerkin discretization for fluid solution was compared to the coupling which uses the time-discontinuous Galerkin discretization for both fluid and solid solution. Moreover, it has also been suggested that the error caused by this deficiency of loosely coupled method can be sometime reduced by improving predictors (Piperno, 1997; Piperno, 2001). By using the predictor, the solution of fluid is not calculated based on the old definition of interface boundary but is calculated based on the prediction made by the predictors. These predictors are normally derived from the extrapolation of the interface deformation of previous time steps.

Furthermore, Jaiman (2007) introduces the combined interface boundary condition (CIBC) method for improving the energy conservation property of the loosely coupled method. The key idea of this new method is to correct the interface loads which, in loosely coupled method; some important physical processes are neglected

due to the deficiency of the coupling condition. By correcting these interface loads, the physical processes is introduced back to the solution system explicitly by additional calculation of correction terms. The formula for these correction terms are derived from the calculation of the residual term in local discrete energy-preserving equations. These equations represent the energy conservation between the dynamic and kinematic coupling condition. That is the residual of these equations determine the contribution of the neglected processes by the nature of conventional loosely coupled method. In the same work, the CIBC is validated against analytical solution of the motion of elastic piston in a close domain. The solution of CIBC agrees very well with the analytical one and is superior to that of the conventional loosely coupled method which is very poorly calculated in terms of accuracy.

Closely coupling

For closely coupling, the fluid and solid system are solved separately in succession. The solution of each system is transfered across the interface at the end of a stagger iteration, which is executed many times until convergence is reached (Kalro and Tezduyar, 2000; Tallec and Mouro, 2001; Wang and Yan, 2010). The main advantage of this method is the high accuracy of solution. This method is recommended for solving problems, which have strong interaction between fluid and solid. However, its disadvantage is the slow speed of calculation since many stagger iterations together with small under-relaxation values are needed to achieve convergence (Formaggia et al., 2001; Jarvinen et al., 2001). Moreover, numerical instability can cause the solution to fail if an approprite treatement is not applied.

In closely coupled method, at least two coupling iterations are needed. The explanation to this is that with only one coupling iteration, the numerical error is very small for one solution module only but not for the other solution module and the interface.

The predictors, which are used in loosely coupled method, are also used in closely coupled method but as an initialization of a new coupling iteration and not only a new time step. It is claimed by van Brummelen and de Borst (2005) that the introduction of a predictor into the closely coupled method can reduce the number

of coupling interactions required for reaching convergence for good accuracy. van Brummelen and de Borst (2005) concludes that the numerical effort for solving FSI with the closely coupled method is strongly dependent on the order of extrapolation of the predictor and discretization error. The discretization error is used as a indicator if the iteration of coupling should continue. If the evaluated numerical error is less than the discretization error, then it means that there is no additional error introduced by coupling's numerical instability augmented to the original error from discretization. So, if the order of discretization error is high, then the required number of coupling iteration can be higher. In contrast, the predictors act as a tool to help reduce the initial value of numerical error such that a smaller number of iterations are required for it to become lower than or equal to the value of discretization error. So it is believed that the higher the extrapolation order of the predictor, the smaller the number of coupling iteration needed to be done. In the work of van Brummelen and de Borst (2005), it is specifically determined that the number of coupling iterations is equal to 2 plus the order of predictor minus the order of the discretization error. Although the closely coupled method in theory can allow good stability since it is designed to reduce the numerical error due to coupling but in practice, it is found that the cost of implementing this method is normally exceptionally high. It is claimed by Felippa et al. (2001), "interfield iteration (coupling iteration) generally costs more than cutting the time step to attain the same accuracy level". To the best of our knowledge, we cannot agree with this statement. It has been proven by Causin et al. (2005) both numerically and theoretically that the reduction in time step size may cause a more severe instability. This finding is also confirmed by our results which will be discussed in the later chapters. However, it is possible that the cost of the method can be reduced by applying acceleration such as Krylov, Aitken and Steepest descent.

2.3 Added-mass instability in partitioned approach

In this section, a brief background of added-mass instability in partitioned approach is discussed. Detailed mathematical analysis of this instability can be found in

Chapter 3. We provide some knowledge here to help readers understand its significance to FSI simulation. In partition approach, there are several observations about stability of partitioned approach FSI made by Forster et al. (2007) as follows:

- Stability of FSI solution tends to be highly severe when density ratio between fluid and solid is high;
- The increase in fluid viscosity leads to the decrease in stability. In contrast, the increase in structural stiffness results in more stability;
- Temporal discretisation schemes used for FSI calculation can influence condition of instability;
- The decrease in time step size used for FSI calculation give an earlier occurance of instability.

We emphasize that this instability does not occur because of the large time step size used in calculation, which is the usual problem in CFD and FEA. Rather, small value of time step size causes problem in FSI. This is because small time step size can lead to large eigenvalues of the amplification operator of the explicit step (Forster et al., 2007). This is confirmed by mathematical analysis (Causin et al., 2005). Added-mass stability can have a significant effect on the perfomance of FSI calculation. Computational time is increased significantly if a final solution can reached at all. This is because solution tends to fail and solution on either fluid or solid domain is terminated without reaching a final solution.

2.4 Summary of Existing Techniques for FSI Closely Coupling

2.4.1 Under-relaxation

Under-relaxation technique can be used to enhance stability of solution. It is applied to fluid and structural load transferred across FSI interface. It generally dampens

the interface loads such that stability requirement of both solid and fluid system can be maintained. This variable can be a constanst, which has a value between 0 and 1. Small values of relaxation factor are normally handle severe instability at the beginning of the iteration process but this value can sometimes overkill the problem at a later stage of iteration. This is because severity of instability varies throughout the calculation process. Therefore, adaptive methods for calculating the optimal relaxation factors are introduced. "Aitken's relaxation" and "Steepest decent relaxation" are the two most popular methods for calculating an optimal relaxation factor. In these methods, the relaxation factor is determined based on information of structural displacement from previous stagger iterations. Irons and Tuck (1969) introduced "Aitken accelerator" which is understood to be an adaptive technique for determining the value of a suitable relaxation factor that can be calculated based on solution of two previous coupling iterations. The calculation of Aitken relaxation factor can be achieved after at least two coupling iterations as it requires information about deformation from at least two previous coupling iterations. However, it should be noted that it is possible to use information from more than two previous coupling iterations for the calculation. A formula for Aitken relaxation can be written as

$$\omega_{m+1} = -\omega_m \frac{(r_m)^T (r_m - r_{m-1})}{|r_m - r_{m-1}|^2}, \tag{2.1}$$

where r_m and r_{m-1} is equal to d_m - d_{m-1} and d_{m-1} - d_{m-2} respectively.

The other accelerator called"Steepest descent relaxation" was proposed by Tezduyar et al. (2006). The central idea of this technique is to find the optimum change in deformation at each coupling iteration by using the interface jacobian, J. According to (Kuttler and Wall, 2008), steepest descent relaxation can be expressed as

$$\omega_m = -\frac{\left(r_{m+1}^{n+1}\right)^T \left(r_{m+1}^{n+1}\right)}{\left(r_{m+1}^{n+1}\right)^T J \left(r_{m+1}^{n+1}\right)}, \tag{2.2}$$

where

$$J = \frac{\partial r\left(d_m^{n+1}\right)}{\partial d}.$$

2.4.2 Reduced order models

The reduced order model was used in FSI simulation by numerous researchers such as (Hall et al., 2000; Dowell and Hall, 2001; Willcox and Peraire, 2002) in order to handle added-mass instability problem. By using this model, fluid solutions are calculated with predefined deformation of domain boundary, which is used as FSI interface. This is conducted to collect information about the response of flow field, which corresponds to the prescribed deformation of the FSI interface. The reduced order model is then constructed using this data. The reduced order model and solid solver are then used to calculate for FSI solution. In 2007, Vierendeels et al. (2007) introduced a similar method to improve the efficiency of partitioned approach FSI. In this model, both fluid and solid solver are utilized to generate solution for fluid and solid domain respectively. The reduced order model is used as a middleware which help stabilize the coupling between fluid and solid solvers. The main task of this middleware is to approximate the Jacobian of fluid and solid solver by using least-squares models. The information used for constructing this models are the solid and fluid solution that are obtained in the previous iterations. Recently, Wang and Yan (2010) also presented sensitivity analysis and verificaton of the reduced order model by comparing numerical results by using the reduced order model and a physical experiment. Without detailed information of this reduced order model, the procedure can be summarized as shown by Figure 2.3 according to Degroote et al. (2008).

2.4.3 Artificial compressibility

Artificial compressibility was first used in numerical simulation by Chorin (1967) to relax coupling of continuity and momentum equations for solving incompressible flow. It is a numerical manipulation for improving coupling between momentum and continuity equation, which leads to the improvement of convergence rate of

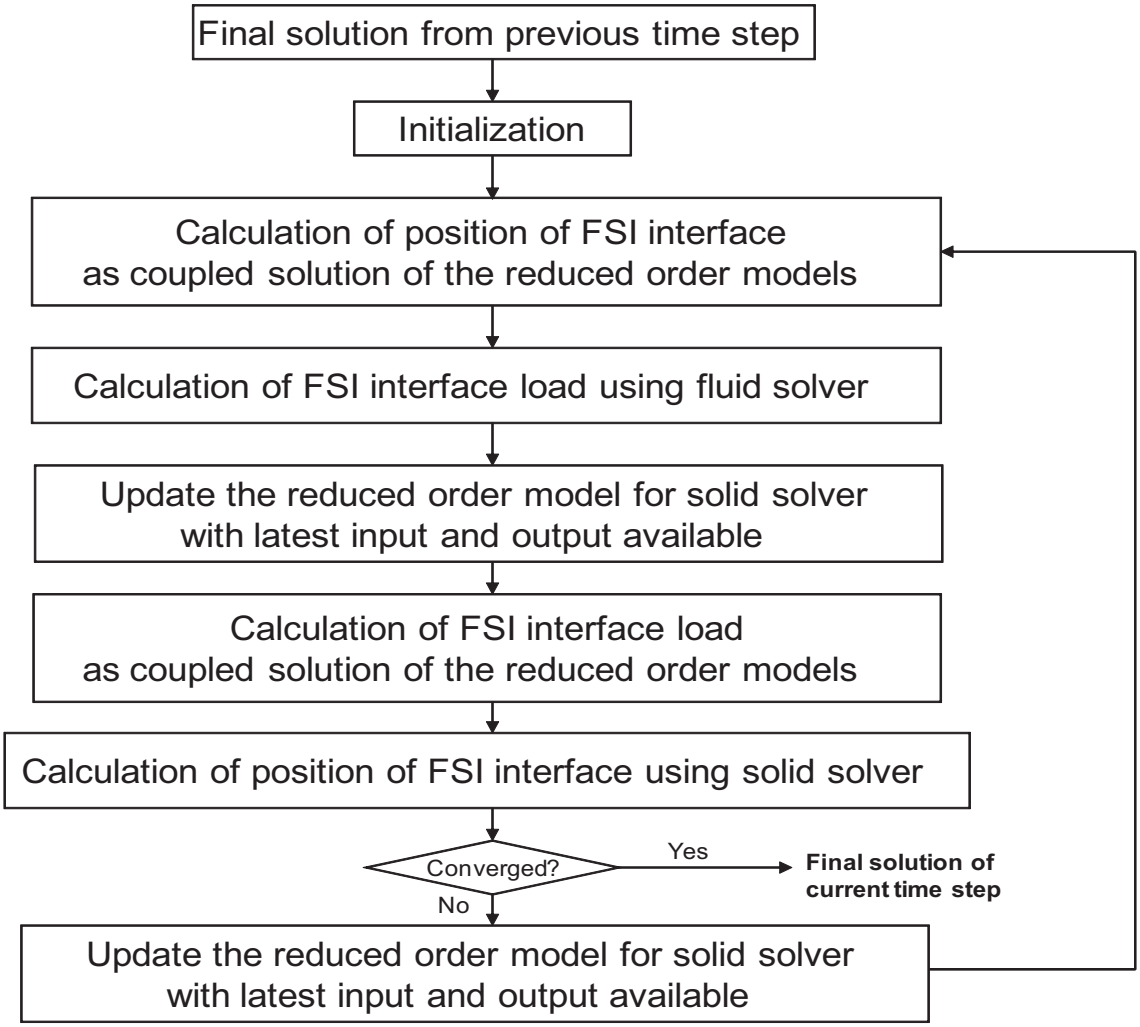

Figure 2.3: Procedure of reduced order models for fluid-structure interaction

solution (Rogers et al., 1987; Carter and Baker, 1991; Peyret, 1976; Merkle and Athavale, 1987). In 2001, this technique is applied to stabilized coupling between fluid and solid equations (Raback et al., 2001). Recently, the so-called "Interface artificial compressibility" was introduced by Degroote et al. (2009), where the artificial term is applied to interface elements. It has been proved by the author that this technique can stabilize the severe instability of FSI coupling. The main idea of the method lies in the introduction of artificial compressibility into equations of motion in the way that the final results are not affected by this additional term. The interface artificial compressibility is modeled as a source term in continuity equation in order to account for position of interface implicitly.

2.5 Methods for computatonal mesh in FSI

Meshing is an important issue in FSI as it has to deal with the movement of the interface especially in problems with large deformation. For the completeness of this review, existing methods for calculating computational mesh for fluid-structure interaction simulation are discussed in this section.

2.5.1 Fixed grid algorithm

Fixed grid algorithms for fluid domain in FSI are very attractive and have been widely used in recent years (Hieber and Koumoutsakos, 2008; Wall, Gerstenberger, Gamnitzer, Forster and Ramm, 2006; Gerstenberger and Wall, 2008; Peskin, 2002). This is mainly because fixed grid algorithms eliminate the need for using remeshing, mesh smoothing for handling large deformation, which is common in FSI. Moreover, there is no need for the calulation of mesh velocity since governing equation is described in Eulerian frame of reference when using fixed grid algorithms. Its advantages mentioned above can lead to a significant reduction in computational cost. However, the main drawback of fixed grid algorithm is the low resolution of result near the boundary of interaction between fluid and solid. The methods used for treating this disadvantage of fixed grid algorithm are:

- Immerse boundary method;
- Chimera method;
- Extended Finite Element Method coupled with Lagrange Multiplier (XFEM/LM).

Immersed boundary method

A fully fixed grid schemes such as the immersed boundary method (IBM) employs a direct structural boundary representation over an Eulerian fluid mesh without recourse to remeshing (Hieber and Koumoutsakos, 2008; Peskin, 2002; Zhang et al., 2004). The structure is treated as some form of fictitious fluid domain which deforms according to the surrounding fluid velocity. This is implemented by interpolating the velocity of surrounding fluid nodes to the structural nodes (Wall, Gerstenberger, Gamnitzer, Forster and Ramm, 2006). Meanwhile, the structural effects on the fluid is realized by spreading the Lagrangian elastic forces of the structure in the form of additional body forces to neighbouring fluid nodes. Both these interactions between Lagrangian and Eulerian variables are implemented by employing interesting properties of the Dirac delta functions. In order to numerically implement the scheme, smooth functions to mimic the properties of dirac delta functions are necessary, leading to the concept of bounded support to efficiently define the extent of influence for each nodal variable.

The spreading of the structural forcing function indirectly smears the boundary of the fluid-structure interface. This limits spatial accuracy of the IBM to its mesh-width and its inability to accurately capture sharp interfaces. Furthermore, without structural position *a priori*, accurate resolution of boundary layers is also a concern. An immersed interface method and adaptive mesh refinement schemes have been proposed to overcome these drawbacks (Peskin, 2002).

Chimera method

Wall, Gerstenberger, Gamnitzer, Forster and Ramm (2006) used the Chimera method, which was introduced by Steger et al. (1983), for solving problems in FSI.

Numerous studies have been conducted to improve this method (Brezzi et al., 2001; Glowinski et al., 2005; Peterson, 1999). Fundamentally, the fluid domain is decomposed to a background Eulerian fluid domain and a ALE fluid subdomain, which overlapped each other. The background Eulerian fluid domain does not extend to the structural boundary, while the ALE fluid subdomain is a deformable fluid subdomain that is attached to the solid domain at interface. This means the ALE fluid subdomain follows the structural movement in order to a local resolution at interface of interaction. Meanwhile, the information between the Eulerian and ALE fluid subdomains are driven by applying Dirichlet and Neumann boundary conditions through interpolation and iteration process.

Extended finite element method coupled with lagrange multiplier

Another fully fixed grid approach include an extended Finite Element Method coupled with Lagrange Multiplier (XFEM/LM) technique proposed by Wall, Gerstenberger, Gamnitzer, Forster and Ramm (2006) and Gerstenberger and Wall (2008). Employing an enrichment jump shape function to capture variable discontinuity, XFEM enables separation of the Eulerian fluid domain to its physical and non-physical subdomains across an interface, allowing more accurate treatment of the interface. The interface grids are free to move and can be coupled to another moving domain. The compatibility between the generally non-matching 3-field grids (physical fluid domain, moving and interface domains) are achieved by applying a lagrange multiplier technique. The scheme can be enhanced by introducing adaptive grid refinement, driven by either heuristic or error indicators, to better capture flow near the interface. However, to efficiently capture boundary layers, the moving domain could also be set to consist of an ALE fluid subdomain coupled to the Lagrangian structural domain. Unlike Chimera schemes, there is no overlap of fluid subdomains and hence open to both partitioned and monolithic solving.

2.5.2 Moving mesh

In fluid-structure interaction, moving mesh is often used to handle deformation of FSI interface. It is important to note that the movement of deforming grid should satisfy "Geometric conservation law" (Lesoinne and Farhat, 1996; Koobus and Farhat, 1999; Guillard and Farhat, 2000; C. Farhat and Grandmont, 2001). The principle statement of this law is that the volume which is swept by interface must be equal to the change in volume of the element that experience the sweep of interface. This law mainly influences the way, which mesh velocity in moving grid domain is calculated. The mesh velocity is usually calculated using first order time integration scheme, which does not always satisfy this law (Donea et al., 2004). Even though the geometric conservation law is believed to be the drive for solution modelled in ALE frame of reference (C. Farhat and Grandmont, 2001) but it has been controversial to determine if this law is essential to calculating moving mesh (Guillard and Farhat, 2000).

Up to date, there are several methods of governing moving mesh. Spring analogy method was introduced by Batina (1989) which was generally used for unstructured meshes only before it was improved by Robinson et al. (1991) for dealing with structured meshes. Despite its ability to handle considerably large deformation, it is often considered computationaly expensive when used for large mesh sizes. In this method, the movement of the nodes are determined by solving an elliptic grid generator iteratively. Later, a simple algebraic shearing technique was proposed by Schuster et al. (1990) which recalculates movement of nodes along nodes lines that are normal to FSI interface. This technique is quite limited as it cannot deal with complex geometries and large deformation. Eriksson (1982) introduced a three stage transfinite interpolation (TFI) method which can only be used for single block mesh before it was improved in the work done by Hartwich and Agrawal (1997). The TFI method was combined with spring analogy method such that the movement of the interface nodes is done by spring analogy while that of interior nodes is done by TFI.

2.5.3 Automatic remeshing

In some FSI problems, the automatic remeshing of compuational domain is required due to excessively large deformation, which cannot be handled by using mesh moving methods such as the spring analogy method. However, it is common that automatic remeshing is used in conjunction with a mesh movement method. By doing this, computational cost for remeshing can be minimized because remeshing will only be executed when quality of computational elements become lower than an acceptable level. The computational cost for remeshing can be expensive because remeshing generally requires generation of totally new mesh and then mapping the solution from the previous mesh onto it. Skewness and aspect ratio can be used as initiators of the remeshing process (*ANSYS Inc. 2009. ANSYS CFX-Solver Theory Guide*, n.d.).

2.6 Summary and concluding remarks

In this chapter, some important terminologies and techniques used in the field of FSI are discussed. From the best of the author's knowledge, The implementation of most of the existing techniques requires intensive modifications or even cannot be done at all in some commercial software. This leaves us with two most obvious choices, which are under-relaxation technique and artificial compressibility, for dealing the instability. Firstly, under-relaxation technique is commonly used in most FSI software but its efficiency is not good for solving most engineering applications. Secondly, artificial compressiblity is a quite simple technique to be applied in any CFD codes. Therefore, these two techniques are choosen for this work for performance comparison both theoretically and numerically in later chapters.

Chapter 3

Methodology

In this chapter, we will discuss our strategy and method to obtain numerical results. Governing equations for fluid and structural mechanics is discussed. Discritization for the governing equations gives the underlining method of solving these governing equations. The procedure for calculating the fluid strucuture interaction is provided. We also discuss the construction and set up for meshing.

3.1 Governing equations

3.1.1 Fluid governing equation

Fluid governing equations consist of the following equations:

- Continuity equation: conservation of mass;
- Momentum equaton: conservation of momentum;
- Energy equation: conservation of energy.

Continuity equation

The continuity equation is based on the idea that any mass in the system has to be conserved. In other words, matter can neither be created or destroyed. This means

that the rate of change of mass within the control volume is equivalent to the mass flux crossing the surface S of volume V. After some mathematical manipulations, a general form of continuity equation in the Eulerian frame can be written as

$$\frac{\partial \rho}{\partial t} + \nabla \cdot (\rho \mathbf{v}) = 0, \tag{3.1}$$

where ρ is density, t is time and $\mathbf{v}$ is velocity.

The continuity equation is reformulated in ALE reference frame. It can be written as

$$\frac{\partial \rho}{\partial t} + \nabla \cdot (\rho(\mathbf{v} - \mathbf{v}_c)) = 0, \tag{3.2}$$

$$\frac{\partial \rho}{\partial t} + \nabla \cdot \rho(\mathbf{v} - \mathbf{v}_c) = 0, \tag{3.3}$$

where $\mathbf{v}_c$ is grid velocity.

Momentum equation

The momentum equation can be formulated based on a physical principle that momentum in the system has to be conserved. A general form of momentum equation in the Eulerian frame can be written as

$$\rho \frac{\partial \mathbf{v}}{\partial t} + \rho \left(\mathbf{v} \cdot \nabla\right) \mathbf{v} = \nabla \cdot (\rho \Upsilon \nabla \mathbf{v}), \tag{3.4}$$

where Υ is diffusivity.

The momentum equation is reformulated in the ALE reference frame. It can be written as

$$\rho \frac{\partial \mathbf{v}}{\partial t} + \rho \left([\mathbf{v} - \mathbf{v}_c] \cdot \nabla\right) \mathbf{v} = \nabla \cdot (\rho \Upsilon \nabla \mathbf{v}). \tag{3.5}$$

Energy equation

The energy equation can be formulated based on a physical principle that energy in the system has to be conserved. A general form of energy equation in Eulerian frame can be written as

$$\rho\frac{\partial \mathbf{E}}{\partial t} + \rho\left(\mathbf{v}\cdot\nabla\right)\mathbf{E} = \nabla\cdot(\rho\Upsilon\nabla\mathbf{E}), \tag{3.6}$$

where $\mathbf{E}$ is energy.

The energy equation is reformulated in the ALE reference frame. It can be written as

$$\rho\frac{\partial \mathbf{E}}{\partial t} + \rho\left([\mathbf{v}-\mathbf{v}_c]\cdot\nabla\right)\mathbf{E} = \nabla\cdot(\rho\Upsilon\nabla\mathbf{E}). \tag{3.7}$$

3.1.2 Solid governing equation

The governing equation for solid domain is formulated in the Largrangian reference frame. It can be written as

$$\mathbf{M}\ddot{d} + \mathbf{C}\dot{d} + \mathbf{K}d = \mathbf{F}, \tag{3.8}$$

where d is displacement, $\mathbf{M}$ is mass, $\mathbf{C}$ is damping, $\mathbf{K}$ is stiffness and $\mathbf{F}$ is force.

3.2 Discretization for governing equations

In this section, discretization schemes used in calculation of both fluid and solid solution will be discussed.

3.2.1 Discretization for fluid governing equations

We start with a generic form of fluid governing equation in the ALE frame of reference which is written as

$$\underbrace{\frac{\partial \rho\phi}{\partial t}}_{\text{Temporal term}} + \underbrace{\nabla \cdot \left(\rho \left[\mathbf{v} - \mathbf{v}_c\right] \phi\right)}_{\text{Convection term}} - \underbrace{\nabla \cdot \left(\rho \Upsilon_\phi \nabla \phi\right)}_{\text{Disffusion term}} = \underbrace{S_\phi \left(\phi\right)}_{\text{Source term}} , \tag{3.9}$$

where ϕ is a transport variable, Υ_ϕ is diffusivity, S_ϕ is a source term.

In finite volume method, it is required that the governing equation is satisfied over control volume $\mathbf{V_P}$ around point $\mathbf{P}$. Therefore, it can be rewritten in the intergral form as

$$\int_t^{t+\triangle t} \left\{ \underbrace{\frac{\partial}{\partial t} \int_{\mathbf{V_P}} \rho\phi d\mathbf{V_P}}_{\text{Temporal term}} + \underbrace{\int_{\mathbf{V_P}} \nabla \cdot \left(\rho \left[\mathbf{v} - \mathbf{v}_c\right] \phi d\mathbf{V_P}\right.}_{\text{Convection term}} - \underbrace{\int_{\mathbf{V_P}} \nabla \cdot \left(\rho \Upsilon_\phi \nabla \phi\right) d\mathbf{V_P}}_{\text{Disffusion term}} \right\}$$
$$= \int_t^{t+\triangle t} \left\{ \underbrace{\int_{\mathbf{V_P}} S_\phi \left(\phi\right) d\mathbf{V_P}}_{\text{Source term}} \right\} \tag{3.10}$$

The following discretization schemes used for each term in transport equation of fluid are presented.

Temporal term

- **First order backward Euler scheme.** By using this scheme, the discretized temporal term can be written as

$$\frac{\partial}{\partial t} \int_{\mathbf{V_P}} \rho\phi d\mathbf{V_P} = \mathbf{V_P} \left(\frac{\rho^{n+1}\phi^{n+1} - \rho^n \phi^n}{\triangle t} \right), \tag{3.11}$$

  where superscript n+1 and n denote time level n+1 and n respectively.

- **Second order backward Euler scheme.** By using this scheme, the discretized temporal term can be written as

$$\frac{\partial}{\partial t}\int_{\mathbf{V_P}} \rho\phi d\mathbf{V_P} = \mathbf{V_P}\left(\frac{3\left(\rho^{n+1}\phi^{n+1}\right) - 4\left(\rho^{n}\phi^{n}\right) + \left(\rho^{n-1}\phi^{n-1}\right)}{2\triangle t}\right). \tag{3.12}$$

Convection term

The convection term can be put into discretized form by using the Gauss's theorem as

$$\begin{aligned}\int_{\mathbf{V_P}} \nabla\cdot\left(\rho\left[\mathbf{v}-\mathbf{v}_c\right]\phi\right) d\mathbf{V_P} &= \sum_{f_c} S_c\left(\rho\left[\mathbf{v}-\mathbf{v}_c\right]\phi\right)_{f_c} \\ &= \sum_{f_c} S_c\left(\rho\left[\mathbf{v}-\mathbf{v}_c\right]\right)_{f_c}\phi_{f_c} \\ &= \sum_{f_c} F_c\phi_{f_c}. \end{aligned} \tag{3.13}$$

Note that S_c and F_c are the outward-pointing face area vector and mass flux through element face. The convection term can be calculated if the flux value on surface of element is known by simple interpolation. The subscript f_c denotes the element face. Now, variable ϕ_{f_c} is the only unknown left before calculation of convection term can be achieved. Therefore, the main purpose of the convection differencing scheme is to evaluate ϕ_{f_c} on faces of computational elements by using the value of ϕ at the center of elements. The followings are convection differencing schemes available in CFX.

- **First order upwind differencing scheme**.

$$\phi_{f_c} = \begin{cases} \phi_{f_c} = \phi_P \text{ if } F_c \geq 0 \\ \phi_{f_c} = \phi_P \text{ if } F_c < 0 \end{cases} \tag{3.14}$$

- **Central differencing scheme**

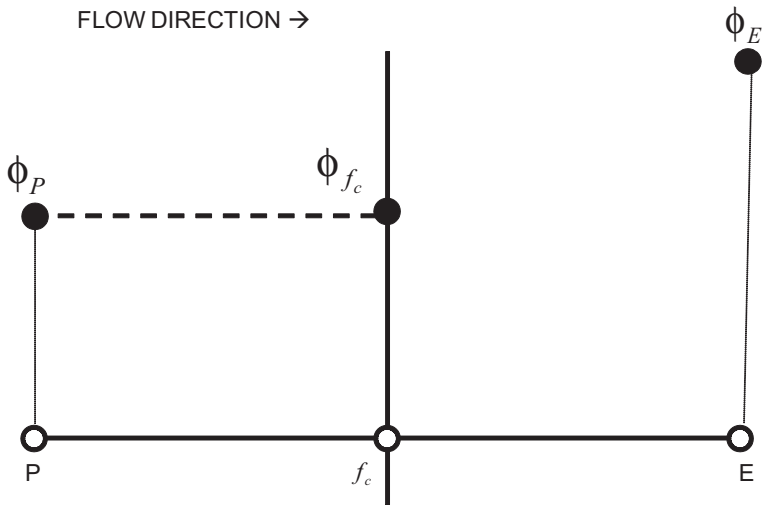

Figure 3.1: Interpolation using upwind differencing scheme when F_c is greater or equal to 0.

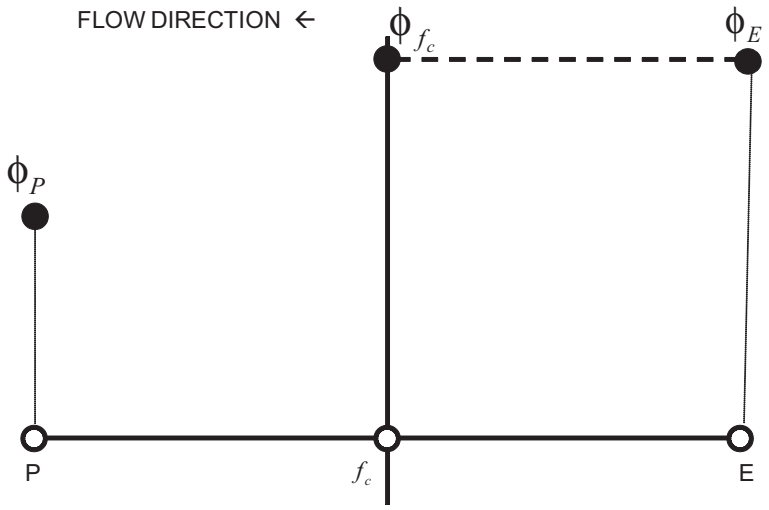

Figure 3.2: Interpolation using upwind differencing scheme when F_c is less than 0.

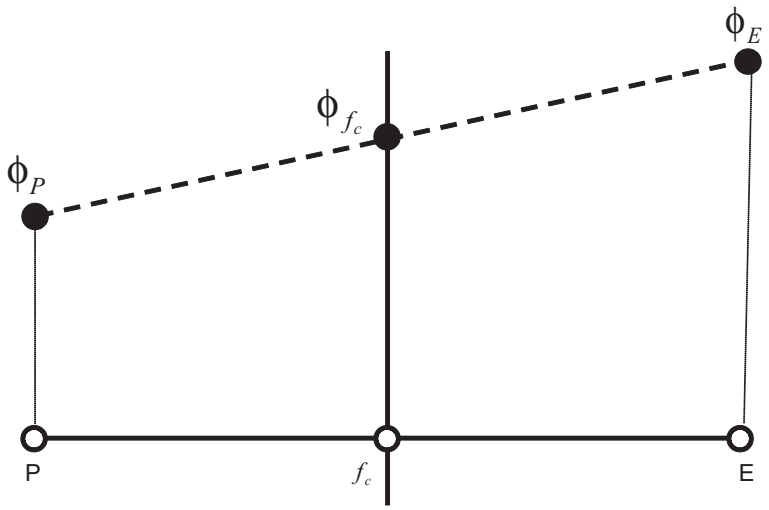

Figure 3.3: Interpolation using central differencing scheme

$$\phi_{f_c} = f_{intp}\phi_P + (1 - f_{intp})\,\phi_E. \tag{3.15}$$

The interpolation factor, f_{intp} can be estimated as

$$f_{intp} = \frac{\overline{f_cE}}{\overline{PE}}. \tag{3.16}$$

Note that $\overline{f_cE}$ and $\overline{PE}$ are the distances from f_c to E and P to E, respectively.

- **High resolution scheme or blended differencing scheme**

$$\phi_{f_c} = (1 - \eta)\,(\phi_{f_c})_{UD} + \eta\,(\phi_{f_c})_{CD}\,. \tag{3.17}$$

Note that $(\phi_{f_c})_{UD}$ and $(\phi_{f_c})_{CD}$ are the values interpolated by the upwind and central differencing scheme respectively.

Although the solution tends to be stable when using the upwind differencing scheme, the level of accuracy is usually decreased. This is mainly because numerical diffusion is introduced to the system by the biased nature of the scheme. In contrast,

the central differencing scheme is less biased in nature, which provides a second order of accuracy at the expense of stability. Therefore, the use of blended differencing scheme is introduced to preserve both stability and accuracy of solution. It is a combination of upwind and central differencing scheme, where the contribution of upwind and central differencing scheme is determined by η. The Blended differencing scheme reduces to upwind differencing scheme when η is chosen to be zero. It also reduces to central differencing scheme when η is chosen to be unity.

Diffusion term

The diffusion term can be put into discretized form by using the Guass's theorem as

$$\begin{aligned}\int_{\mathbf{V_P}} \nabla \cdot (\rho \Upsilon_\phi \nabla \phi)\, d\mathbf{V_P} &= \sum_{f_c} S_c \left(\rho \Upsilon_\phi \nabla \phi\right)_{f_c} \\ &= \sum_{f_c} \left(\rho \Upsilon_\phi\right)_{f_c} S_c \left(\nabla \phi\right)_{f_c}. \end{aligned} \tag{3.18}$$

To be able to calculate diffusion term, the most important task is to correctly estimate $\left(\nabla \phi\right)_{f_c}$. Here,

$$\left(\nabla \phi\right)_{f_c} = \left(\frac{\partial \phi}{\partial x}\right)_{f_c} + \left(\frac{\partial \phi}{\partial y}\right)_{f_c} + \left(\frac{\partial \phi}{\partial z}\right)_{f_c}, \tag{3.19}$$

$$\begin{aligned}\left(\frac{\partial \phi}{\partial x}\right)_{f_c} &= \sum_{nd} \left(\frac{\partial N_{nd}}{\partial x}\right)_{f_c} \phi_{nd}, \\ \left(\frac{\partial \phi}{\partial y}\right)_{f_c} &= \sum_{nd} \left(\frac{\partial N_{nd}}{\partial y}\right)_{f_c} \phi_{nd}. \\ \left(\frac{\partial \phi}{\partial z}\right)_{f_c} &= \sum_{nd} \left(\frac{\partial N_{nd}}{\partial z}\right)_{f_c} \phi_{nd}. \end{aligned} \tag{3.20}$$

Note that formula of shape function N_{nd} depends on shape of computational element being considered during calculation (*ANSYS Inc. 2009. ANSYS CFX-Solver Theory Guide*, n.d.).

Source term

A simple linearlization is applied to discretize source term in fluid transport equation. As suggested by (Patankar, 1980), the discretized source term can be written as

$$\int_{\mathbf{V_P}} S_\phi\left(\phi\right) d\mathbf{V_P} = S_u \mathbf{V_P} + S_P \mathbf{V_P} \phi_\mathbf{P}. \tag{3.21}$$

Interface fluid acceleration

The backward Euler is used for the discretization of fluid acceleration. The first order backward Euler can be written as

$$\frac{\mathbf{v}^{n+1} - \mathbf{v}^n}{\triangle t} = \dot{\mathbf{v}}^{n+1}, \tag{3.22}$$

while the second order backward Euler can be put as

$$\frac{\mathbf{v}^{n+1} - \mathbf{v}^n}{\triangle t} = \frac{1}{3}\frac{\mathbf{v}^n - \mathbf{v}^{n-1}}{\triangle t} + \frac{2}{3}\dot{\mathbf{v}}^{n+1}. \tag{3.23}$$

In this paper, only the zeroth order structural predictor is used in order to estimate the fluid deformation corresponding to structural displacement of previous time step d^n.

The structural predictor can be written as

$$d_{\Gamma,P}^{n+1} = d_\Gamma^n. \tag{3.24}$$

3.2.2 Discretization for solid governing equation

The nonlinear version of the generalized-α time integration scheme, which was introduced by (Chung and Hulbert, 1993), can be used for discretization of solid governing equation as mentioned by (Bathe, 1996). The method assumes that

$$\dot{d}^{n+1} = \dot{d}^{n} + \left[(1-\delta)\, \ddot{d}^{n} + \delta \ddot{d}^{n+1} \right] \triangle t, \tag{3.25}$$

$$d^{n+1} = d^{n} + \dot{d}^{n} \triangle t + \left[\left(\frac{1}{2} - \alpha \right) \ddot{d}^{n} + \alpha \ddot{d}^{n+1} \right] \triangle t^2. \tag{3.26}$$

According to (*ANSYS Inc. 2009. ANSYS CFX-Solver Theory Guide*, n.d.), after some mathematical manipulations, equations (3.25) and (3.26) can be recast in equations (3.27) and (3.28) respectively as

$$\dot{d}^{n+1} = \dot{d}^{n} + \triangle t\, (1-\delta)\, \ddot{d}^{n} + \triangle t \delta \ddot{d}^{n+1}, \tag{3.27}$$

$$\ddot{d}^{n+1} = \frac{1}{\alpha \triangle t^2} \left(d^{n+1} + d^{n} \right) - \frac{1}{\alpha \triangle t} \dot{d}^{n} - \left(\frac{1}{2\alpha} - 1 \right) \ddot{d}^{n}. \tag{3.28}$$

The value of structural displacement, velocity and acceleration is interpolated between time level as

$$\ddot{d}^{n+1,\alpha} = (1-\alpha_m)\, \ddot{d}^{n+1} + \alpha_m \ddot{d}^{n}, \tag{3.29}$$

$$\dot{d}^{n+1,\alpha} = (1-\alpha_f)\, \dot{d}^{n+1} + \alpha_f \dot{d}^{n}, \tag{3.30}$$

$$d^{n+1,\alpha} = (1-\alpha_f)\, d^{n+1} + \alpha_f d^{n}. \tag{3.31}$$

By using the equations for $\ddot{d}^{n+1}$ and $\dot{d}^{n+1}$, the discretized solid governing equation can be written as

$$\begin{aligned}\left(a_0\mathbf{M}+a_1\mathbf{C}+\left(1-\alpha_f\right)\mathbf{K}\right)d^{n+1} = \left(1-\alpha_f\right)\mathbf{F}_{ext}^{n+1}+\alpha_f\mathbf{F}_{ext}^{n}-\alpha_f\mathbf{F}_{int}^{n}\\ +\mathbf{M}\left(a_0d^n+a_2\dot{d}^n+a_3\ddot{d}^n\right)\\ +\mathbf{C}\left(a_1d^n+a_4\dot{d}^n+a_5\ddot{d}^n\right).\end{aligned} \tag{3.32}$$

The coefficients required in above equations are provided as follows.

$$\begin{aligned}a_0=\frac{1-\alpha_m}{\alpha\triangle t^2}\ ,\ a_1=\frac{\delta\left(1-\alpha_f\right)}{\alpha\triangle t}\ ,\ a_2=\frac{1-\alpha_m}{\alpha\triangle t}\ ,\ a_3=\frac{1-\alpha_m}{2\alpha}-1\ ,\\ a_4=\frac{\delta\left(1-\alpha_m\right)}{\alpha}-1\ ,\ a_5=\triangle t\left(1-\alpha_m\right)\left(\frac{\delta}{2\alpha}-1\right)\end{aligned} \tag{3.33}$$

In order to maintain unconditional stability and second order accuracy of time integration, the following criteria must be satisfied (*ANSYS Inc. 2009. ANSYS CFX-Solver Theory Guide*, n.d.).

$$\delta\geq\frac{1}{2}\ ,\ \alpha\geq\frac{1}{2}\delta\ ,\ \delta=\frac{1}{2}-\alpha_m+\alpha_f\ ,\ \alpha_m\geq\alpha_f\geq\frac{1}{2}. \tag{3.34}$$

The studies by (Wood et al., 1981) suggests that these parameters can be written in terms of amplitude decay factor γ as

$$\alpha=\frac{1}{4}(1+\gamma)^2\ ,\ \delta=\frac{1}{2}+\gamma\ ,\ \alpha_f=0\ ,\ \alpha_m=-\gamma. \tag{3.35}$$

When minimum numerical damping is applied, the value of α, δ, α_m and α_f are set to be $\frac{1}{4}$, $\frac{1}{2}$, 0, 0 respectively. These values represent time integration which has zero numerical damping. This can be achieved by setting $\gamma=0$. The equations for $\ddot{d}^{n+1}$ and $\dot{d}^{n+1}$ can be put as

$$\dot{d}^{n+1}=\dot{d}^n+\frac{1}{2}\triangle t\ddot{d}^n+\frac{1}{2}\triangle t\ddot{d}^{n+1}, \tag{3.36}$$

$$\ddot{d}^{n+1} = \frac{4}{\triangle t^2}\left[d^{n+1} + d^n - \triangle t\dot{d}^n - \frac{\triangle t^2}{4}\ddot{d}^n\right]. \tag{3.37}$$

After some mathematical manipulation, the structural acceleration can be written in terms of deformation at different time levels as

$$\ddot{d}^{n+1,\alpha} \approx \frac{1}{\triangle t^2}\left(4d^{n+1} - 16d^n + 32d^{n-1} - 20d^{n-2}\right) - \frac{12}{\triangle t}\dot{d}^{n-2} - \ddot{d}^{n-2}. \tag{3.38}$$

This time integration scheme cannot be put in terms of displacement only and it has the fully recursive characteristics which means that the calculation of time step $n+1$ utilizes information of all previous time steps down to the intial step.

When maximum numerical damping is applied, the values of α, δ, α_m and α_f are set to be 1, $\frac{3}{2}$, -1 and 0 respectively. This can be alternatively achieved by setting $\gamma = 1$. Therefore, equations for $\ddot{d}^{n+1}$ and $\dot{d}^{n+1}$ can be written as

$$\dot{d}^{n+1} = \dot{d}^n + \frac{1}{2}\triangle t\ddot{d}^n + \frac{3}{2}\triangle t\ddot{d}^{n+1}, \tag{3.39}$$

$$\ddot{d}^{n+1} = \frac{1}{\triangle t^2}\left[d^{n+1} + d^n - \triangle t\dot{d}^n - \frac{\triangle t^2}{2}\ddot{d}^n\right]. \tag{3.40}$$

Subsequently, this leads to

$$\ddot{d}^{n+1,\alpha} = \frac{1}{\triangle t^2}\left(2d^{n+1} - 5d^n + 4d^{n-1} - d^{n-2}\right). \tag{3.41}$$

3.3 Fundamental conditions for FSI coupling

The conditions required when solving FSI are kinematic and dynamic ones, which is suggested by the work by Wang and Yan (2010). The kinematic condition ensures the compatibility of displacement across FSI interface. It can be written as

$$d^f_\Gamma = d^s_\Gamma, \tag{3.42}$$

where d is displacement, d_Γ^s and d_Γ^f are the displacement of the solid and fluid interface, respectively. This condition leads to a relationship between fluid velocity $\mathbf{v}_\Gamma$ and rate of change of displacement, which can be written as

$$\widehat{n} \cdot \mathbf{v}_\Gamma = \widehat{n} \cdot \dot{d}_\Gamma^s, \tag{3.43}$$

where $\widehat{n}$ is normal vector on the interface.

If no-slip condition is used on the fluid side of the FSI interface. The dynamic condition ensures the compatibility of traction across FSI interface. It can be written as

$$\widehat{n} \cdot \sigma_\Gamma^s = \widehat{n} \cdot \sigma_\Gamma^f, \tag{3.44}$$

where σ_Γ represents stress on the interface.

These two conditions are normally utilized in FSI codes, which adopts the partitioned approach. By following the kinematic condition, fluid nodes on FSI interface are updated according to their corresponding solid nodes. By following the dynamic condtion, the equilibrium of stress on FSI interface is ensured and the fluid pressure is integrated into fluid force which is used when applying to solid nodes along interface. A simple diagram can illustrate that these two conditions force the transfer of interface loads across FSI interface as shown in Figure 3.4

3.4 Implementation of artificial compressibility

In this section, the implementation of artificial compressibility is discussed. In this thesis, artificial compressibility is applied to solution system of fluid-structure interaction of working fluid. The density of fluid is generally written as follows:

If working fluid is modelled as incompressible flow, then

$$\rho = \rho_0 + \text{Artificial compressibility}. \tag{3.45}$$

If working fluid is modelled as compressible flow, then

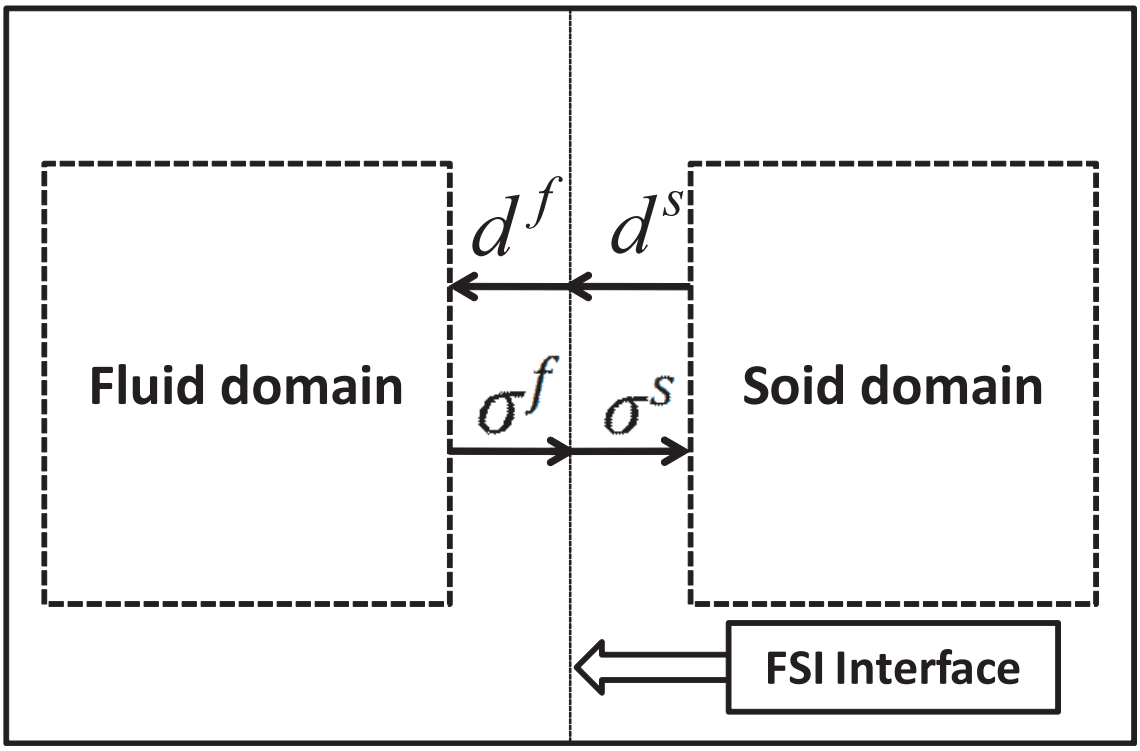

Figure 3.4: Diagram of FSI coupling

$$\rho = \rho_0 + \text{Artificial compressibility} + \text{Real compressibility}. \tag{3.46}$$

Note that

$$\text{Artificial compressibility} = \frac{P_{m+1,i}^{n+1} - P_{m,i}^{n+1}}{K_{ac}}, \tag{3.47}$$

$$\text{Real compressibility} = \rho_0 \frac{P_{m+1,i}^{n+1,f}}{K_B}, \tag{3.48}$$

where K_{ac} and K_B are related to the artificial and real bulk modulus respectively. K_B depends on the working fluid. It is directly related to bulk modulus of the fluid being solved. On the other hand, K_{ac} is a variable which represents a relationship between deformation and fluid pressure. It can be determined by computing equation (3.49) which is written as

$$K_{ac} = \frac{1}{V}\frac{d\mathbf{V}}{d\mathbf{P}} = \frac{\mathbf{V} - \mathbf{V}_0}{\mathbf{V}_0}\frac{1}{d\mathbf{P}}. \tag{3.49}$$

Recall that the continuity equation is provided earlier as

$$\frac{\partial \rho}{\partial t} + (\mathbf{v} - \mathbf{v}_c) \cdot \nabla \rho + \rho \nabla \cdot \mathbf{v} = 0. \tag{3.50}$$

By rewritting it in the integral form, we get

$$\int_{V_P} \frac{\partial \rho}{\partial t} d\mathbf{V_P} + \int_{\mathbf{V_P}} (\mathbf{v} - \mathbf{v}_c) \cdot \nabla \rho \; d\mathbf{V_P} + \int_{\mathbf{V_P}} \rho \nabla \cdot \mathbf{v} \; d\mathbf{V_P} = 0, \tag{3.51}$$

$$\rho \frac{\partial \mathbf{V_P}}{\partial t} + \rho \oint_{\mathbf{V_P}} (\mathbf{v} - \mathbf{v}_c) \; d\mathbf{A_P} + \rho \oint_{\mathbf{V_P}} \nabla \cdot \mathbf{v} \; d\mathbf{A_P} = 0, \tag{3.52}$$

$$\rho \left(\frac{\partial \mathbf{V_P}}{\partial t} + \oint_{\mathbf{V_P}} (\mathbf{v} - \mathbf{v}_c) \; d\mathbf{A_P} + \oint_{\mathbf{V_P}} \nabla \cdot \mathbf{v} \; d\mathbf{A_P} \right) = 0. \tag{3.53}$$

By applying artificial compressibility, the governing equation of fluid analysis becomes

$$\underbrace{\frac{\left(P_{m+1,i}^{n+1} - P_{m,i}^{n+1}\right)}{K_{ac}} \left(\frac{\partial \mathbf{V_P}}{\partial t} + \oint_{\mathbf{V_P}} (\mathbf{v} - \mathbf{v}_c)\ d\mathbf{A_P} + \oint_{\mathbf{V_P}} \nabla \cdot \mathbf{v}\ d\mathbf{A_P} \right)}_{\textbf{Contribution from artificial compressibility}}$$
$$+ \underbrace{\rho_0 \left(\frac{\partial \mathbf{V_P}}{\partial t} + \oint_{\mathbf{V_P}} (\mathbf{v} - \mathbf{v}_c)\ d\mathbf{A_P} + \oint_{\mathbf{V_P}} \nabla \cdot \mathbf{v}\ d\mathbf{A_P} \right)}_{\textbf{Contribution from rigid fluid solution}} = 0. \tag{3.54}$$

The contribution from artificial compressibility provides the estimation of how a flexible solid part will react to fluid pressure exerted on interface. This estimation then used to calculate added-mass force which is likely to occur due to the original fluid pressure calculated from the assumption that fluid domain is fixed. This is similar to the decomposition of fluid pressure mentioned in the work by Causin et al. (2005). The estimation is done by using the relationship between fluid pressure and the change in an infinitsimal volume due to the pressure through K_{ac}. The result of this manipulation of a fluid governing equation leads to an increase in implicitness of solution algorithm of fluid-structure interaction using the partitioned approach.

3.5 Procedure of calculation

In this section, the following methods are discussed. The iterative method, which is used for FSI coupling in ANSYS-CFX, is Dirichlet/Neumann approach. This simply means that fluid equation is imposed with the Dirichlet boundary condition at the interface such as displacement and velocity. On the other hand, solid equation is subjected to the Neumann boundary condition such as force. This section can be divided into two subsection as follows:

- Procedure of calculation with under-relaxation;
- Procedure of calculation with aritificial compressibility.

3.5.1 Under-relaxation

Standard procedure of calculation in FSI with under-relaxation technique can be summarized here. Similar procedures of FSI solution can be found in the works by (Kamakoti and Shyy, 2004) and (Wall, Forster, Neumann and Ramm, 2006). If fluid problem is solved before solid probem in the sequence of partitioned approach, the procedure is as follows. Note that m and m+1 represent two adjacent coupling steps, which are used to describe the procedure of calcuation that will continue in the same manner for the entire simulation as shown in Figure 3.5.

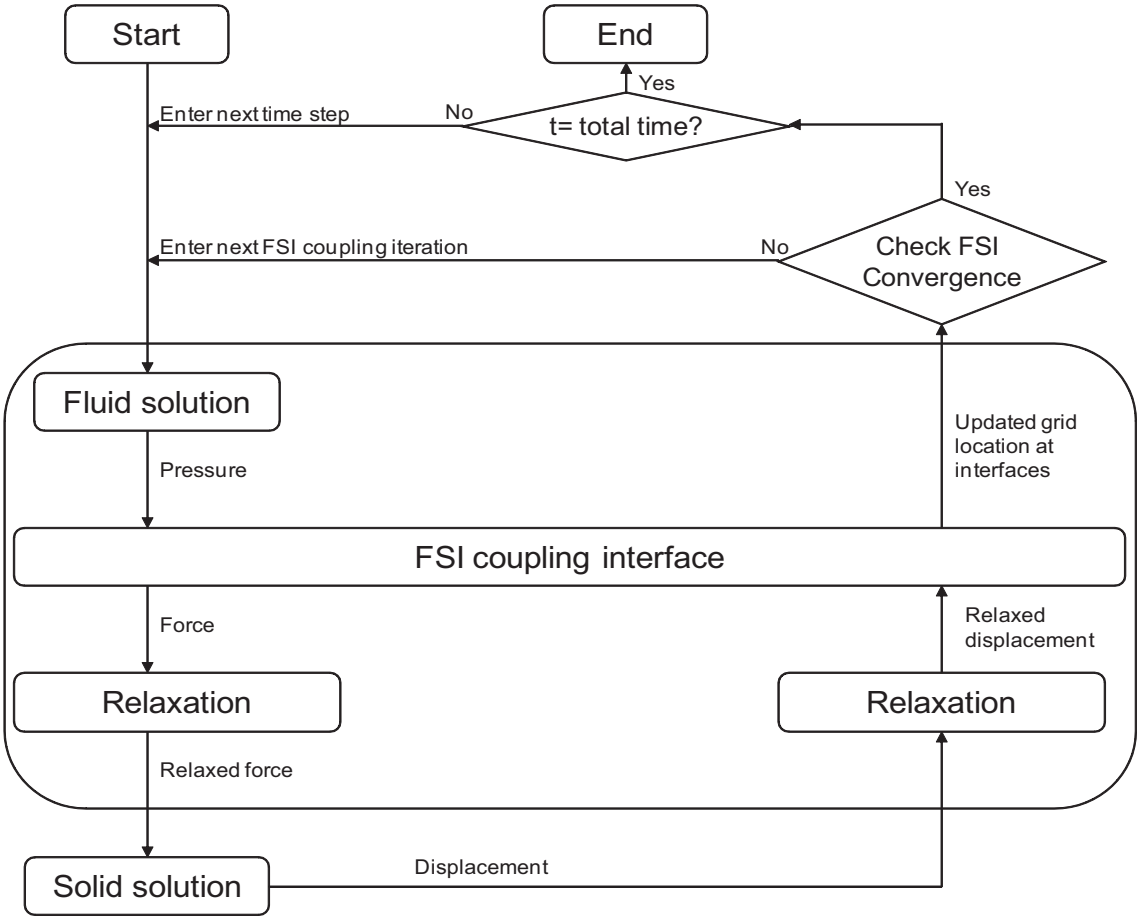

Figure 3.5: Flowchart of standard procedure of partitioned approach when using under-relaxation technique

1. Compute initial configuration of fluid domain by using information passed from previous time step, d^n in case of the first coupling step of time step level $n+1$, otherwise information passed from previous coupling iteration, d_m^{n+1} will be used instead. That is

$$\widetilde{d}_{m+1}^{n+1} = \begin{cases} d^n \text{ if } m = 0 \\ d_m^{n+1} \text{ if } m \neq 0, \end{cases} \tag{3.55}$$

where $denotesthatthedisplacementisonlyanestimation.$

2. Solve fluid field using a fluid solver to get

$$\widetilde{P}_{m+1}^{n+1} = F\left(\widetilde{d}_{m+1}^{n+1}\right), \tag{3.56}$$

where P represents fluid pressure, F represents fluid calculation.

3. Transfer fluid load obtained to solid solver and estimate corresponding load to be applied in solid solver. That is

$$\widetilde{P}_{m+1}^{n+1} = \omega\left(\widetilde{P}_{m+1}^{n+1}\right), \tag{3.57}$$

where ω is an applied under-relaxation factor.

4. Solve solid governing equation to get

$$\widetilde{d}_{m+1}^{n+1} = S\left(\widetilde{P}_{m+1}^{n+1}\right), \tag{3.58}$$

where S represents solid calculation.

5. Estimate deformation of fluid domain, which is corresponding to solid solution obtained from previous step. That is

$$d_{m+1}^{n+1} = (1-\omega)\,\widetilde{d}_{m+1}^{n+1} + \omega d_m^{n+1}. \tag{3.59}$$

Note that $\widetilde{d}_{m+1}^{n+1}$ is not the final solid solution but only an estimation for fluid calculation at coupling level $m+1$.

6. Check for convergence. The solution is converged if the following conditions is applied. Here,

$$r^{n+1,s} < \varepsilon_0,\ r^{n+1,s} = d_{m+1}^{n+1} - d_m^{n+1}, \tag{3.60}$$

$$r^{n+1,f} < \varepsilon_0,\ r^{n+1,f} = P_{m+1}^{n+1} - P_m^{n+1}, \tag{3.61}$$

where r is calculated residual, ε_0 is a tolerance used for determining convergence of solution. Note that superscripts s and f denotes solid and fluid respectively.

7. Proceed to next time step or finish simulation if convergence is reached. If convergence is not reached, then continue the iteration process in a similar manner as mentioned above.

If the under-relaxation factor and number of coupling iteration used for secondth and sixth step are chosen to be 1, the FSI algorithm becomes explicit. Calculation can be done in a similar manner if the solid problem is solved before fluid problem in the sequence of partitioned approach.

3.5.2 Aritificial compressibility

Standard procedure of calculation in FSI with artificial compressibility can be presented here. For this technique, the artificial compressibility is applied to fluid density as mentioned in the previous section. If the fluid problem is solved before solid probem in the sequence of partitioned approach, the procedure is as follows. Note that m and $m+1$ represent two adjacent coupling steps which are used to describe the procedure of calcuation that will continue in the same manner for the entire simulation. The procedure of calculation above can be illustrated with a simple diagram in Figure 3.6.

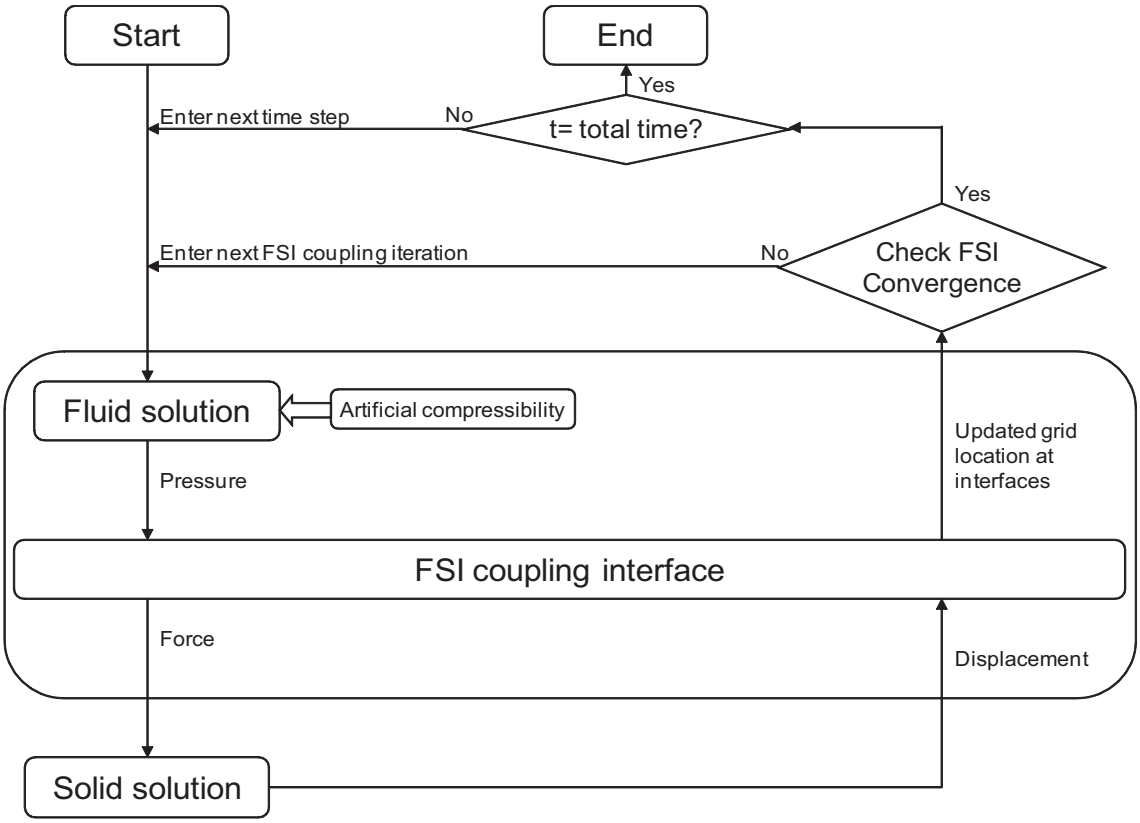

Figure 3.6: Flowchart of standard procedure of partitioned approach when using artificial compressibility

1. Compute initial configuration of fluid domain by using information passed from previous time step, d^n in case of the first coupling step of time step level $n+1$, otherwise information passed from previous coupling iteration, d_m^{n+1} will be used instead. That is

$$\widetilde{d}_{m+1}^{n+1} = \begin{cases} d^n \text{ if } m = 0 \\ d_m^{n+1} \text{ if } m \neq 0. \end{cases} \tag{3.62}$$

2. Solve fluid field using a fluid solver to get

$$\widetilde{P}_{ac,m+1}^{n+1} = F_{ac}\left(\widetilde{d}_{m+1}^{n+1}\right), \tag{3.63}$$

where P_{ac} and F_{ac} represent respectively the fluid pressure and fluid calculation which accounts for artificial compressibility.

3. Transfer fluid load obtained to solid solver and estimate corresponding load to be applied in solid solver. That is

$$\widetilde{P}_{ac,m+1}^{n+1} = \left(\widetilde{P}_{ac,m+1}^{n+1}\right). \tag{3.64}$$

4. Solve solid governing equation to get

$$\widetilde{d}_{ac,m+1}^{n+1} = S\left(\widetilde{P}_{ac,m+1}^{n+1}\right). \tag{3.65}$$

5. Estimate deformation of fluid domain, which is corresponding to solid solution obtained from previous step. That is

$$d_{ac,m+1}^{n+1} = \widetilde{d}_{ac,m+1}^{n+1}. \tag{3.66}$$

Note that $d_{ac,m+1}^{n+1}$ is not final solid solution but only an estimation for fluid calculation using artificial compressibility at time step level $n+1$.

6. Check for convergence. The solution is converged if the following conditions are applied. Here,

$$r^{n+1,s} < \varepsilon_0,\ r^{n+1,s} = d_{ac,m+1}^{n+1} - d_m^{n+1}, \tag{3.67}$$

$$r^{n+1,f} < \varepsilon_0,\ r^{n+1,f} = P_{ac,m+1}^{n+1} - P_m^{n+1}. \tag{3.68}$$

7. Proceed to next time step or finish simulation if convergence is reached. If convergence is not reached, then continue the iteration process in a similar manner mentioned above. It is necessary to emphasize that $d_{ac,m+1}$ will eventually approach to d_{m+1} as the effect of artificial compressibility disappears at convergence of FSI interface loads.

3.6 Convergence of interface loads

According to *ANSYS Inc. 2009. ANSYS CFX-Solver Theory Guide* (n.d.), criteria which is used for determining if the FSI solution is converged is explained. Here,

$$\text{Conv} = \frac{log\left(\frac{\epsilon_x}{\epsilon_{min}}\right)}{log\left(\frac{\epsilon_{max}}{\epsilon_{min}}\right)}, \tag{3.69}$$

where ϵ_x = norm of each of the interface quantities
which is transferred between two physical disciplines
$= \left(\sum R_i^2\right)^{\frac{1}{2}}$,
ϵ_{min} = Convergence criteria specified by in coupling set up,
ϵ_{max} = Divergence threshold. This value is set to be 100 by default.

To determine convergence of FSI solution, calculation of of each interface load quantities and consider the following conditions:

- If $\epsilon_x < \epsilon_{min}$, then solution has converged;
- If $\epsilon_x > \epsilon_{min}$, then solution has not converged.

Let's us consider a simple example to illustrate the information provided above. By assumming that ϵ_x, ϵ_{min} and ϵ_{max} are set as 0.01, 0.001 and 100 respectively. Before calculation, we could expect the solution to not converged because $\epsilon_x > \epsilon_{min}$.

$$\text{Conv} = \frac{log\left(\frac{0.01}{0.001}\right)}{log\left(\frac{100}{0.001}\right)} = \frac{log(10)}{log(5)} = 1.4285.$$

As expected, $Conv$ is still greater than 0. This means that the solution has not converged and more coupling iteration is required.

3.7 General procedure of FSI simulation setup

In this section, steps of conducting fluid structure interaction simulation in ANSYS are discussed as follows. This can be used as a general guideline for conducting fluid-structure interaction with under-relaxation technique.

1. Create geometry in fluid and solid.
2. Create mesh for fluid domain and solid domain. Quality control of computational elements used in each domain is checked strictly.
3. Set up proper analysis types (transient or steady) for both fluid and solid domain. It is important to ensure that the time step size used for fluid calculation is correspondent to that used in solid calculation.
4. Set up proper boundary conditions of both fluid and solid domain. Besides the normal boundary conditions required in FEA and CFD, fluid structure interaction boundary condition is required for transferring interface load. Fluid and solid mesh do not have to be conformal but the area of the interface has to be the same to avoid any loss during load transfer across FSI interface. This can be checked at the beginning of output file for every FSI simulation. It is

necessary to ensure that the percentage of the non-matching area is less than 2 percent.

5. Coupling setting should be properly set considering time consumption, accuracy and stability of solution. Maximum number of coupling step: use bigger number if more coupling step is needed. However, it has to be selected with care because it can increase simulation time significantly. Relaxation for interface loads (such as displacements and forces): use smaller number, which is ranged between zero to one. Although small value of relaxation factors can sometimes help improving stability of FSI solution, it also increases computational time significantly. Convergence criteria for each interface load: if accuracy of FSI is needed to be improved, convergence criteria should be reduced. Also, it has to be small enough for maintaining stability of solution because it sometime is necessary to keep the error as small as possible to avoid artificial added mass effect in the next coupling iteration.

6. After solution is converged, post-processing is performed.

3.8 Construction and setup for mesh in FSI

In this section, the Spring analogy for moving mesh (*ANSYS Inc. 2009. ANSYS CFX-Solver Theory Guide*, n.d.), (Wuchner et al., 2007), which is the method for mesh movement used in this project, is discussed. In this method, each individual mesh element is assigned with a stiffness value. The stiffness value is varied from low near the interface to high in the far field region. The variation is made in this way to avoid mesh folding, which could occur when experiencing large deformation in the system. In CFX, mesh motion is governed by a following Laplace equation:

$$\bigtriangledown \cdot (K_{mesh} \bigtriangledown \delta) = 0, \tag{3.70}$$

where δ is the displacement relative to the previous mesh location. K_{mesh} is mesh stiffness which determines relationship of how regions of nodes move together.

There are two options in CFX for mesh movement as follows:

- Increase near small volumes

$$K_{mesh} = \left(\frac{1}{\overline{\overline{\mathbf{V}}}} \right)^{C_{stiff}} . \tag{3.71}$$

- Increase near boundary

$$K_{mesh} = \left(\frac{1}{d_{mesh}} \right)^{C_{stiff}} , \tag{3.72}$$

where $\overline{\mathbf{V}}$ and d_{mesh} stand for control volume size and distance from the nearest boundary respectively. C_{stiff} is stiffness exponential constant.

It is important to note that in each individual analysis, stiffness exponential has to be properly selected to suit the nature of the analysis. This is mainly to avoid the failure of mesh movement which can lead to the failure of fluid solution due to highly skewed elements or negative volumes. This can be demonstrated by the following simple analysis which give us a general idea about the importance of the proper variation of elemental stiffness. This investigation about mesh movement is done in a simple benchmarking problem which is flow pass an orifice. Table 3.1 shows the details of cases in this investigation about mesh motion.

	Solid properties			**Fluid properties**		**Stiffness parameter**
	Density (kg/m^3)	Young modulus (Pa)	Poisson ratio	Density (kg/m^3)	Dynamic viscosity (Pa s)	Stiffness exponential constant used for successful simulation
Case 1	1000	2×10^{11}	0.3	1000	0.01	10
Case 2	1000	9×10^{6}	0.3	1000	0.01	10
Case 3	1000	9×10^{6}	0.3	1000	0.01	5

Table 3.1: Table of mesh motion analysis.

In case 1, the solid structure is modelled to be very stiff and can withstand the flow which is pushing from the front of the structure as shown in Figure 3.7. The

stiffness exponential constant used in this case is 10, which is a default value in CFX.

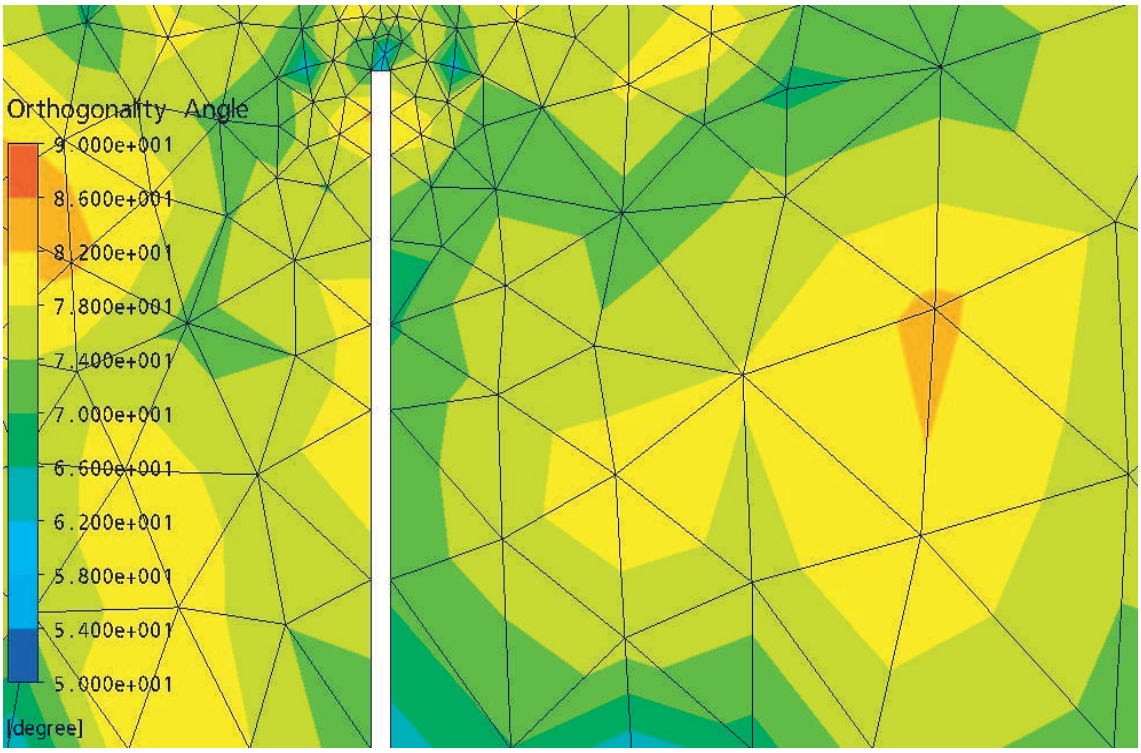

Figure 3.7: Mesh motion of case 1.

After that, we reduce Young modulus value of the solid structure to 9E6 Pa in case 2. In this case, the solution can only proceed for a few time steps and then failed due to mesh distortion. This is mainly because solid structure becomes more flexible and therefore more deformation is expected. At the time step before the solution fails, we can observe high deformation which might cause the computational elements to become distorted and then lead to failure of the solution. Figure 3.8 illustrates highly distorted elements in the computational domain.

In case 3, we reduce the stiffness exponential constant from 10(default) to 5. This proved to be a successful treatment to the problem, which we observed in case 2. The mesh quality is considerably improved as shown in Figure 3.9 and final solution of simulation can be reached.

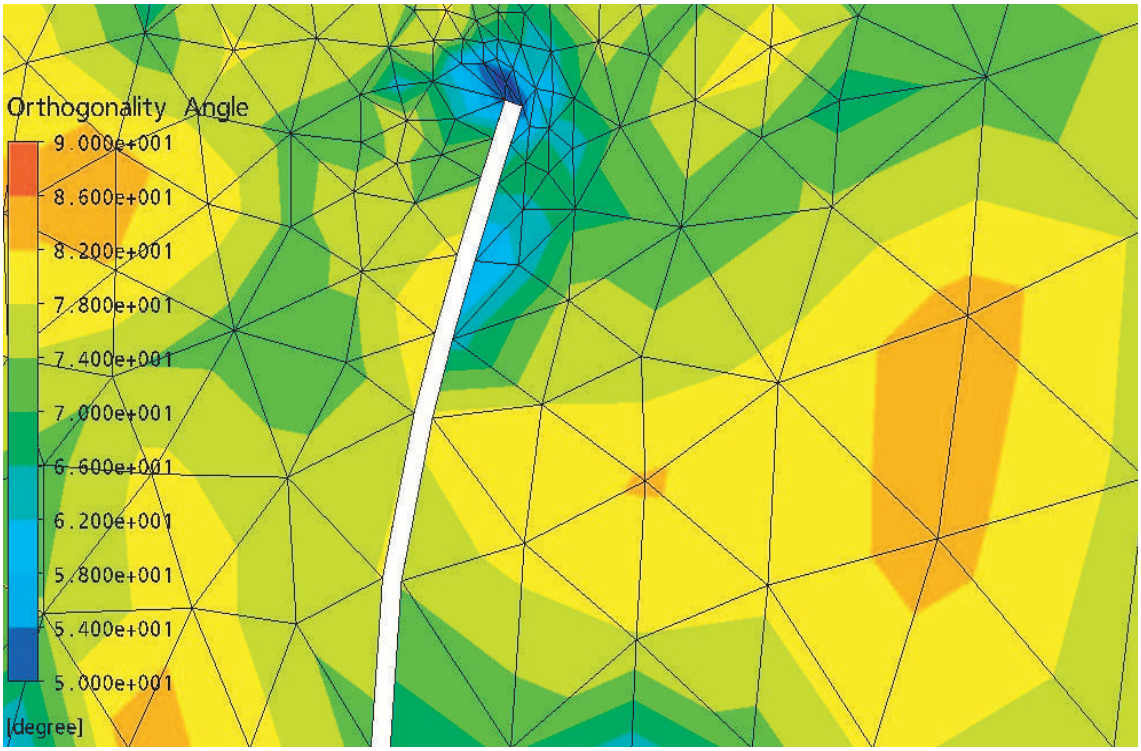

Figure 3.8: Mesh motion of case 2.

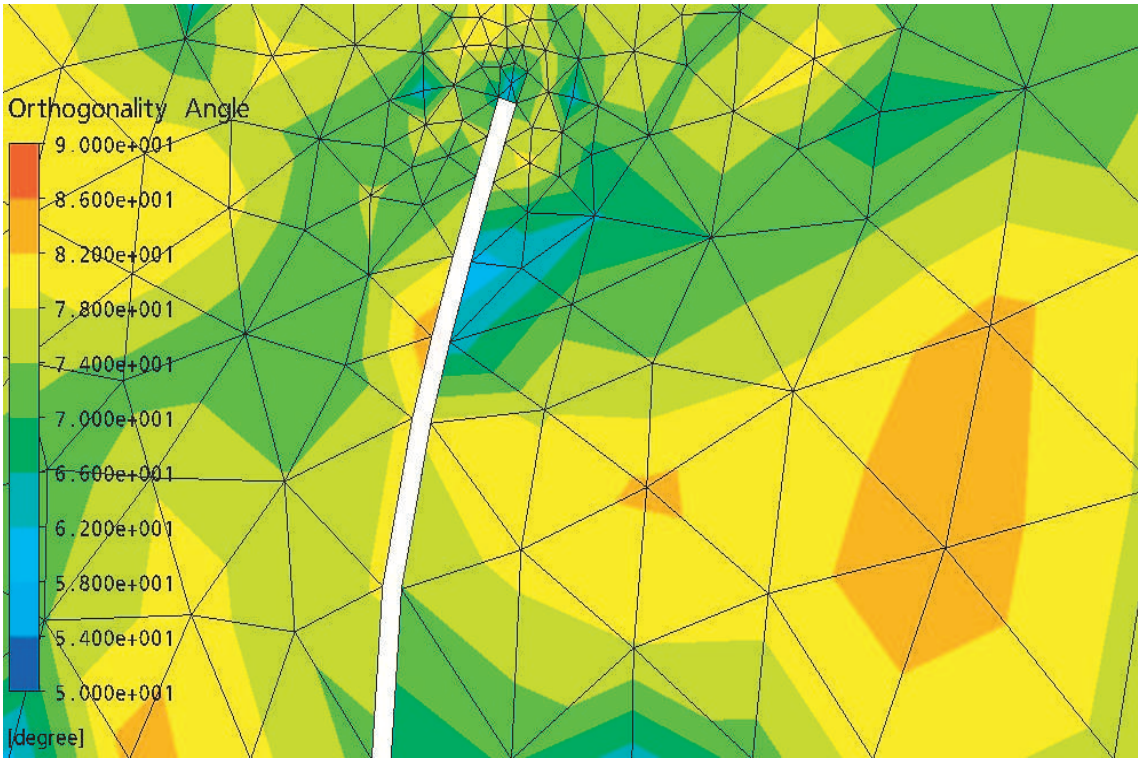

Figure 3.9: Mesh motion of case 3.

From the above investigation, it can be pointed out that elemental stiffness of computational domain should be properly set up by considering the deformation, is expected to occur during simulation. From both equations above, the larger C_{stiff} will lead to a larger stiffness gradient. And we can also expect that large stiffness gradient will cause negative volume and folded mesh. This can be explained by considering two adjacent elements, one moves significantly but the other element does not move (or slightly move), then the element that moves significantly will fold onto the other one. It may be a straight forward idea to reduce the C_{stiff} to smooth out the mesh whenever we get the mesh folding or negative volume due to large deformation. However, the lack of accuracy due to this small value of C_{stiff} may affect our result. This is due to the structure not experiencing significantly large deformation but the mesh stiffness gradient is chosen to be small; the quality of mesh surrounding the solid structure at interface becomes slightly lower compared to that when we have higher C_{stiff}. To optimize this, an expression was suggested in (*Solving FSI Applications using Workbench, ANSYS Mechanical and CFX*, n.d.) as follows.

$$C_{stiff} = 1 - \left(\frac{\text{wall distance} - \text{minimum value of wall distance}}{\text{maximum value of wall distance} - \text{minimum value of wall distance}} \right)^2 . \tag{3.73}$$

3.9 Summary and concluding remarks

This chapter provides detailed information about governing equations and methodology incluing discretization schemes used for both fluid and solid solver. Also, calculation procedures corresponding to techniques are discussed. Moreover, best practice in FSI based on the author's knowledge and experience is suggested.

Chapter 4

Theoretical analysis of stability in FSI

4.1 Introduction

Fluid-structure interaction is used widely in many engineering fields such as Automotive, Biomechanical and Aerospace engineering. It can be done in mainly two approaches: Monolithic and Partitioned approach. FSI solvers, when using the first approach, solves a system of governing equations of both fluid and solid fields (Hron and Turek, 2006). Although it gives strong coupling between the fields, the shortcomings are the following.

- Demanding computational power for solving a large system of equations
- The need for further development preconditioning
- Lack of specialized capabilities of the sophisticated software such as ABAQUS and ANSYS.

On the other hand, the partitioned approach is attractive due to its advantage of software modularity allowing selection of an appropriate solver among well-established solvers for each field. However, the efficiency of partitioned approach

is inferior to the other approach due to the existence of the so-called "Added-mass instability" which commonly occurs in problems with large deformation and light weight structure. This can cause FSI solution to diverge and fail before the final solution is reached. In order to handle this instability, small values of coupling relaxation factors of interface loads must be used in order to maintain stability of calculation. This leads to a significant increase in computational time. It is understood that FSI solution experiences this numerical instability when the following conditions is observed (Forster et al., 2007).

- Stability of FSI solution tends to be highly severe when density ratio between fluid and solid $\frac{\rho_f}{\rho_s}$ is high.
- The increase in fluid viscosity leads to increased instability. In contrast, the increase in structural stiffness results in less instability.
- Temporal discretisation schemes used for FSI calculation could influence the condition of instability.
- The decrease in time step size used for FSI calculation make instability occur earlier.

The observed behaviours of the instability is explained mathematically by Causin et al. (2005) where conditions for stability of both explicit and implicit FSI solution of a flexible cylindrical vessel are demonstrated. However, impact of structural time integration scheme, which is used for FSI calculation, is still not fully understood. The main aim of this chapter is to analyze performance of FSI using partitioned approach based on different structural time integration schemes. We conduct the analysis on a simplified problem of pressure wave propagation along a flexible cylindrical vessel. Our findings can be summarized as follows.

- Influence of structural time integration schemes on performance of FSI
- Influence of time step size
- Influence of density ratio

- Influence of geometric properties

Moreover, a theoretical analysis of FSI coupling using artificial compressibility is also discussed and compared with those using under-relaxation technique. This chapter is organized as follows. In Section 2, a mathematical description of a simplified pressure wave propagation along a flexible cylindrical vessel and fundamental FSI conditions are presented. In Section 3, theoretical analysis of stability based on under-relaxation technique are discussed.

4.2 Simplified problem for stability analysis

A simple flexible cylindrical tube is chosen for our mathematical analysis. It allows mathematical and numerical studies to be performed, and provides enough information for conducting a more realistic situation. A schematic representation of our problem domain is shown in Figure 4.1.

Deformation of the cylindrical tube is allowed only in the radial and longitudinal directions. Inlet and outlet of the fluid domain are subjected to pressure boundary conditions. We refer to governing equation of deformation of a flexible cylindrical tube in the work by Causin et al. (2005), which can be written as

$$\rho_s h_s \frac{\partial^2 d_\Gamma}{\partial t^2} + a_0 d_\Gamma - b\frac{\partial^2 d_\Gamma}{\partial x^2} = P_{\Sigma,\Gamma}, \tag{4.1}$$

$$\rho_s h_s \frac{\partial^2 d_\Gamma}{\partial t^2} + a_0 d_\Gamma - b\frac{\partial^2 d_\Gamma}{\partial x^2} = P_{ext,\Gamma} - \rho_f M_a \frac{\partial^2 d_\Gamma}{\partial t^2}, \tag{4.2}$$

$$\rho_s h_s \frac{\partial^2 d_\Gamma}{\partial t^2} + \rho_f M_a \frac{\partial^2 d_\Gamma}{\partial t^2} + a_0 d_\Gamma - b\frac{\partial^2 d_\Gamma}{\partial x^2} = P_{ext,\Gamma}, \tag{4.3}$$

where $a_0 = \frac{Eh_s}{r^2(1-\nu^2)}$, $b = K_T B h_s$, x is position in space and t is position in time.

Since we are interested in added-mass instability, where the mass term is dominated the stiffness term, we will neglect some non-linearity. Therefore, (4.3) is reduced to equation (4.4) such that

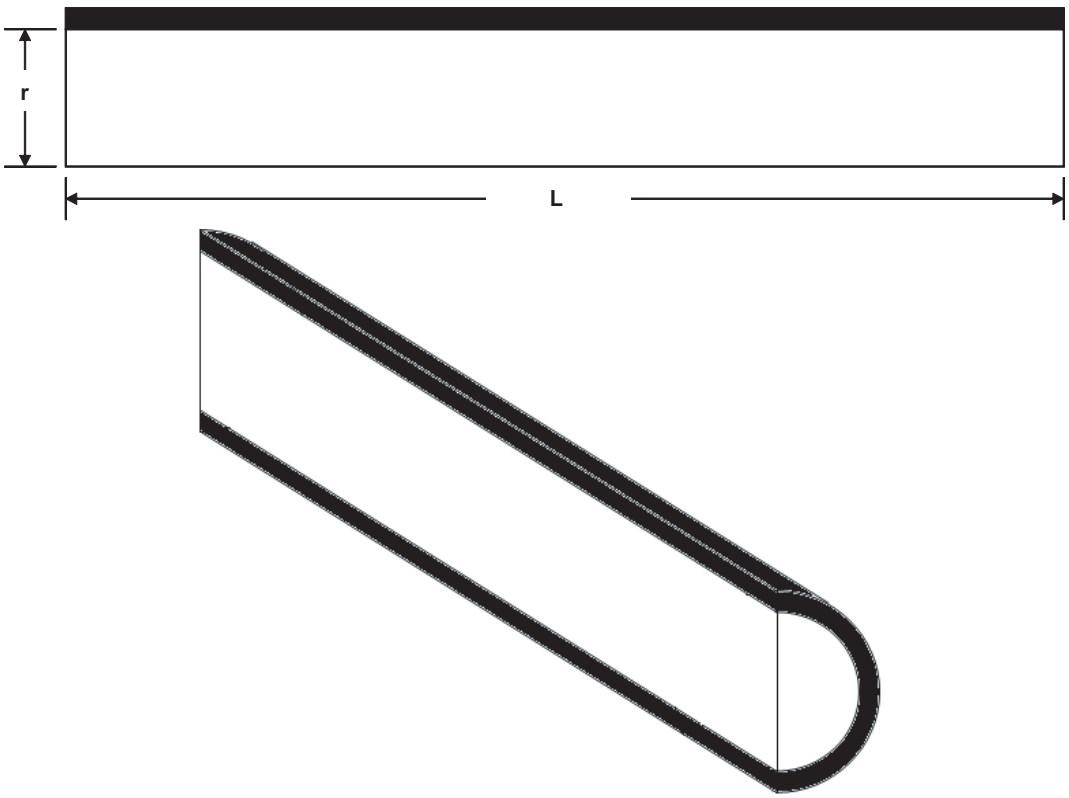

Figure 4.1: Graphical representation of flexible vessel.

$$\rho_s h_s \frac{\partial^2 d_\Gamma^s}{\partial t^2} + \rho_f M_a \frac{\partial^2 d_\Gamma^f}{\partial t^2} + a_0 d_\Gamma^s = P_{ext,\Gamma}. \tag{4.4}$$

4.3 Theoretical analysis: under-relaxation

A stability analysis of FSI calculation using implicit coupling is presented. By adopting implicit coupling, several coupling iterations are needed for each time step and relaxation is applied to maintain the stability of calculation.

4.3.1 Stability condition: minimum numerical damping is applied

In this section, the analysis of explicit FSI coupling, when minimum numerical damping is used, is discussed.

The discretized form of structural acceleration is written as

$$\ddot{d}_\Gamma^{n+1,s} \approx \frac{1}{\triangle t^2}\left(4d_\Gamma^{n+1} - 16d_\Gamma^n + 32d_\Gamma^{n-1} - 20d_\Gamma^{n-2}\right) - \frac{12}{\triangle t}\dot{d}_\Gamma^{n-2} - \ddot{d}_\Gamma^{n-2}. \tag{4.5}$$

The discretized form of fluid acceleration is written as

$$\ddot{d}_\Gamma^{n+1,f} = \tfrac{1}{\Delta t^2}(\widetilde{d}_\Gamma^{n+1} - 2d_\Gamma^n + d_\Gamma^{n-1}). \tag{4.6}$$

Unlike explicit coupling, the latest information used for calculation of FSI interface acceleration of fluid domain comes from the same time level with that used for structural acceleration. This is due to the application of relaxation factors.

Discretization of equation (4.4) is achieved by substituting equations (4.5) and (4.6) to give

$$\frac{\rho_s h_s}{\triangle t^2}(4\widetilde{d}_\Gamma^{n+1} - 16d_\Gamma^n + 32d_\Gamma^{n-1} - 20d_\Gamma^{n-2} - \frac{12}{\triangle t^3}\dot{d}_\Gamma^{n-2} - \frac{1}{\triangle t^2}\ddot{d}_\Gamma^{n-2})$$
$$+\frac{\rho_f M_a}{\triangle t^2}(\widetilde{d}_\Gamma^{n+1} - 2d_\Gamma^n + d_\Gamma^{n-1}) + a_0 d_\Gamma^{n+1} = P_{ext,\Gamma}^{n+1}. \tag{4.7}$$

To simplify it, the analysis can be done by considering only one eigenvector, $\mathbf{v_i}$ of solution on the interface. This is because the added mass opertor, M_A is a real positive matrix. Therefore, $d_\Gamma = \Sigma d_i \mathbf{v_i}$. Notice that the added-mass operator M_A can be represented by the ith eigenvalues of M_A, μ_i. This reduced equation (4.7) to (4.8) as given by

$$\frac{\rho_s h_s}{\triangle t^2}(4\widetilde{d}_i^{n+1} - 16d_i^n + 32d_i^{n-1} - 20d_i^{n-2} - \frac{12}{\triangle t^3}\dot{d}_i^{n-2} - \frac{1}{\triangle t^2}\ddot{d}_i^{n-2})$$
$$+\frac{\rho_f \mu_i}{\triangle t^2}(\widetilde{d}_i^{n+1} - 2d_i^n + d_i^{n-1}) + a_0 d_i^{n+1} = \frac{\triangle t^2}{\rho_s h_s} P_{ext,i}^{n+1}. \tag{4.8}$$

By substituting equation (3.59), equation (4.8) can be rewritten as

$$\frac{\rho_s h_s}{\triangle t^2}(\frac{4d_i^{n+1}}{\omega} - 16d_i^n + 32d_i^{n-1} - 20d_i^{n-2} - \frac{12}{\triangle t^3}\dot{d}_i^{n-2} - \frac{1}{\triangle t^2}\ddot{d}_i^{n-2}) + a_0\frac{d_{m+1,i}^{n+1}}{\omega}$$
$$= \left(\frac{1-\omega}{\omega}\right)\left(\frac{2\rho_s h_s}{\triangle t^2} + a_0\right) d_{m,i}^{n+1} - \frac{\rho_f \mu_i}{\triangle t^2}(d_{m,i}^{n+1} - 2d_i^n + d_i^{n-1}) + \frac{\triangle t^2}{\rho_s h_s} P_{ext,i}^{n+1}, \tag{4.9}$$

$$\frac{1}{\omega}\left(\frac{4\rho_s h_s}{\triangle t^2} + a_0\right) d_{m+1,i}^{n+1} = \left[\left(\frac{1-\omega}{\omega}\right)\left(\frac{4\rho_s h_s}{\triangle t^2} + a_0\right) - \frac{\rho_f \mu_i}{\triangle t^2}\right] d_{m,i}^{n+1}$$
$$+g\left(d_i^n, d_i^{n-1}, d_i^{n-2}, \dot{d}_i^{n-2}, \ddot{d}_i^{n-2}, P_{ext,i}^{n+1}\right), \tag{4.10}$$

$$\frac{d_{m+1,i}^{n+1}}{d_{m,i}^{n+1}} \approx \frac{\left[\left(\frac{1-\omega}{\omega}\right)\left(\frac{4\rho_s h_s}{\triangle t^2}+a_0\right)-\frac{\rho_f \mu_i}{\triangle t^2}\right]}{\frac{1}{\omega}\left(\frac{4\rho_s h_s}{\triangle t^2}+a_0\right)} = \underbrace{1-\frac{\omega\left(4\rho_s h_s + a_0\triangle t^2 + \rho_f \mu_i\right)}{4\rho_s h_s + a_0 \triangle t^2}}_{Growth factor, G}. \quad (4.11)$$

Absolute value of the growth factor has to be less than unity if the solution is to be stable. That is

$$|G| = \left|1-\frac{\omega\left(4\rho_s h_s + a_0\triangle t^2 + \rho_f \mu_{max}\right)}{4\rho_s h_s + a_0 \triangle t^2}\right| < 1, \quad (4.12)$$

$$0 < \omega < \frac{8\rho_s h_s + 2a_0\triangle t^2}{4\rho_s h_s + a_0\triangle t^2 + \rho_f \mu_{max}}. \quad (4.13)$$

From equation (4.13), it is obvious that not only the material and geometrical properites such as density of both fluid and solid, Young modulus and the maximum eigenvalue of added mass matrix influences the allowable relaxation factor but also the time step size of the calculation. It can be further deduced that if the time step size is very small (approaching zero), then equation (4.13) becomes

$$0 < \omega < \frac{8}{4+\frac{\rho_f \mu_{max}}{\rho_s h_s}}. \quad (4.14)$$

This means that if time step size is very small, the Young modulus is no longer a factor that determines the criteria for stability of an implicit algorithm. Therefore, the critical value of relaxation factor converges and does not vary with a further decrease in time step size. Moreover, it can also be concluded that if $\rho_f \mu_{max} = \rho_s h_s$, then the relaxation factor has to be strictly less than $\frac{8}{5}$ to allow convergence of solution.

4.3.2 Stability condition: maximum numerical damping is applied

The discretized form of structural acceleration is written as

$$\ddot{d}_{\Gamma}^{n+1,s} = \frac{1}{\Delta t^2}(2\widetilde{d}_{\Gamma}^{n+1} - 5d_{\Gamma}^{n} + 4d_{\Gamma}^{n-1} - d_{\Gamma}^{n-2}). \tag{4.15}$$

The discretized form of fluid acceleration is written as

$$\ddot{d}_{\Gamma}^{n+1,f} = \tfrac{1}{\Delta t^2}(\widetilde{d}_{\Gamma}^{n+1} - 2d_{\Gamma}^{n} + d_{\Gamma}^{n-1}). \tag{4.16}$$

Unlike explicit coupling, the latest information used for calculation of FSI interface acceleration of fluid domain comes from the same time level as that used for structural acceleration. This is due to the application of relaxation factors.

The discretized form of equation (4.4) is achieved by substituting equations (4.15) and (4.16) to give

$$\begin{aligned}&\frac{\rho_s h_s}{\triangle t^2}(2\widetilde{d}_{\Gamma}^{n+1} - 5d_{\Gamma}^{n} + 4d_{\Gamma}^{n-1} - d_{\Gamma}^{n-2}) + \frac{\rho_f M_a}{\triangle t^2}(\widetilde{d}_{\Gamma}^{n+1} - 2d_{\Gamma}^{n} + d_{\Gamma}^{n-1}) + a_0 d_{\Gamma}^{n+1} \\ &= P_{ext,\Gamma}^{n+1},\end{aligned} \tag{4.17}$$

$$\begin{aligned}&\frac{\rho_s h_s}{\triangle t^2}(2\widetilde{d}_{i}^{n+1} - 5d_{i}^{n} + 4d_{i}^{n-1} - d_{i}^{n-2}) + \frac{\rho_f \mu_i}{\triangle t^2}(\widetilde{d}_{i}^{n+1} - 2d_{i}^{n} + d_{i}^{n-1}) + a_0 d_{i}^{n+1} \\ &= \frac{\triangle t^2}{\rho_s h_s} P_{ext,i}^{n+1}.\end{aligned} \tag{4.18}$$

By substituting equation (3.59), equation (4.18) can be rewritten as

$$\begin{aligned}&\frac{\rho_s h_s}{\triangle t^2}(\frac{2d_{m+1,i}^{n+1}}{\omega}-5d_i^n+4d_i^{n-1}-d_i^{n-2})+a_0\frac{d_{m+1,i}^{n+1}}{\omega}\\&=\left(\frac{1-\omega}{\omega}\right)\left(\frac{2\rho_s h_s}{\triangle t^2}+a_0\right)d_{m,i}^{n+1}-\frac{\rho_f\mu_i}{\triangle t^2}(d_{m,i}^{n+1}-2d_i^n+d_i^{n-1})\\&+\frac{\triangle t^2}{\rho_s h_s}P_{ext,i}^{n+1},\end{aligned}\tag{4.19}$$

$$\begin{aligned}\frac{1}{\omega}\left(\frac{2\rho_s h_s}{\triangle t^2}+a_0\right)d_{m+1,i}^{n+1}=&\left[\left(\frac{1-\omega}{\omega}\right)\left(\frac{2\rho_s h_s}{\triangle t^2}+a_0\right)-\frac{\rho_f\mu_i}{\triangle t^2}\right]d_{m,i}^{n+1}\\&+g\left(d_i^n,d_i^{n-1},d_i^{n-2},P_{ext,i}^{n+1}\right),\end{aligned}\tag{4.20}$$

$$\frac{d_{m+1,i}^{n+1}}{d_{m,i}^{n+1}}\approx\frac{\left[\left(\frac{1-\omega}{\omega}\right)\left(\frac{2\rho_s h_s}{\triangle t^2}+a_0\right)-\frac{\rho_f\mu_i}{\triangle t^2}\right]}{\frac{1}{\omega}\left(\frac{2\rho_s h_s}{\triangle t^2}+a_0\right)}=\underbrace{1-\frac{\omega\left(2\rho_s h_s+a_0\triangle t^2+\rho_f\mu_i\right)}{2\rho_s h_s+a_0\triangle t^2}}_{Growth factor,G}.\tag{4.21}$$

Absolute value of the growth factor has to be less than unity if the solution is to be stable. That is

$$|G|=\left|1-\frac{\omega\left(2\rho_s h_s+a_0\triangle t^2+\rho_f\mu_{max}\right)}{2\rho_s h_s+a_0\triangle t^2}\right|<1,\tag{4.22}$$

$$0<\omega<\frac{4\rho_s h_s+2a_0\triangle t^2}{2\rho_s h_s+a_0\triangle t^2+\rho_f\mu_{max}}.\tag{4.23}$$

From equation (4.23), it is obvious that not only the material and geometrical properites such as density of both fluid and solid, Young modulus and eigenvalue of added mass matrix has influence on the allowable relaxation factor but also the

time step size of the calculation. It can be further put that if the time step size is very small (approach to zero), then equation (4.23) becomes

$$0 < \omega < \frac{4}{2 + \frac{\rho_f \mu_{max}}{\rho_s h_s}}. \tag{4.24}$$

Here, it is proved that if time step size is very small, the Young modulus is no longer a factor determining the criteria for stability of implicit algorithm. This also means that the critical value of relaxation factor converges and does not vary with a further decrease in time step size. Moreover, it can also be concluded that if $\rho_f \mu_{max} = \rho_s h_s$, then the relaxation factor has to be strictly less than $\frac{4}{3}$ to allow convergence of solution.

4.3.3 Generalization of stability condition

We recall equations (3.25) and (3.26) which are used as time integration method of structural analysis.

$$\begin{aligned} \dot{d}^{n+1} &= \dot{d}^n + (1-\delta)\triangle t \ddot{d}^n + \delta \triangle t \ddot{d}^{n+1}, \\ \ddot{d}^{n+1} &= \frac{1}{\alpha \triangle t^2}\left[d^{n+1} - d^n - \triangle t \dot{d}^n - \left(\frac{1}{2} - \alpha\right)\triangle t^2 \ddot{d}^n\right]. \end{aligned}$$

We also recall that

$$\ddot{d}^{\alpha} = (1-\alpha_m)\,\ddot{d}^{n+1} + \alpha_m \ddot{d}^n.$$

Therefore, structural acceleration can be rewritten as

$$\begin{aligned} \ddot{d}^{n+1,\alpha} = (1-\alpha_m)\frac{1}{\alpha \triangle t^2}&\left[d^{n+1} - d^n - \triangle t \dot{d}^n - \left(\frac{1}{2} - \alpha\right)\triangle t^2 \ddot{d}^n\right] \\ +\frac{\alpha_m}{\alpha \triangle t^2}&\left[d^n - d^{n-1} - \triangle t \dot{d}^{n-1} - \left(\frac{1}{2} - \alpha\right)\triangle t^2 \ddot{d}^{n-1}\right]. \end{aligned} \tag{4.25}$$

According to the mathematical analysis for our two time integration methods, it is obvious that the general version of conditon can be casted as

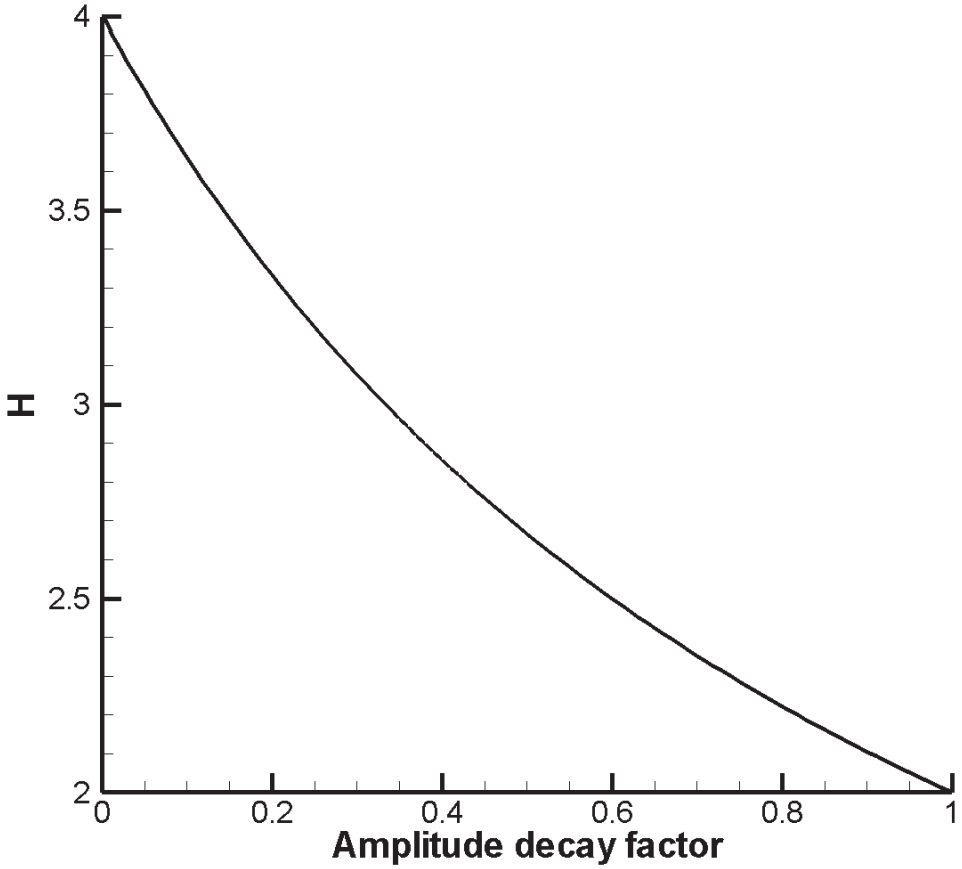

Figure 4.2: Plot of $\frac{4}{(1+\gamma)}$ in the range of γ between zero and one.

$$0 < \omega < 2 \left[\frac{\left(\frac{(1-\alpha_m)}{\alpha}\right) \rho_s h_s + a_0 \triangle t^2}{\left(\frac{(1-\alpha_m)}{\alpha}\right) \rho_s h_s + a_0 \triangle t^2 + \rho_f \mu_{max}} \right]. \tag{4.26}$$

In order to optimize the stability of FSI solution using the generalized-α time integration scheme, $\frac{(1-\alpha_m)}{\alpha}$ should be maximized. In an attempt to find the maximum value of this term, it is important that conditions of stability and accuracy of structural solution are also satisfied. According to (*ANSYS Inc. 2009. ANSYS CFX-Solver Theory Guide*, n.d.),

$$\frac{(1-\alpha_m)}{\alpha} = \frac{4}{(1+\gamma)}. \tag{4.27}$$

For maintaining stability and accuracy when using the time integration method, the following condition must be satisfied.

$$0 \geq \gamma \geq 1. \tag{4.28}$$

4.4 Summary and concluding remarks

In practice, most of physical and numerical properties (such as dimension of problem domain and time step size) are fixed and the combination of their contributions to the stability of the FSI coupling may lead to divergence and failure of solution. Therefore, it is necessary to determine the critical value of relaxation factor which allows the solution to be stable. A similar analysis was done by Causin et al. (2005) but in their work, only the Leap-Frog schemes are used for analysis. Here, in our analysis, we obtain similar conclusions made by them. In our derivations, the critical value of relaxation factor is found to be a function of the following parameters:

- Density of solid and fluid;
- Time step size;
- Young modulus of solid;
- Geometrical properties such as vessel thickness and radius.

From our derivations, the influence of these parameters can be summarized as follows:

$$\left.\begin{array}{r}\text{Higher density ratio}\\ \text{Smaller time step size}\\ \text{Smaller Young modulus}\\ \text{Larger respective eigenvalue}\end{array}\right\} \rightarrow \text{Smaller critical value of relaxation factor.}$$

Apart from the above findings, this work originally contributes to the FSI research community by revealing the influence of numerical damping applied through structural time integration schemes on the stability condition of partitioned FSI. It is found that the larger amount of numerical damping in structural time integration schemes lead to stricter stability conditions. This is also proven with a set of numerical results which will be mentioned in Chapter 5.

These findings from our derivations can provide researchers some quidances when partitioned approach FSI with under-relaxation technique is used. However, these results need to be verified with numerical simulations to confirm their validity which is discussed in Chapter 5.

Chapter 5

Validation and numerical results

In this chapter, a series of numerical tests conducted on both under-relaxation technique and artificial compressibility methods implementing fluid-structure interaction problems and using the different time integration method discussed in previous chapters are presented. The main purpose of these tests is to provide a numerical validation of the theoretical results mentioned in Chapter 4. Every sensitivity analysis in this chapter was obtained in the time interval $[0, T_{max} = 0.011s]$.

5.1 Validation

In this section a validation is proveded for justifing the accuracy of the relaxation factor technique and artificial compressibility used in this work. Pressure pulse velocity has been widely used as an indicator of blood vessel health. In the past, only physical experiment and analytical solutions are available for obtaining the pulse velocity. Although these analytical solutions are only used for simple geometries of blood vessel, they can serve as solid verification for numerical simulation, which are becoming popular nowadays. Therefore, a simulation of fluid-structure interaction for calculating pressure pulse velocity in a compliant vessel is conducted to verify our numerical results by comparing with analytical solutions such as the Moen-Korteweg equation. The results presented in this section are obtained by using the

same method as that used in the next section where numerical results are presented to confirm our theoretical results.

5.1.1 Geometric and material descriptions

The geometrical model of three-dimensional tube is shown in Figure 4.1. The cylindrical domain has a radius of 0.0005 m and a total length of 0.06 m. The working fluid is modelled as incompressible fluid with fluid viscosity and density of 0.01 $Pa \cdot s$ and 1,000 $\frac{kg}{m^3}$ respectively. On the other hand, the compliant vessel is modelled as isotropic material with Poisson ratio and density of 0.3 and 1,000 $\frac{kg}{m^3}$ respectively. Young modulus of the solid structure is varied between 50 and 200 kPa.

5.1.2 Computational domain

Figure 6.3 shows the computational mesh of both solid and fluid domains which consist of 1,800 and 24,674 elements respectively. In the fluid mesh, the laminar boundary layer has 5 layers of thin hexagonal elements, while 4 layers is used for the thickness of solid domain. In this work, only one set of computational grids are used for obtaining numerical results as our main aim is to validate the theoretical results mentioned above.

5.1.3 Analytical solutions

In this section, analytical solutions developed for pressure wave velocity are discussed below.

Moen-Korteweg equation

The Moen-Korteweg equation (Korteweg, 1878; Moens, 1878) can be written as

$$c = \sqrt{\frac{Eh_s}{2R_s\rho_s}}, \tag{5.1}$$

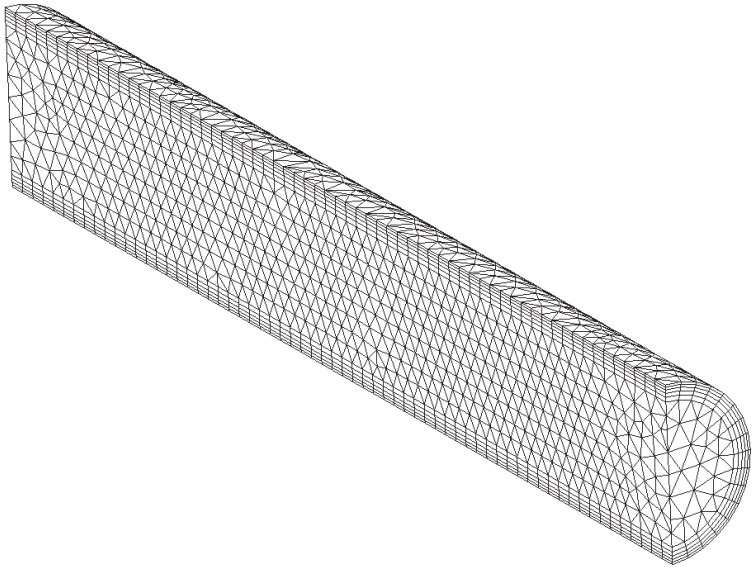

(a) Fluid mesh

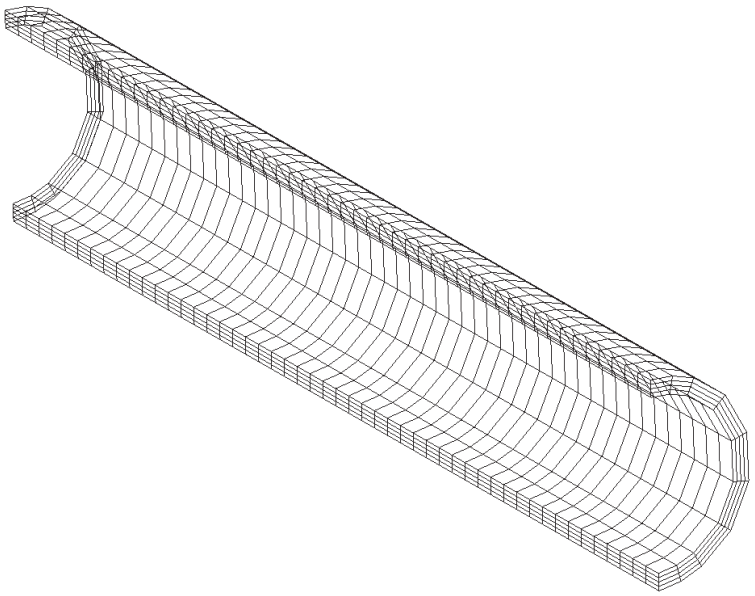

(b) Solid mesh

Figure 5.1: Computational meshes of fluid and solid domain.

where c represents the pressure wave velocity, E is Young modulus, h_s is thickness of the flexible cylindrical tube, R_s is the radius of the flexible cylindrical tube, ρ_s is the working fluid density.

Streeter and Wiley equation

The Wiley and Streeter equation (Wylie and Streeter, 1983) can be written as

$$c = \varphi c_f^*, \tag{5.2}$$

where φ is the stress factor, c_f^* is the corrected pressure wave velocity. Here,

$$c_f^* \sqrt{\frac{E}{\rho_f}\left(\frac{(2r+2h_s)^2}{h_s(2r+h_s)} - 2(1-\nu)\right)^{-1}}, \tag{5.3}$$

$$\varphi = \sqrt{1-\nu^2\left[1 - \frac{E}{K}\left(\frac{h_s}{2r}\right)\left(1 - \frac{K\rho_f}{E\rho_s}\right)\right]^{-1}}. \tag{5.4}$$

5.1.4 Comparison between numerical and analytical solutions

In this section, a case study which is used for validating our numerical results is discussed. The relationship between pressure wave velocity and Young modulus of flexible vessel is shown to illustrate adequate accuracy of the results calculated using the under-relaxation and artificial compressibility as shown in Figure 5.2. Moen-Kortweg equation is the most simple analytical solution for estimating the propagation speed of pressure wave. However a more accurate solution was proposed by Wylie and Streeter (1983). The Streeter and Wiley equation accounts for some important physical properties such as fluid compressibility, flexibility of solid. In their work, the corrected pressure wave velocity, c_f^*, which is expressed in equation (5.3) is aguably the most accurate analytical expression available in the literature for calculating pressure wave speed as it takes the axial stress into consideration by

applying φ. Figure 5.2 shows that our FSI numerical results generated using both under-relaxation and artificial compressibility are in agreement with c_f^*.

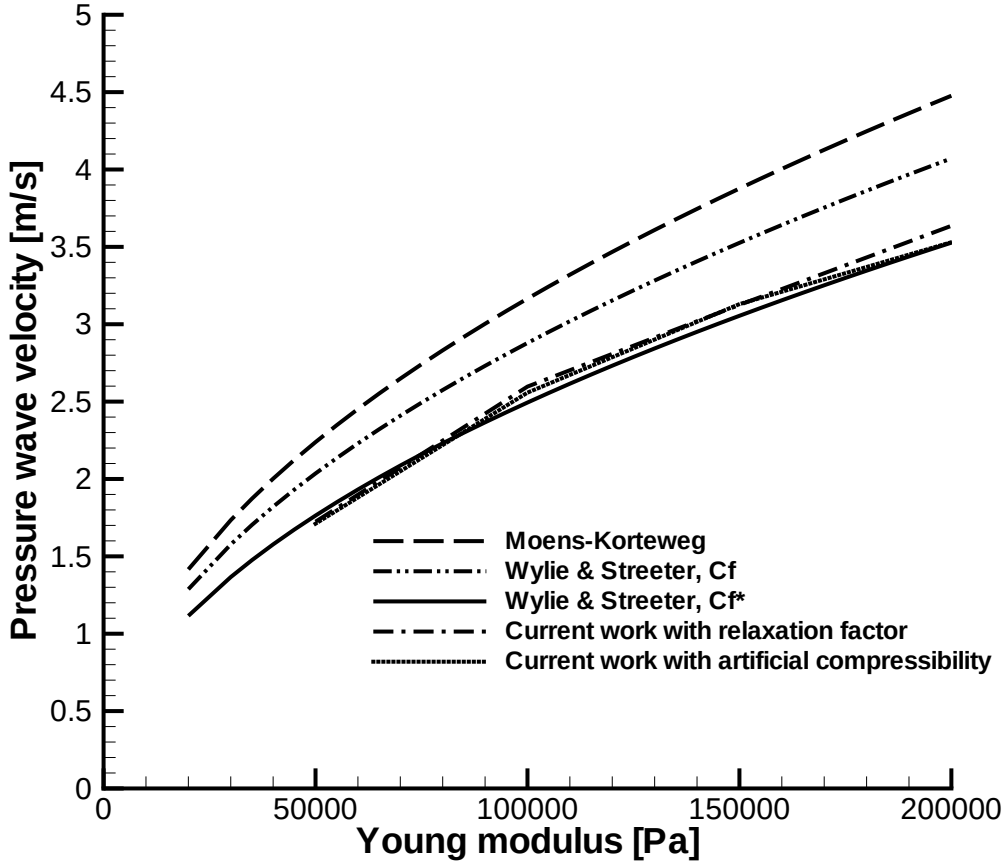

Figure 5.2: Relationship between pressure wave velocity and Young modulus of flexible vessel.

The pressure pulse velocity is calculated by measuring the location of maximum deformation at two different times, which are the sixth and eleventh millisecond. The distance between the two locations is divided by time difference of five milliseconds in order to get the velocity of the pressure pulse. The location of maximum deformation is used for the measurement as it represents the centre of the pressure

wave. Figures 5.3 and 5.4 shows the contour plot of pressure wave propagation along the flexible cylindrical vessel at various Young modulus and simulation time levels.

5.2 Numerical results

In this section, we present a set of numerical results with different structural time integration scheme by varying the amplitude decay factor. The main purpose of these results is to confirm our theoretical results. In our default configuration, which is used as a reference to compare with other cases, we set vessel radius $r = 0.005$ m, vessel lenght L=0.06 m, vessel thickness h_s=0.001 m, solid density ρ_s=30,000 $\frac{kg}{m^3}$, Young modulus E = 750,000 Pa, Poisson ratio $\nu = 0.5$, fluid density ρ_f=1,000 $\frac{kg}{m^3}$ and fluid dynamic viscosity $\mu_f = 0.01$ Pa $\cdot$ s. At initial condition, fluid is set to be at rest and pressure pulse with peak of 2,000 Pa is imposed at the inlet. The total duration of our observation, T_{max} for instability is 0.02 second for different values of amplitude decay factor γ. In the majority of test cases, the instability occurs at the beginning of the calculation before reaching T_{max}. In our results, fluid acceleration is discretized by the second order accurate backward Euler scheme except for those results presented in Table 5.2, which is obtained by the use of the first order accurate backward Euler scheme and for illustrating the influence of numerical schemes used for fluid acceleration.

5.2.1 Influence of structural time integration scheme

We observe a significant dependence on the amplitude decay factor, and namely the required relaxation factor for maintaining stability becomes greater as the amplitude decay factor approaches zero whereby the structural time integration sheme becomes the average acceleration method. The numerical tests agree with our theoretical results. In particular, they confirm that the critical relaxation factor increases with the decrease of the structural amplitude decay factor. Moreover, it is observed that the required values of relaxation factor when using amplitude decay factor of zero

(a) E = 50 kPa, t= 6 ms

(b) E = 100 kPa, t= 6 ms

(c) E = 150 kPa, t= 6 ms

(d) E = 200 kPa, t= 6 ms

Figure 5.3: Pressure wave propagation along the flexible cylindrical vessel with various Young modulus at 6 ms.

(a) E = 50 kPa, t= 11 ms

(b) E = 100 kPa, t= 11 ms

(c) E = 150 kPa, t= 11 ms

(d) E = 200 kPa, t= 11 ms

Figure 5.4: Pressure wave propagation along the flexible cylindrical vessel with various Young modulus at 11 ms.

can be approximately 30 percent higher than that when using amplitude decay factor of one as shown in Table 6.1.

Relaxation factor, ω	$\gamma = 0$	$\gamma = 0.25$	$\gamma = 0.5$	$\gamma = 0.75$	$\gamma = 1$
0.685	√	√	√	√	√
0.716	√	√	√	√	x
0.756	√	√	√	x	x
0.812	√	√	x	x	x
0.891	√	x	x	x	x
0.9	x	x	x	x	x

Table 5.1: Influence of amplitude decay factor on the critical relaxation factor when time step size is 0.001s.

5.2.2 Influence of fluid time integration scheme

Here, we prove numerically the influence of the fluid time integration scheme on the FSI stability condition. By comparing Figures 6.1 and 5.2 , it is clear that changing the discretization scheme used for fluid acceleration from the second to the first order accurate backward Euler scheme results in the value of critical relaxation factor based on each value of γ to increase considerably.

Relaxation factor, ω	$\gamma = 0$	$\gamma = 0.25$	$\gamma = 0.5$	$\gamma = 0.75$	$\gamma = 1$
0.691	√	√	√	√	√
0.728	√	√	√	√	x
0.776	√	√	√	x	x
0.834	√	√	x	x	x
0.913	√	x	x	x	x
0.9	x	x	x	x	x

Table 5.2: The critical relaxation factors when time step size is 0.001s and first order accurate backward Euler scheme is used for fluid acceleration.

5.2.3 Influence of time step size

The influence of time step size on the stability of FSI calculation is discussed. Here, we consider the same domain of calculation and physical parameter as before, only time step size used for calculation is reduced from 0.001 to 0.0001 s. It is found that time step size also has considerable impact on the performance of FSI simulation. From Table 5.3, it is shown that the values of critical relaxation factor corresponding with various values of amplitude decay factor decrease considerably when time step size is reduced. Moreover, when time step size is futher reduced to 0.00001 s, the change in critical relaxation factor almost remains unchanged. This observation agrees well with our theoretical results that when time step size approaches zero, the value of critical relaxation factor converges as shown in Table 5.4.

Relaxation factor, ω	$\gamma = 0$	$\gamma = 0.25$	$\gamma = 0.5$	$\gamma = 0.75$	$\gamma = 1$
0.523	√	√	√	√	√
0.563	√	√	√	√	x
0.617	√	√	√	x	x
0.705	√	√	x	x	x
0.815	√	x	x	x	x
0.9	x	x	x	x	x

Table 5.3: Influence of amplitude decay factor on required density ratio when time step size is 0.0001s.

Relaxation factor, ω	$\gamma = 0$	$\gamma = 0.25$	$\gamma = 0.5$	$\gamma = 0.75$	$\gamma = 1$
0.6523	√	√	√	√	√
0.563	√	√	√	√	x
0.615	√	√	√	x	x
0.704	√	√	x	x	x
0.813	√	x	x	x	x
0.9	x	x	x	x	x

Table 5.4: Influence of amplitude decay factor on required density ratio when time step size is 0.00001s.

5.2.4 Influence of density ratio

The influence of density ratio to the performance of FSI calculation is presented below. Here, the relationship between density ratio $\frac{\rho_f}{\rho_s}$ and the critical relaxation factor is based on different values of amplitude decay factor. Figure 6.5 shows that the impact the density ratio has on variation of critical density ratio is high only when density ratio is relatively small. Its influence tends to vanish as we increase the density ratio value. At a constant $\frac{\rho_f}{\rho_s} = 0.033$, the difference in the critical relaxation factor at $\gamma = 0$ and $\gamma = 1$ is considerably high, while it is negligible at $\frac{\rho_f}{\rho_s} = 1$.

5.2.5 Influence of vessel radius

Here, the dependency of critical relaxation factor on vessel radius is explained. The data provided in 5.5 is achieved by increasing the radius from 0.5 to 0.7 cm. With $\gamma = 1$, the solution will be stable if the relaxation factor is set at lower or equal to 0.683, while this threshold increases up to 0.935 when γ is set to zero. By comparing 5.5 to 6.1, it can clearly be seen that the value of critical relaxation factor is inversely proportional to the value of amplitude decay factor.

Relaxation factor, ω	$\gamma = 0$	$\gamma = 0.25$	$\gamma = 0.5$	$\gamma = 0.75$	$\gamma = 1$
0.683	√	√	√	√	√
0.711	√	√	√	√	x
0.754	√	√	√	x	x
0.835	√	√	x	x	x
0.935	√	x	x	x	x
0.95	x	x	x	x	x

Table 5.5: The critical value of relaxation factor when using time step size is 0.001s and radius is increased to 0.7 cm

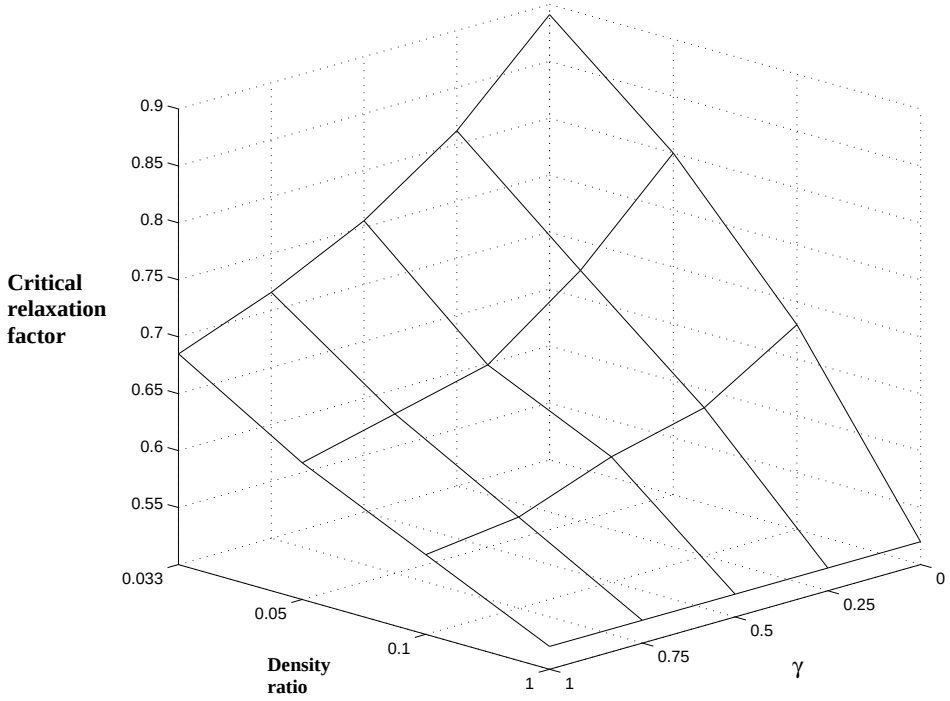

Figure 5.5: Influence of density ratio and amplitude decay factor on the impact of critical relaxation factor.

5.3 Implicit solution using artificial compressibility

In this section, numerical results are used to validate our theoretical results, which suggests that FSI coupling based on artificial compressiblity is unconditionally stable. It is found that the FSI coupling is stable regardless of the following factors that commonly affect stability of coupling if it is based on under-relaxation technique.

- applied numerical damping
- density ratio
- time step size
- geometrical properties such as radius and thickness of vessel

The only factor that dictates the success of FSI coupling using artificial compressibility is the relationship between deformation and pressure, K_{ac}. Therefore, the selection of this value is critical. The calculation of this parameter was suggested in the work by Raback et al. (2001). We recall from Figure 5.2 that the results obtained by using artificial compressibility are close to those of under-relaxation technique.

5.4 Performance comparision between artificial compressibility and under-relaxation technique

Apart from being applicable to solving problems with higher density ratio, artificial compressibility has a superior performance to the under-relaxation technique when solving the wave propagation along a flexible cylindrical tube as shown in Table 5.6. This comparison is achieved by looking at the computational time required for solving the problem between the two techniques. The total time and time step size are 11 and 1 ms respectively. For each case, no numerical damping is applied since it

has been proven that it performs best with no numerical damping. For cases with artificial compressibility, K_{ac} are chosen according to the work done by Raback et al. (2001). In each case, convergence of interface loads are satisfied by allowing enough coupling iterations. Density of fluid is fixed at 1000 $\frac{kg}{m^3}$ while density of solid is varied according to the density ratio. Young modulus and poisson ratio of the tube is held constant at 0.75 MPa and 0.49 respectively. Each case is run on a workstation with Intel duo core2 CPU (3.16 GHz) which has 3.48 Gigabyte of RAM. The same set of computational meshes mentioned in Section 5.1.2 are used for each case.

From Table 5.6, as we increase the density ratio from 0.033 to 1.0, the computational time required for computing with under-relaxation technique increases dramatically from 19 minutes and 8 seconds to almost 15 hours. This trend relates to the decrease of critical value of relaxation factor that allow stable solution which leads to a larger number of coupling iterations needed for reaching convergence criteria. In contrast, the computational time of those cases using artificial compressibility only rise slightly from 19 minutes and 38 seconds to 30 minutes and 43 seconds. With this methods, there is only a small change in the average of required number of coupling iteractions from 3.27 to 5.00. It is therefore clear that artificial compressibility is a more efficient method for solving problems with high density ratio than the under-relaxation technique.

However, it should be noted that at a low density ratio such as 0.033 and 0.05, the computing time when using under-relaxation technique is slightly smaller than when using artificial compressibility, even though the averaged required numbers of coupling iterations per time step for artificial compressibility is much smaller than those of under-relaxation technique. This is because artificial compressiblity requires more time for calculation and data storage process in each iteration.

5.5 Summary and concluding remarks

In this chapter, a number of simulations are conducted to confirm our theoretical results in Chapter 4. In Chapter 4, pressure wave propagation in a straight flexible vessel, which is a phenomenon relevant in many engineering applications such as flow

	Under-relaxation			**Artificial compressibility**	
Density ratio, $\frac{\rho_f}{\rho_s}$	Computational time when using under-relaxation technique	Critical value of relaxation factor	Averaged required number of coupling iterations per time step	Computational time when using artificial compressibility	Averaged required number of coupling iterations per time step
0.033	19 mins and 8 secs	0.88	8.27	19 mins and 38 secs	3.27
0.05	20 mins and 1 secs	0.52	8.91	21 mins and 21 secs	3.45
0.1	33 mins and 18 secs	0.31	15.36	25 mins and 2 secs	4.00
0.2	1 hr, 40 mins and 35 secs	0.11	48.64	27 mins and 11 secs	4.36
0.5	5 hrs, 54 mins and 51 secs	0.04	98.57	30 mins and 4 secs	4.73
1.0	14 hrs, 51 mins and 17 secs	0.02	256.78	30 mins and 43 secs	5.00

Table 5.6: Comparison between the consumed computation time when using artificial compressibility and under-relaxation technique.

in artery, is choosen for analyzing stability condition theoretically. In this chapter, the same problem is solved using the numerical technique in order to confirm those results. Our numerical outcomes appear to agree well with the theoretical ones. These outcomes can be summarized as follows:

- Structural time integration schemes with less numerical damping allow larger critical value of relaxation factor. However, the effect of the numerical damping becomes neglegible when density ratio is high.

- The selection of fluid time integration schemes also has considerable influence on the critical value of relaxation factor. It is found that the 1st order accurate backward Euler gives better stability to FSI solution.

- Smaller time step size leads to smaller critical value of relaxation factor. However, the influence of time step size disappears when we keep reducing it to a very small value. In other words, the critical value of relaxation factor almost stays unchanged with the decrease in time step size when the time step size is very small.

- Geometrical properties such as radius of vessel also has an impact on the critical value of relaxation factor. That is when radius of the flexible vessel is greater, the stability condition can become deteriorated.

To ensure that our method in producing these numerical results is accurate, they are validated against a number of well-defined analytical solutions which are used to estimate the velocity pressure wave propagation. Our results go considerably well with them and therefore ensure the accuracy of our results.

Due to the limited improvement varying numerical damping in structural time integration scheme, the artificial compressiblity technique is also analyzed and resulted a more versatile technique for a wider range of applications as it provides a reasonably good performance regardless of density of fluid and solid. In this technique, the only key parameter, which needs some attention from the user, is the artificial bulk modulus and it is not restricted by physical properties of the problem.

Moreover, the performance of artificial compressibility is superior to that of relaxation factor as shown in Table 5.6. Computational time can be reduced significantly with this technique.

It is therefore recommended to use artificial compressibility for FSI problems with high density ratio. In Chapter 6, this method is used for analysing Atherosclerosis in carotid bifurcation in order to confirm its practical use. This engieering problem is selected because it has the characteristic of high density ratio and is therefore suitable for the purpose of demonstration of practicality of artificial compressiblity.

Chapter 6

Fluid-structure interaction in carotid bifurcation

The main purpose of this chapter is to demonstrate the practicality of FSI with artificial compressibility for solving challenging real world engineering applications. In this work, fluid-structure interaction of atherosclerosis in carotid bifurcation is selected as it poses real issues of added mass stability.

6.1 Abstract

It has been suggested that atherosclerosis in carotid bifurcation depends on flow parameters such as wall shear stress, flow pulsatility and blood pressure. However, it is still not clearly verified how the disease becomes aggravated when plaque experiences high level of shear stress during advanced stages of this disease. Despite the significant effect of arterial compliance on hemodynamics, most previous works are based on the assumption of modelling a rigid vessel. In this work, fluid and structural properties in idealistic geometries are analyzed by using fluid-structure interaction (FSI). In our results, the relationship among blood pressure, stenotic compression and deformation was established. It shows that high level compression

occurs at the stenotic apex, and can potentially be responsible for plaque progression. Moreover, wall shear stress and deformation are significantly affected by the degree of stenosis.

6.2 Introduction

6.2.1 General background of atherosclerosis

Atherosclerosis is one of the most life-threatening diseases in developed countries. The main characteristic of this disease is the narrowing of blood vessels that results in occlusion and thus causes insufficient supply of blood to the brain and heart (Falk, 1991; Falk, 1992). Intermittently, this can lead to ischemia and heart attack. In Australia, stroke is the cause of 9,006 deaths which is almost 7 percent of all deaths in 2003 (Senes, 2006). This fact has motivated a rise in stroke related research activity to rise around the globe in the past decade. It has been well understood that stroke, due to atherosclerosis, occurs mainly because of the deficiency of oxygen to the brain, causing brain cells to die. One of the most relevant atherosclerotic sites for the occurrence of stoke is carotid bifurcation. This is probably because it consists of multiple curvilinear features, which will lead to a favoured condition of the disease, especially, at the outer wall of the inner carotid artery (ICA) sinus (Zarins et al., 1983; Samuel et al., 2008; Ku et al., 1985). Other components of bifurcation are the common (CCA) and external (ECA) carotid arteries.

6.2.2 Hypothesis on the developement of artherosclerosis

There has been intensive research that focuses on finding the cause of atherscleresis (e.g. Caro et al., 1971; Ku et al., 1985; Glagov et al., 1989). Although understanding the causative mechanism is still not clear, many researchers suggest that thickening of the vessel is stimulated by low levels of wall shear stress (e.g. Friedman et al., 1989; Lee and Chiu, 1996; Giddens et al., 1993; Kleinstreuer et al., 2001; Nerem, 1992). It is believed that low and oscillating wall shear stress increases

the risk of occurrence for the disease while high wall shear stress tends to suppress it (Friedman et al., 1986; Giddens et al., 1993; Ku et al., 1985). However, this is not always true since it has been discovered that the disease can also develop when the vessel is undergoing high shear stress (Joshi et al., 2004; Wentzel et al., 2003). An example of this occurrence is at the apex of the stenosis (at advanced stages of the disease) and the bifurcation point. Although these two regions experience high shear stress, plaque can still grow. Tang et al. (2008) advocates that beside low and oscillating wall shear stress, the intramural stress of the wall may also be responsible for the progress of plaque at advanced stages by statistically proving that there is a negative correlation between wall thickness increment and structural stress. This induces medical experts to look for other indicators that may have influenced this phenomenon. Mechanical values such as Von Mises and principal stresses have been used in the past to gain understanding of the disease (Salzar et al., 1995; Hariton et al., 2007; Callaghan et al., 2009; Delfino et al., 1997; Thubrikar and Robicsek, 1995; Kaunas et al., 2006; Lee and Xu, 2002). It is found that high mechanical stress occurs mainly at the bifurcation point and the bulb region of bifurcation, which are common locations for atherosclerosis. This suggests strong correlation between the existence of the lesion and mechanical stress (Salzar et al., 1995; Delfino et al., 1997). However, these previous studies only focus on stress level experienced in healthy carotid bifurcations. Therefore, an important question which remains unanswered is "How does the mechanical stresses at these regions vary with different degrees of stenosis". The answer to this question will allow us to better understand the factors that influence the growth of plaque. Deformation pattern of the artery is also studied by Tada and Tarbell (2005) and Ramnarine et al. (2003), but there is no report of the relationship between deformation and atherogenesis.

6.2.3 Types of atherosclerosis

According to (Gregory and Michael, 2008), atherosclerosis can have three main categories. The first category involves atheromatous plaque which has artheroma or lipid pool covered with fibrous cap. The second one is a non-atheromatous plaque

that consists of connective tissues with admixed smooth muscle cells. The third one is calcified plaque. The atheromatous plaque is known to be the most common of all three categories. This can be the important reason why in recent years, most past studies focused on atheromatous (with lipid core) and calcified type of the disease while literature that relate to non-atheromatous (no lipid core) remains scarce. With limited information about non-atheromatous, it is believed that mechanical stresses experienced by this type of plaque can be quite different from the other types. For example, atheromatous plaque is mainly subjected to high tensile stress, while non-atheromatous plaque is subjected to compressive stress. One may argue that non-athermatous is rare and its behavior might be trivial. Therefore, it is important to emphasize that even though the lipidless plaque has a low percentage of occurance compared to other types of this disease, it cannot be ignored when considering the total number of patients suffering from this kind of disease. This fact makes it worthwhile to try investigating the behaviour of non-atheromatous plaque in order to provide suitable treatment for the patients. Moreover, the study of its interaction with blood flow may also help researchers to gain better understanding of plaque with soft lipid.

6.2.4 Clinical implications of blood pressure and heart rate

There have been many clinical reports that suggest a relationship between heart rate and the occurance of atherosclerotic plaque (e.g. Giannoglou et al., 2008; Tardif, 2009; Palatini, 1999). These reports recommend that patients with abnormally high blood pressure and heart rate have a higher tendency of developing stenosis in their blood vessels. Many studies also suggest that even a standard heart rate may be already too high and cause atherosclerosis. Therefore, the standard range of blood pressure for healthy blood circulation may need to be revisited. This can be done by studying the influence of blood pressure on the characteristics (such as stresses and blood flow pattern) of atherosclerotic plaque, which may help define a proper range of blood pressure to avoid the development of this disease. To the best of

our knowledge, none of the previous studies have developed a new range of blood pressure to replace the current range used in medical clinics.

6.2.5 Aim and scope

This work aims to analyze how mechanical stress (such as principal stress) is influenced by the degree of stenosis. This allows us to gain more understanding on the formation and the growth of atherosclerotic plaque. The second aim is to explain the relationship between flow characteristics (such as magnitude of hemodynamic pressure, general flow pattern and mechanical stress). Our study focuses on non-atheromatous plaque and utilizes idealistic geometry of carotid bifurcation. A set of important research questions that need to be answered, can be summarized as follows:

- What is the influence of the degree of stenosis on mechanical stress experienced in carotid bifurcation?
- How does the pattern of blood flow change with the presence of stenosis with different sizes?
- Is there any relationship between blood pressure, strucutural stress and deformation of the lesion?

6.3 Methodology

Numerical simulation by computational fluid dynamics (CFD) has an important role nowadays in many engineering fields such as biomechanical engineering. Many research questions could not possibly be acknowledged by only physical experiments. Despite the benefit of great accuracy, these physical experiments have many drawbacks such as difficulties in extracting meaningful data, and cost of operation when compared to CFD. CFD is utilized to overcome these difficulties which occurred in research communities. Moreover, due to the rapid advancement in computer technology, the power of computing has improved significantly over the recent decades.

This makes it possible to incorporate FSI in the numerical simulation and increase the accuracy of flow results that are strongly affected by the deformation of solid. The best example will be the interaction of the artery wall and blood flow. In this work, FSI solutions were obtained using the partitioned approach.

6.3.1 Partitioned approach for fluid-structure interaction

In the partitioned approach, the coupling between solid and fluid solver is performed many times per time step until the convergence of interface variables (such as displacements and pressure) is reached. At each coupling loop, the calculation of blood flow is initiated. Then, calculated pressure field is transferred and used as an applied force in the solid solver in order to calculate deformation of the artery. However, FSI solution using this approach is computationally demanding due to the existence of "Added-mass instability" (Causin et al., 2005; Wall, Gerstenberger, Gamnitzer, Forster and Ramm, 2006; Forster et al., 2007). In order to improve its performance, FSI coupling is stabilized by introducing "Artificial compressibility", which will be discussed further in this work. The tolerance for the interface variables is in the order of 1E-4. The time step size is set to 0.015 s. Results are obtained at the 4th heart cycle to exclude effects from initial conditions.

6.3.2 Idealistic geometry of carotid bifurcation

Physiological geometries have been widely used in the past with the help of magnetic resonance imaging (see Xue et al., 2008; Tang, 2004; Quan et al., 2000). This type of geometry allows the inclusion of complex structures of patient-specific carotid bifurcation, which lead to high accuracy data for the treatment of patients. However, in order to conduct an intensive parametric study, this type of geometry may not be suitable due to its complex features. In contrast, it is widely accepted that simplistic geometry can capture most of the important characteristic of the problem, and it is also simple enough in that parametric research can be implemented (Wong et al., 2006; Wong et al., 2010). In other words, an idealistic carotid bifurcation is suitable for studies, which aim to find the key factors that cause and influence the

disease. In past decades, this type of geometry used by numerous reseachers (e.g. Tada and Tarbell, 2005; Perktold et al., 1991; Ku and Giddens, 1983; Ding et al., 2001), is shown to be able to represent the reasonable flow behaviour of the carotid bifurcation.

In this work, a realistic geometry that is used by Tada and Tarbell (2005) is selected for the modelling of healthy carotid bifurcation as shown in Figure 6.1. In this geometry, a region of sinus is included as the common feature found in carotid bifurcation. Detailed dimensions of the geometry can be presented in Table 6.1. For diseased carotid bifurcation, the location of the stenosis is assumed to be located on the outer wall of the sinus of ICA in order to study the effect of the stenosis to the flow as well as the occurrence of mechanical stress. The degree of stenosis is varied by variation of the ICA diameter at the location where maximum diameter of ICA sinus occurs.

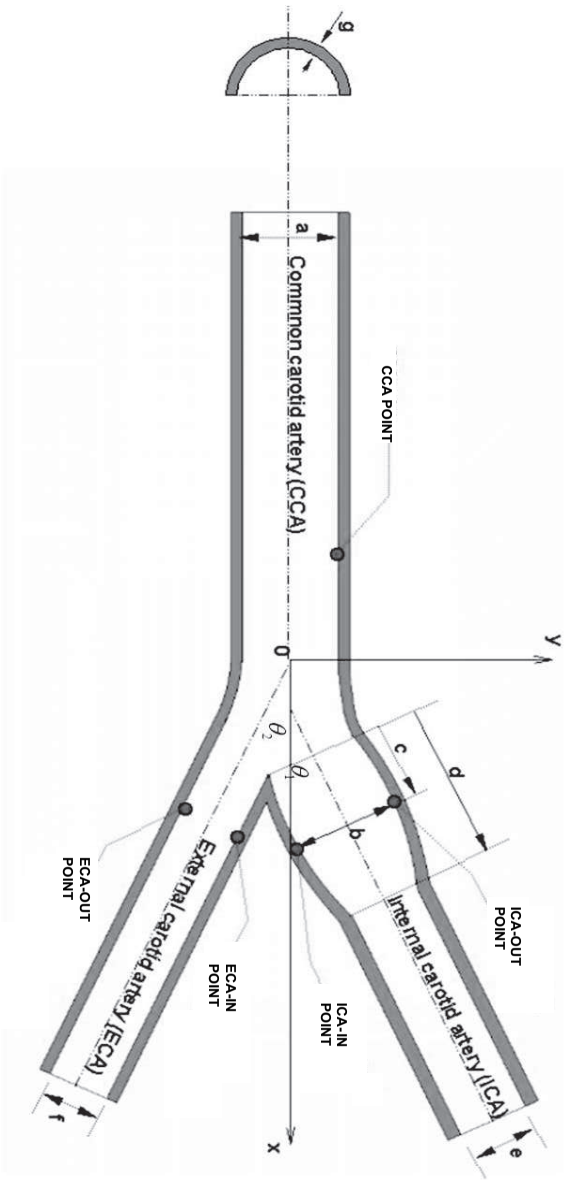

Figure 6.1: Geometry of carotid bifurcation

6.3.3 Computational domain

Figure 6.2 shows an example of the computational grid used in this study. In each case, the mesh will differ slightly due to the degree of stenosis. The mesh consists of three-dimensional tetrahedral and prism and is generated using CFX-mesh software. Grid independence analysis was performed at 3 different mesh refinement levels: coarse (20,000 elements), medium (500,000 elements) and fine (1,000,000 elements). Only 2 percent of the dissimilitude between the fine and medium mesh is observed. Therefore, it is concluded that the fine mesh can be used to obtain grid independent results. All obtained results disserted in the discussion section are the solution of computation performed with the fine mesh.

6.3.4 Boundary conditions and material properties

In the solid domain, each end of the artery (CCA, ICA, ECA) is modelled as fixed support while symmetrical condition is assumed at the plane of the bifurcation. In the fluid domain, boundary condition at the inlet is specified as a time-varying constant pressure that is taken from (Tada and Tarbell, 2005), while outlet boundary conditions at the end of ICA and ECA are set as time-varying mass flow rate as shown in Figure 6.3. Note that the period of pressure pulse is denoted by T (in seconds, s). The time t is normalized by the period of pressure pulse. In addition, no slip condition is specified at the artery wall. The wall is assumed to be smooth. Material models for artery wall were proposed in the past, such as the "Mooney-Rivlin" models (Torii et al., 2009). However, in this work, the arterial wall is prepared as a Hookian and isotropic material for simplicity as used by numerous researchers (e.g. Salzar et al., 1995; Thubrikar and Robicsek, 1995). The blood is modelled as a Newtonian fluid. The properties of the blood and artery are shown in Table 1. The blood flow is modelled as a laminar flow since the highest Reynolds number, even with high degree of stenosis, is approximately 1000 which is still in laminar region.

Descriptions	Symbols	Value	Units
Material properties			
Artery			
Young Modulus	E	5.00E+05	Pa
Poisson ratio	ν	0.5	$-$
Blood			
Density	ρ	1050	$\frac{kg}{m^3}$
Dynamic viscosity	μ	3.50E-03	Pa
Dimensions			
CCA internal diameter	a	0.006	m
Maximum sinus internal diameter	b	0.00666	m
Distance from bifurcation point to location of maximum sinus internal diameter	c	0.00546	m
Total length of sinus	d	0.0138	m
ICA internal diameter	e	0.00444	m
ECA internal diameter	f	0.0039	m
Artery wall thickness	g	0.0007	m
ICA bifurcation angle	θ_1	25	$degree$
ECA bifurcation angle	θ_2	25	$degree$
Parameters for FSI			
Convergence criteria for coupling	ϵ_0	1.00E-05	$-$
Time step size	t_s	0.01	s
Time	t	$-$	s
Pressure pulse period	T	0.92	s

Table 6.1: FSI parameters, material properties and dimensions of carotid bifurcation used in this work

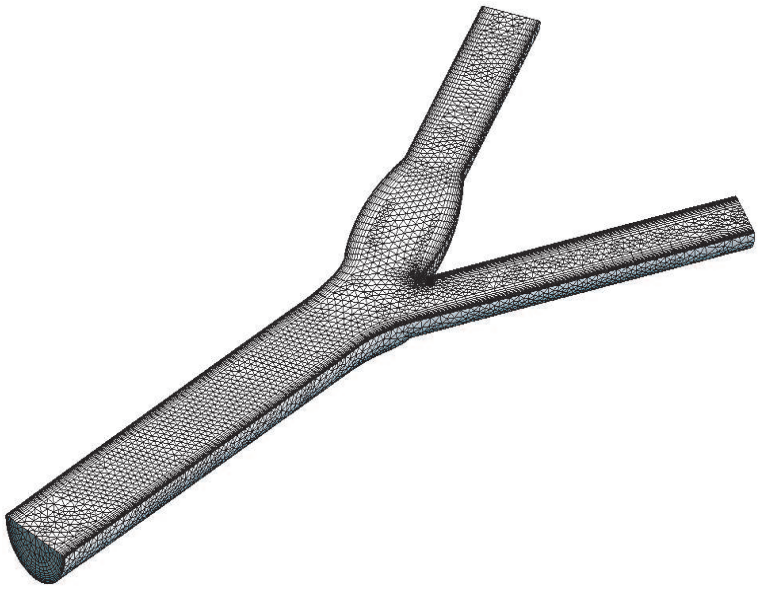

(a) Fluid mesh

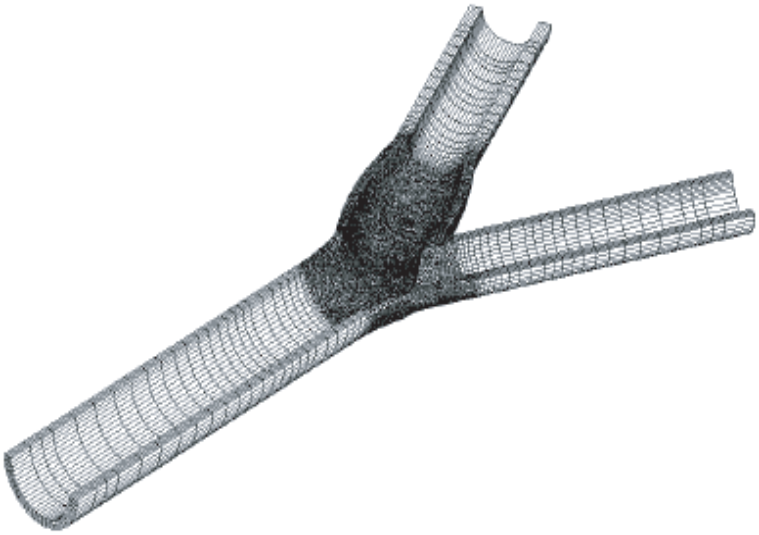

(b) Solid mesh

Figure 6.2: Computational grid used in this work.

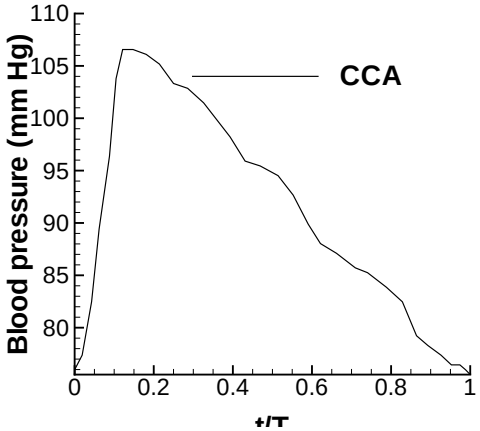

(a) Flow condition at common carotid artery (CCA)

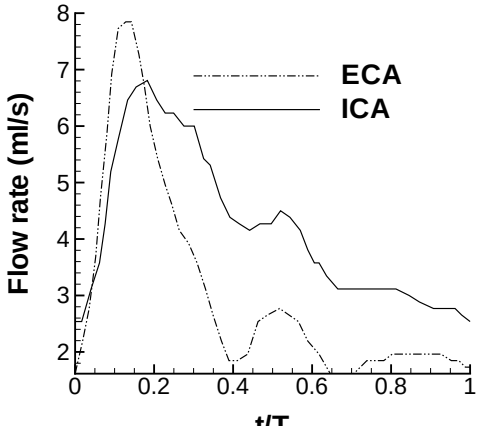

(b) Flow conditions at internal and external carotid artery (ICA and ECA)

Figure 6.3: Flow conditions at the ends of common, internal and external carotid artery.

6.3.5 Flow properties to be examined

The following mechanical parameters are examined in our work:

- Maximum principal stress (MPS) has the implication of the maximum value of stress being applied on a vessel. The contour of MPS on the artery can be presented using logarithmic scale. The region which has a small value represents negative value on the linear scale. In Figure 6.7, we aim to show the location of negative MPS on the artery, therefore only greyscale is utilized. Positive MPS generally means that the stress is tensile whilst a negative sign represents compression.

- Maximum deformation (MD) refers to highest possible displacement of a vessel wall when it is placed under stress. This parameter has an important implication in analysing the MPS and can be used for examining structural vessel changes. The distribution of deformation can be used to analyse plaque developement which is experienced by the plaque.

- Wall shear stress (WSS) is a shearing effect due to blood viscosity. We note that wall shear stress can be oscillating due to the pulsality of blood.

- Pulse pressure refers to transient behavior of blood circulation in vessels due to the periodic pumping action of the heart.

6.4 Results

6.4.1 Healthy carotid bifurcation – normal flow behavior

Figure 6.5(a) shows that in the healthy carotid bifurcation, the blood flow separates at the terminal end of CCA and then forms a recirculation zone inside the ICA sinus. The recirculation zone is located near the outer wall of the sinus, and is relatively large when compared to the diameter of the sinus. The recirculation zone ends at a reattachment point around the distal end of the sinus. Blood motion inside the recirculation zone is slow and backward directing. Consequently, wall shear stress

in this region is also very small and has a negative sign for the large part of the heart cycle as demonstrated in Figure 6.4(b). The results also show that at the beginning of each cycle, the recirculation zone disappears for a short period of time (at $t/T = 0$ to 0.1) since the sign is positive in this period. Moreover, it is recognized that under comparison of our CFD and FSI results, 5 percent of discrepancy in the maximum value of the wall shear stress can be observed. Figures 6.4(a) to 6.4(e) show that the waveforms of the wall shear stress have very similar shapes to the pressure waveform of the blood flow. In contrast, the velocity and wall shear stress at the bifurcation point are very high. The effect of blood vessel compliance reduces the peak of the wall shear stress slightly at each monitoring point as defined in Figure 6.1. From Figure 6.6(a), it is perceived that the region which has the MD situates just upstream of the bifurcation point. Another high deformation region resides near the connection region between the ICA and CCA. It is obvious from Figure 6.7(a) that throughout the healthy carotid bifurcation, the MPS is positive. This would mean that the healthy carotid bifurcation is subjected to tension only.

6.4.2 Diseased carotid bifurcation – parameters affected based on different degrees of stenosis

Flow pattern of blood

At peak flow rate, there is a huge recirculation near the outer wall of ICA sinus. In Figures 6.5(b) and 6.5(c), the 10 and 25 percent blockage cases do not differ much, and flow reversal can be observed at the entire outer wall of the ICA sinus. The region of flow reversal on the outer wall starts from the distal ends of CCA and also at the plaque. The distal end of the plaque seems to be the reattachment point where the flow is divided into two regions of directions, which are the regions of forward and reversal flow. As the flow moves away from this point in both backward and forward directions, acceleration can be observed. In the backward direction, the flow accelerates until it reaches the apex of the stenosis and then decelerates. In contrast, the flow accelerates to achieve a fully developed flow condition near the outlet of ICA in the forward direction. In the separation zone, the velocity and

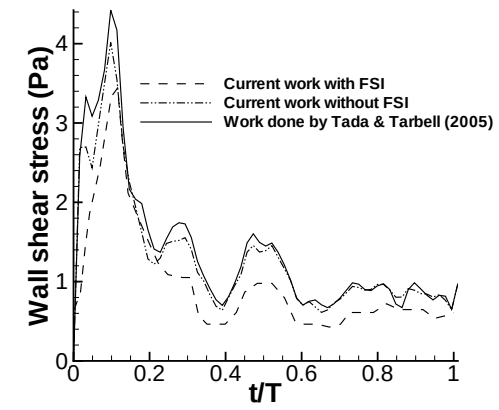

(a) CCA

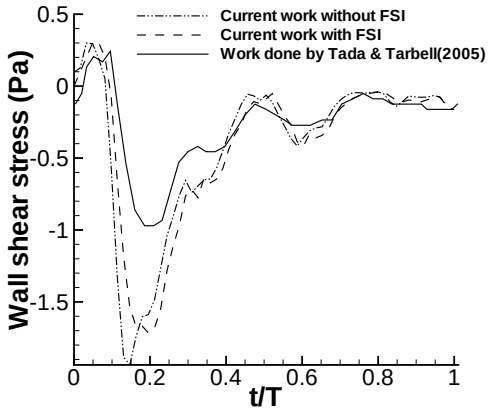

(b) ICA-out

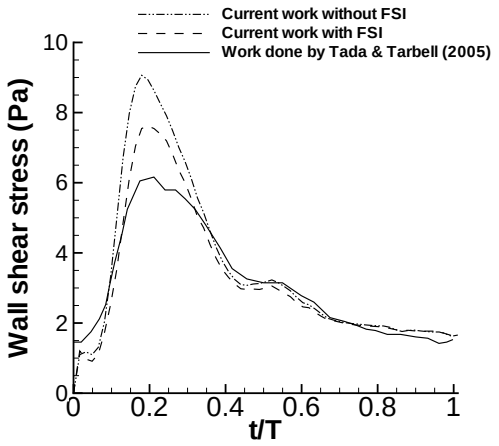

(c) ICA-in

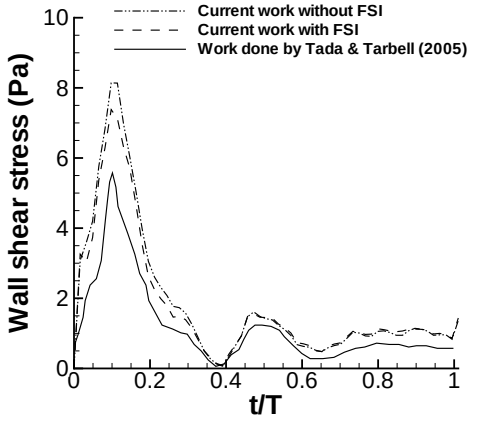

(d) ECA-out

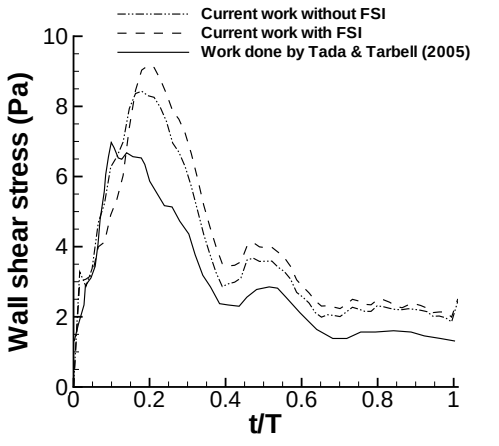

(e) ECA-in

Figure 6.4: Wall shear stress at various monitoring points. The common carotid artery (CCA), inner and outer monitoring points of the internal and external carotid artery (ICA-in and ECA-in, and ICA-out and ECA-out respectively).

shear strain rate are extremely small when compared to those at the inner wall of the section. For 50 percent blockage case, the flow pattern changes drastically as demonstrated in Figure 6.5. The recirculation zone in these two cases only occurs at the proximal and distal ends of the stenosis. Flow near the apex of the stenosis and inner wall of the sinus is not reversed. The velocity magnitude and shear strain rate depends strongly on the degree of stenosis.

Deformation

Figure 6.6 illustrates the region of high deformation in the carotid bifurcation. There are two regions which have relatively high deformation when compared to other regions in the model. These two regions are at the stenosis and upstream to the flow divider. It can be observed that the deformation pattern does not change with the degree of stenosis. However, the magnitude of the deformations in each region changes with time and has variation that corresponds to the pressure waveform (see section 4). Moreover, it also appears that as the degree of stenosis increases, the wall deformation in the stenotic region reduces. In contrast, the deformation in the region near the downstream of the bifurcation point seems to be insensitive to the variation of blockage.

Maximum principal stress

Magnitude of MPS Figure 6.7 shows the region of negative MPS (compression) that can be identified as being on the stenosis while other parts of the bifurcation are under the condition of positive MPS (tension). Only the stenotic region is under compression, while the rest of the artery is under tension. Moreover, as the degree of stenosis is increased, the magnitude of the negative MPS may get larger as illustrated in Figure 6.9. In the case with 10 percent blockage, the region of negative MPS is located in a very confined region on the apex of the stenosis. The negative MPS region tends to expand as the degree of stenosis increases.

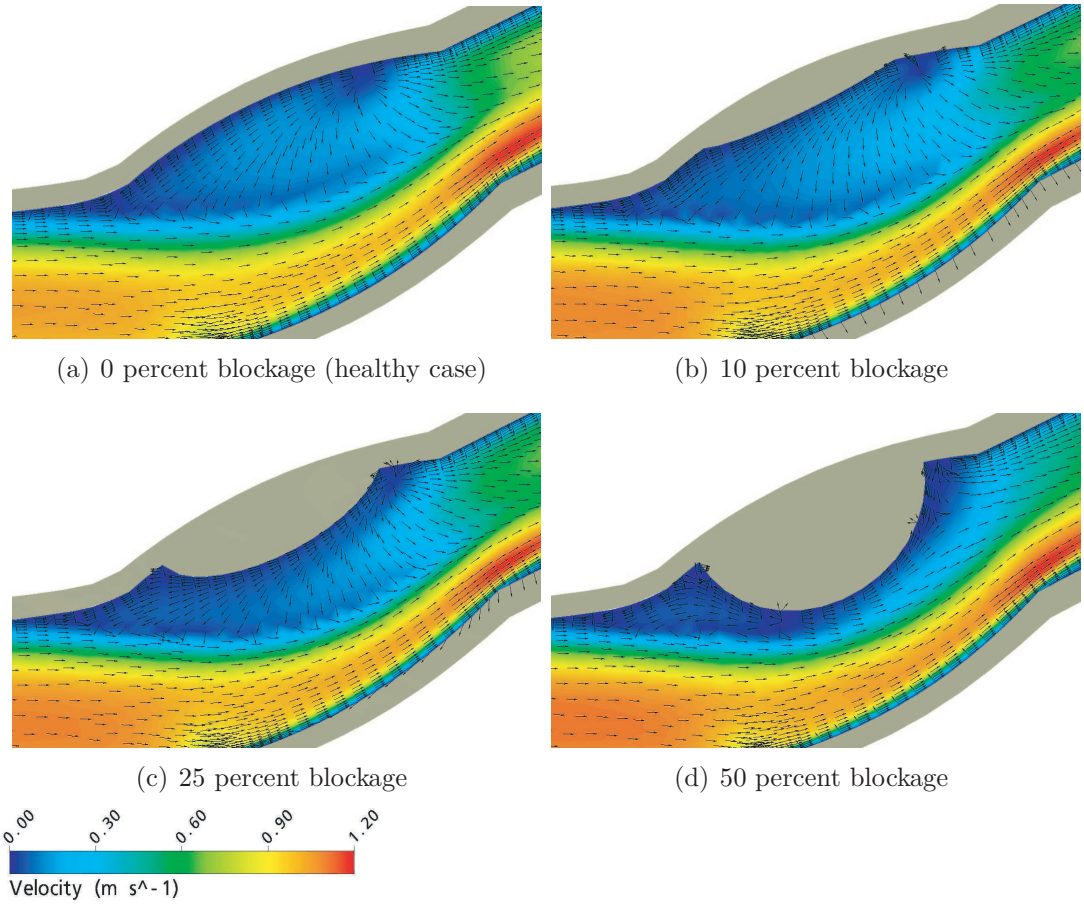

(a) 0 percent blockage (healthy case)

(b) 10 percent blockage

(c) 25 percent blockage

(d) 50 percent blockage

Figure 6.5: Flow pattern in carotid bifurcation with different degrees of stenosis.

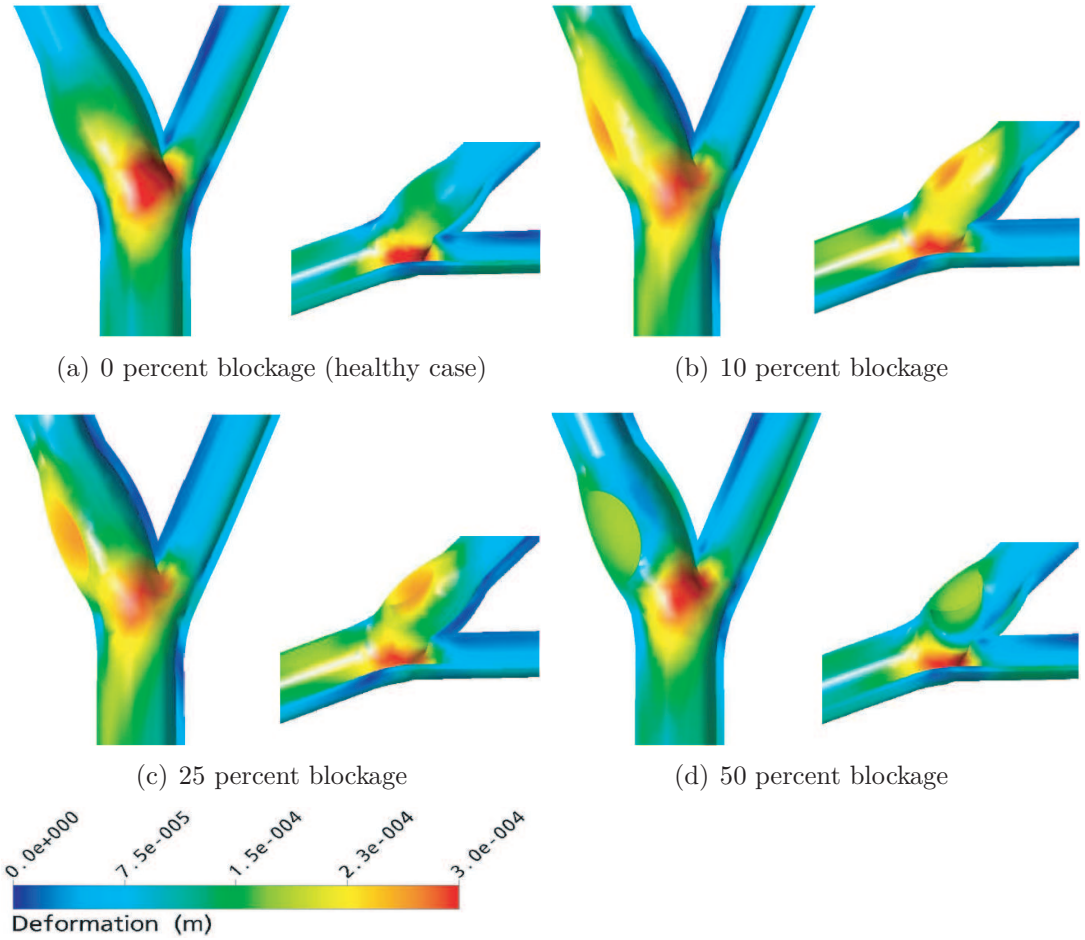

(a) 0 percent blockage (healthy case)

(b) 10 percent blockage

(c) 25 percent blockage

(d) 50 percent blockage

Figure 6.6: Pattern of deformation in carotid bifurcation with different degrees of stenosis.

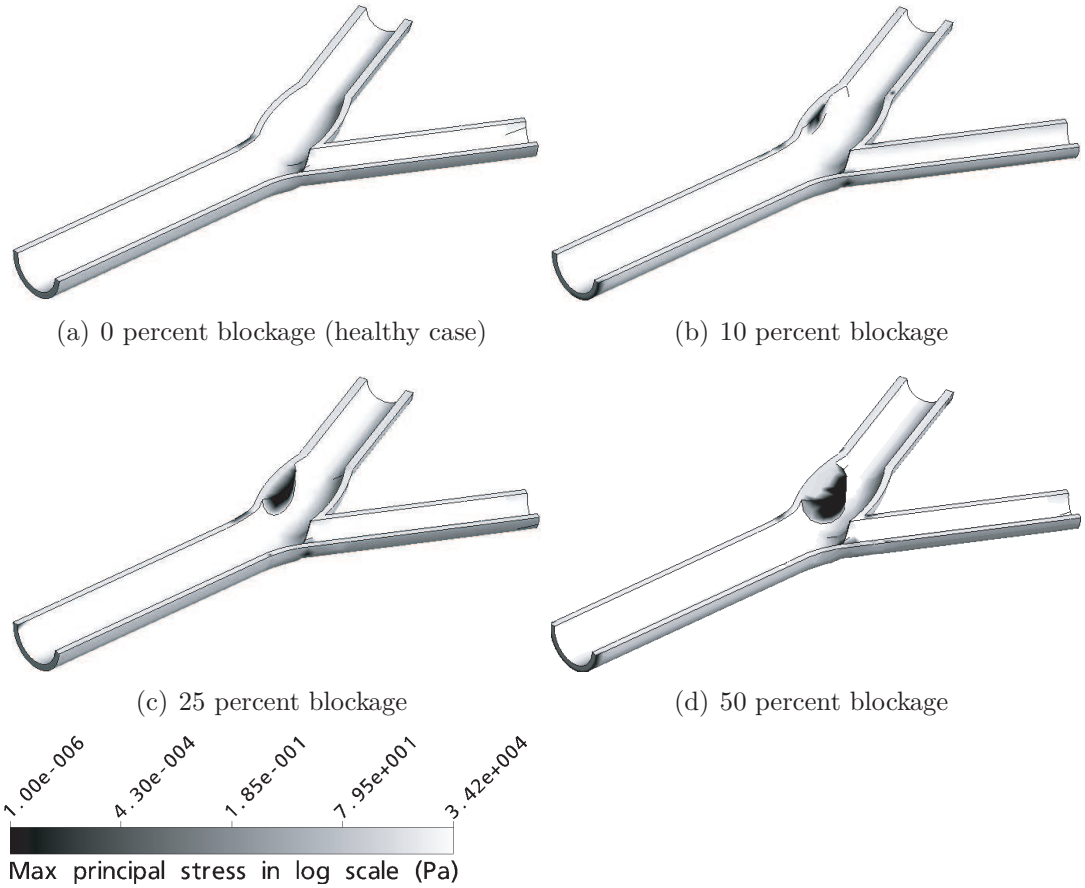

(a) 0 percent blockage (healthy case)

(b) 10 percent blockage

(c) 25 percent blockage

(d) 50 percent blockage

Figure 6.7: Identification of location of negative MPS (compression) in carotid bifurcation with different degrees of stenosis. Note that this plot is in logarithmic scale. The small value in this scale represents negative MPS.

Distribution of MPS We describe the distribution of MPS on the plaque. Figure 6.8 and 6.9 show the location of the stenosis inside the sinus of the carotid bifurcation and also the reference line (in Figure 6.8) on which the distribution of the MPS is plotted in Figure 6.9 and 6.11. From Figure 6.9, the region of high positive value of MPS can be observed along the border line of the stenosis while the region of negative value of MPS resides near the apex of the stenosis.

For the 10 percent blockage case, the pattern of MPS is highly symmetrical. However, as we increase the degree of stenosis, the distribution starts to become asymmetrical. For 25 and 50 percent blockage, it is noticeable that MPS at the proximal ends of the stenosis is greater than that at the distal end (Figure 6.9). Not only does the pattern become asymmetrical when increasing the degree of stenosis, the minimum value of MPS becomes more negative. At peak flow rate, it drops from about -400 to -4000 Pa when changing the degree of stenosis from 10 to 25 percent. The value was observed at both peak and minimum flow rate, which show a similar trend. The only difference is that at the minimum flow rate, the order of magnitude is much smaller. It is shown that the minimum MPS takes place at the apex of the stenosis. In addition, the profile of distribution of the MPS on the stenosis appears to be of smaller variation as we increase the degree of stenosis.

Wall shear stress

Wall shear stress (WSS) is of low and high value near the outer and inner wall respectively. According to Figure 6.10, there is a similar pattern for these cases. High WSS can be found near the flow divider of the bifurcation and the distal end of the inner wall of the sinus. These regions have very high velocity and shear strain rate. Therefore, high WSS is experienced in these regions. Another region worth considering is the apex of the stenosis. Despite the overall low shear strain rate and velocity on the outer wall of the sinus, the maximum value of WSS is always on the apex of the stenosis. At the distal and proximal end of the stenosis, extremely small values of WSS are shown in Figure 6.10. Moreover, the WSS pattern on the stenosis becomes increasingly asymmetrical as the degree of stenosis increases. Distribution of WSS along a line on the stenosis is shown in Figure 6.11. For 10

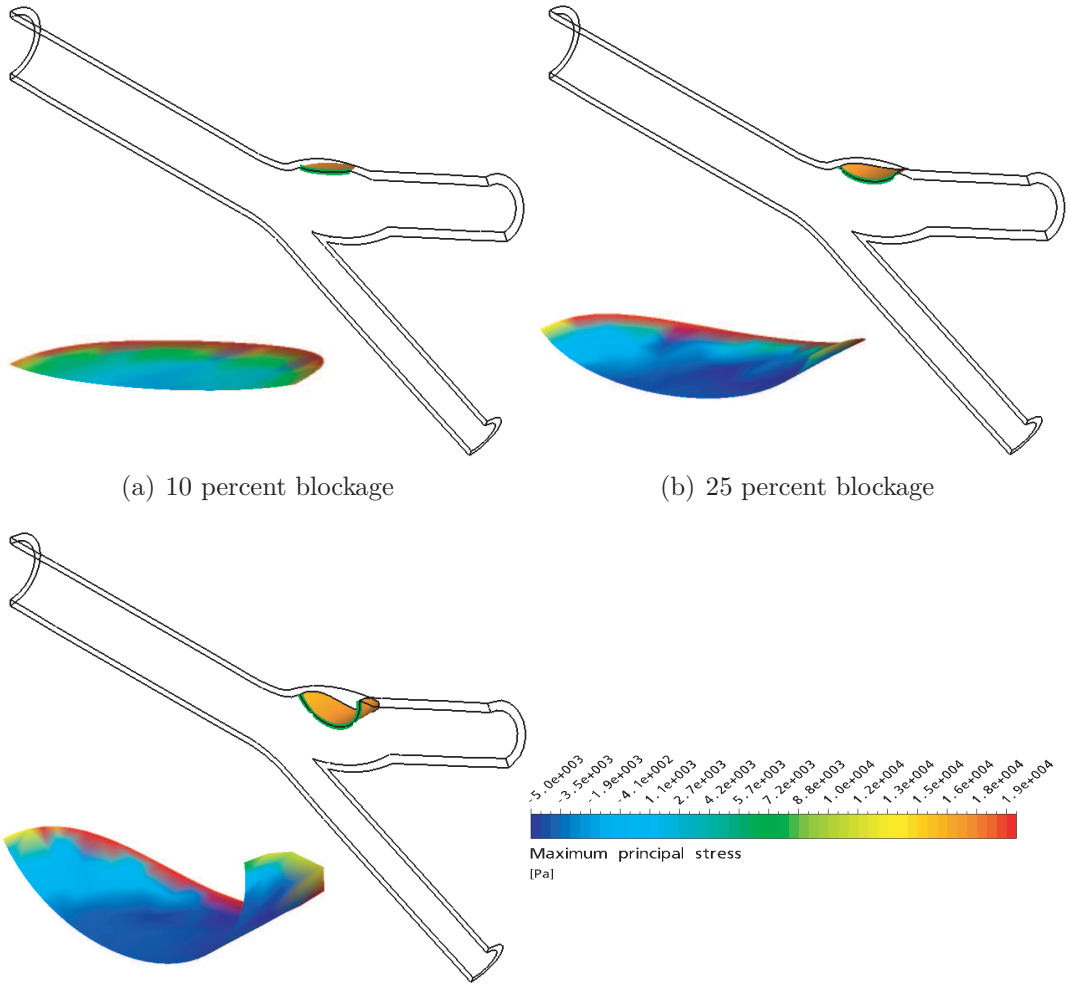

(a) 10 percent blockage

(b) 25 percent blockage

(c) 50 percent blockage

Figure 6.8: Contours of MPS distributions based on different degrees of stenosis.

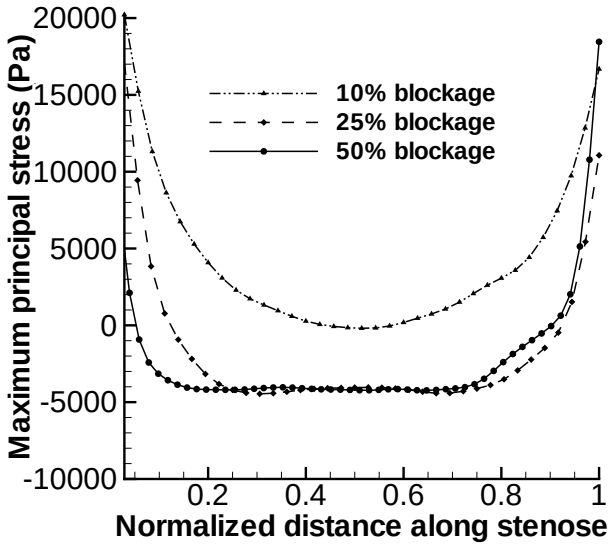

(a) Peak flow rate

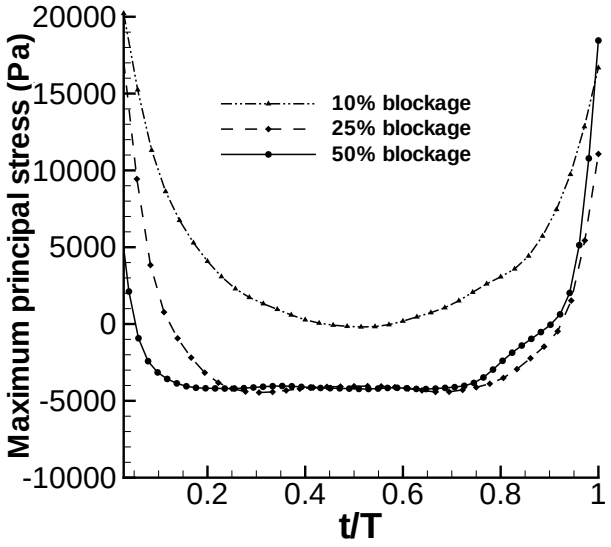

(b) Minimum flow rate

Figure 6.9: Plots of the MPS on stenosis in diseased carotid bifurcations.

and 25 percent blockage cases, the entire stenosis immerses in the recirculation zone. Therefore, WSS in these two cases has negative values. However, in the case of 50 percent blockage, negative WSS only appears at the proximal and distal ends of the stenosis, whilst the centre of the stenosis experiences positive WSS.

Relationship of pulse pressure, MD and minimum MPS

In relation to Figure 6.3(a) and 6.12(a), as the pressure is increased to reach the peak of approximately 4,000 Pa, both displacement and MPS increase. After the peak of the pressure pulse, displacement and MPS decline proportionally with respect to pressure. Regardless of the degree of stenosis, the MPS detected on the stenotic surface is negative throughout the entire heart cycle. However, the degree of stenosis has an influence on the magnitude of the MPS. That is, as we increase the percentage of blockage from 10 to 50 percent, the magnitude of the negative principal stress becomes larger however the shape of the plot of principal stress against time remains essentially the same.

Time variation of MD at stenosis is shown in Figure 6.12(b). Similar to the MPS, MD on the plaque also has a strong relationship with blood pressure. The MD rises with an increase in blood pressure during systole. After the peak, it declines to reach the minimum value at the end of diastole. It should be noted that the peak value of the MD decreases with the degree of stenosis. The peak of MD decreases from 0.28 mm to about 0.18 mm as the degree of stenosis is increased from 10 to 50 percent Time variation of MD in the region near the flow divider is shown in Figure 6.12(c). Similar to the MPS and displacement on the plaque, MD in this region also varies with blood pressure. The MD rises with an increase in blood pressure during systole. After the peak, it declines to reach the minimum value at the end of diastole. However, unlike MD at the stenosis, MD in this region is not affected by a variation of the degree of stenosis. Regardless of the percentage of blockage, the peak value of the MD is approximately 0.3 mm.

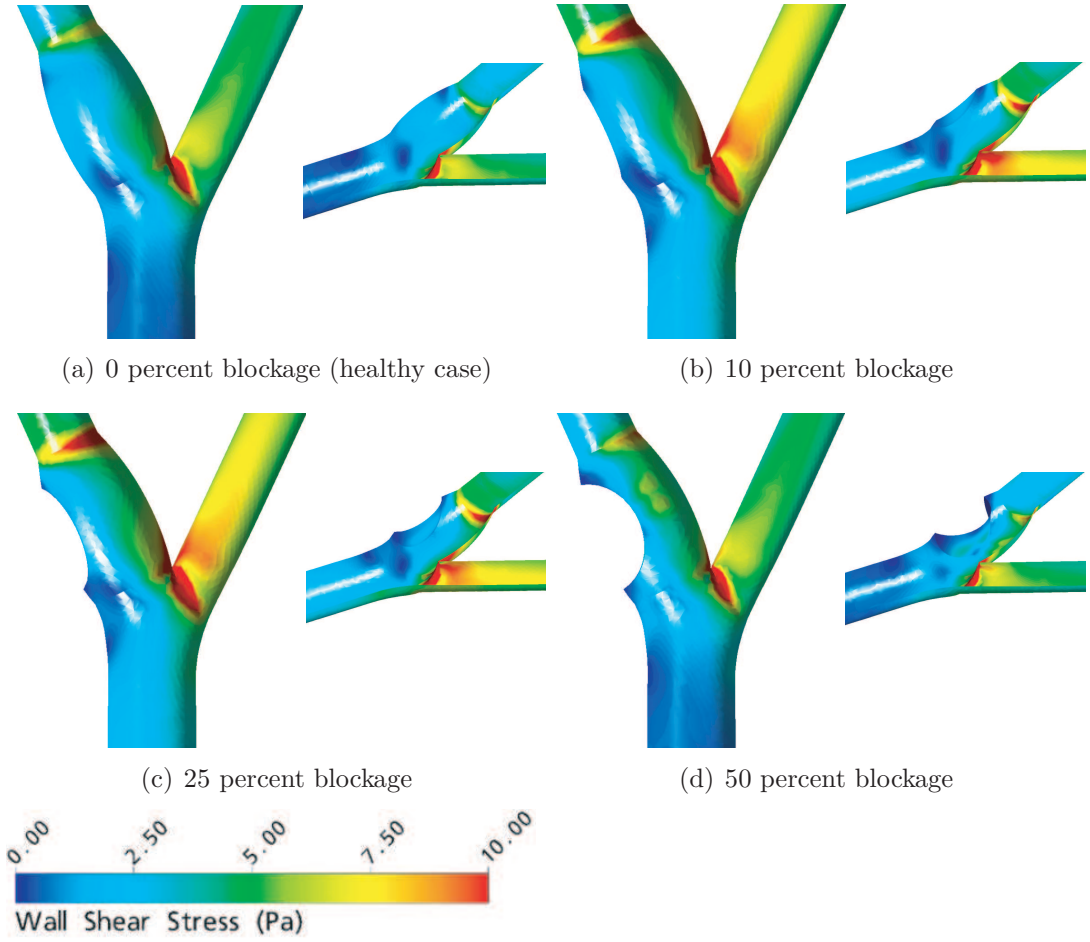

(a) 0 percent blockage (healthy case)

(b) 10 percent blockage

(c) 25 percent blockage

(d) 50 percent blockage

Figure 6.10: Pattern of wall shear stress in carotid bifurcation with different degrees of stenosis.

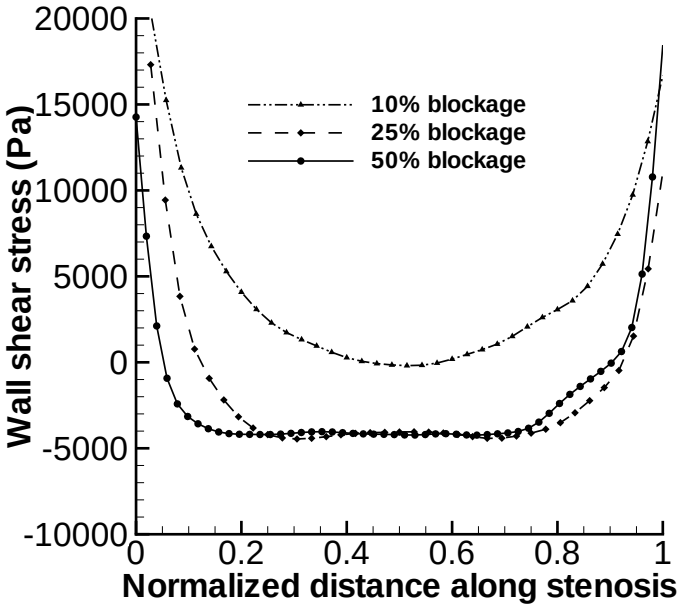

(a) Peak flow rate

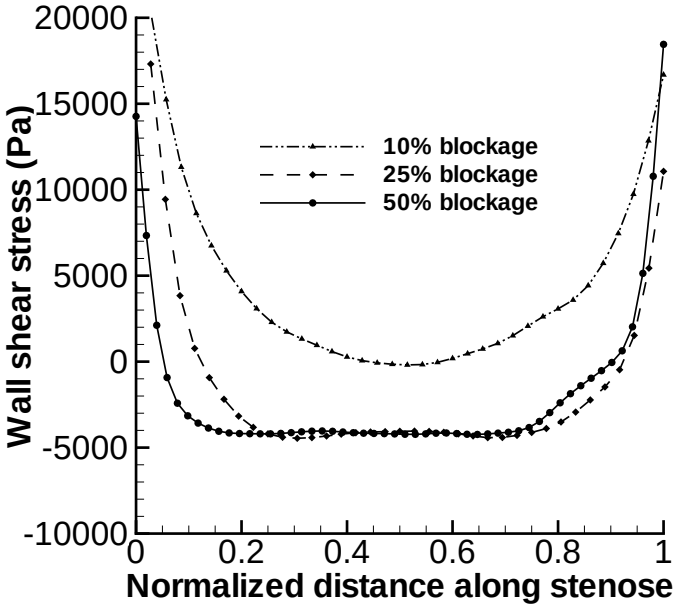

(b) Minimum flow rate

Figure 6.11: Plots of wall shear stress along the stenosis.

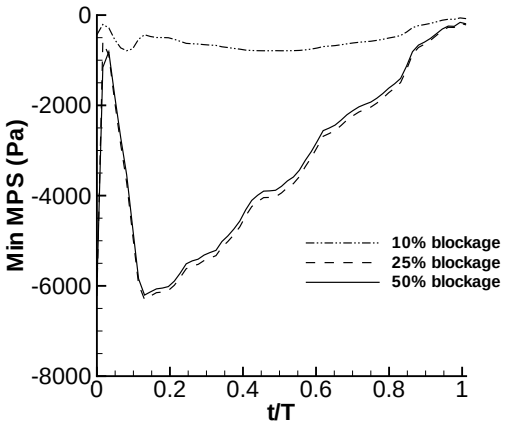

(a) MPS

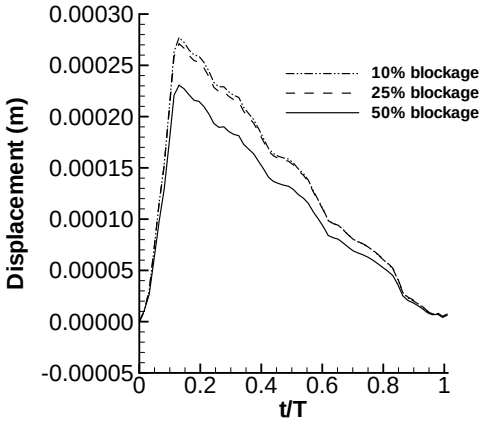

(b) MD on stenosis

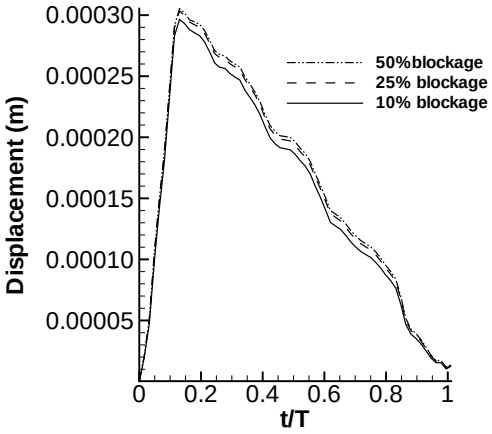

(c) MD in the region upstream to bifurcation point

Figure 6.12: Relationship of pulse pressure, MD and minimum value of MPS.

6.5 Discussion

6.5.1 Blood flow pattern and wall shear stress

Flow pattern of the healthy carotid bifurcation is predicted to have a single large recirculation zone located inside the ICA sinus near its outer wall. This recirculation zone is also recognized in studies by many investigators (Perktold et al. (1991), Ku and Giddens (1983) and Ding et al. (2001)) who worked with similar geometries. This recirculation zone is known to be the most common place for plaque to develop. As we increase the degree of stenosis, similar behaviour is observed for 10 and 25 percent blockage cases. Conversely, for 50 percent blockage, it appears that there are two separate recirculation zones instead of one. These are located at the proximal and distal end of the stenosis. Since they are much smaller than the single wake found in healthy and mildly stenotic cases, it may be reasonable to conclude that flow reversal is minimal in the case of severe stenosis. For 50 percent blockage cases, the stenotic apex blocks the backward flow and therefore divides the original recirculation zone into two zones. This has significant implication on plaque growth. Based on the hypothesis that plaque development is localized in the region of low wall shear stress, this would mean that plaque will grow either toward CCA or the outlet of the ICA. This fits the past findings by Samuel et al. (2008) that the plaque region is sometimes found around the terminal end of CCA and also further downstream of the ICA. The stenosis is exposed to high velocity, shear strain rate and high wall shear stress. The low and oscillating wall shear stress hypothesis suggests that the plaque will cease to grow. However, this is not always the case as statistically shown by Grant et al. (2003) that the stenosis can vary from mild to extremely severe (>80 percent of blockage area).

6.5.2 Deformation

In our healthy carotid bifurcation, MD is located just upstream of the bifurcation point. Another place of considerable deformation during each cardiac cycle is the region distal of the CCA to the distal end of the sinus. Tada and Tarbell (2005)

and Ramnarine et al. (2003) have confirmed this phenomenon both qualitatively and quantitatively. Ramnarine et al. (2003) uses Tissue Doppler Imaging technique to obtain deformation of the carotid wall. Although their flow condition is slightly different from ours, the results ensure that our pattern of deformation corresponds closely with experimental data. This deformation data can be used in analysis of plaque developement and rupture. In this work, it is discovered that the degree of stenosis does not affect distribution of the deformation. Nevertheless, it has influences on the magnitude of deformation of the plaque. The level of deformation seems to be inversely proportional to thickness. This is because thickening of the artery in the region provides more strength to the wall for withstanding the pressure. In contrast, the other region of high deformation (just upstream of the bifurcation point), which has constant thickness, is not changing with the degree of stenosis. Further support of this is shown by Valencia (2006) who presents a contour showing that the deformation at the stenosis is much smaller than that upstream of the bifurcation point. However, the influence of the degree of stenosis on the deformation is not presented.

6.5.3 Principal stress

In a healthy carotid bifurcation, MPS is positive throughout the artery. Regions of high MPS are found to be at the bifurcation point and also on the outer wall of ICA sinus. This result is similar to numerous previous works (e.g. Salzar et al., 1995; Hariton et al., 2007; Callaghan et al., 2009; Delfino et al., 1997) which also have information about mechanical stress on a similar geometry. We note that this idealized healthy carotid bifurcation is only undergoing tension. In contrast, both tension and compression can be clearly observed in a diseased carotid bifurcation. The only region which experiences compression is on the surface of the stenosis. In the past, regions of compression in diseased carotid bifurcation are also reported in many studies such as that by Samuel et al. (2007) and Lee and Xu (2002). However, most of them studied only the stenosis with lipid core. Samuel et al. (2007) found the region of compression to always be next to the region of high

tensile stress. On the other hand, Lee and Xu (2002), who also work on non-atheromatous plaque, presented a contour of mechanical stress which shows that the stenotic apex is under compression whilst other parts including the proximal and distal ends of the artery are under tension. This agrees well with our results as shown in Figure 6.7. It is clear that tensile stress appears along the border of the stenosis with compression in the middle. Our findings may have an impact on the research direction of endothelial cell behaviour due to mechanical stress since in the past only plaque undergoing hypertension was studied by Kaunas et al. (2006) and Kaunas and Hsu (2009). Kaunas et al. (2006) suggests that arterial wall can orientate stress fibre in the direction of tension force applied, and if tension is applied in many directions (i.e. in the region where there is oscillating shear force), the stress fibre can be randomly oriented and result in atherosclerosis. Our results suggest the need for future research which aims to investigate the behavior of the endothelial cell when it is under compression. We speculate that the compression of the arterial wall may have some implications as evidenced by Abdelaziz et al. (1999). In his work, he suggested that atherosclerosis may be induced by compression as a result of the hyoid bone. We notice that atherosclerosis can also be caused due to compression as shown in both his and our works.

6.5.4 Relationship of pulse pressure, MD and minimum value of MPS

In our results, it appears that the magnitude of the MPS and MD will be maximum at peak pressure. This is firmly supported by Zhao et al. (2002), although they only provide information on the principal stress. Figure 6.12(a) to 6.12(c) show a clear relationship among these variables that both the magnitude of MD and MPS have positive correlation with blood pressure. This has a significant interpretation because the blood pressure can be a possible candidate of plaque growth and rupture based on stenotic stress on the stenotic region. The possibility of blood pressure being a cause of the plaque development and rupture is already well known. Giannoglou

et al. (2008) speculates that the elevated heart rate that leads to an increase in exposure time of high blood pressure, and can well be an indicator of atherosclerotic risk. In our work, it is revealed that the plaque undergoes extremely high and low compression during systole and diastole. Therefore, an elevated heart rate can place the artery in a condition whereby it has to withstand the high compressive force for long periods of time.

6.6 Summary and concluding remarks

We summarize that different degrees of stenosis have a significant influence on three basic characteristics of atherosclerosis. Firstly, the presence of severe stenosis can dramatically alter the blood flow pattern. Flow reversal is found to be smaller at advanced stages of the disease. This leads to diminishing low WSS in the stenotic region. Secondly, the apex of stenosis experiences compressive stress which can intensify as it grows. This explains why plaque can still grow at advanced stages when the wall shear stress is higher. Finally, the relationship among pulse pressure, MD and MPS suggests that elevated heart rate can lead to a higher risk of stroke due to longer exposure to high MD and MPS. However, determining a proper range of suitable heart rate is beyond the scope of this current work.

Chapter 7

Concluding Remarks

7.1 Achievements and their significances

The achievements made in this work are summarized as follows.

7.1.1 Numerical and theoretical analysis on influence of structural time integration schemes on added mass instability in FSI

We have shown that stability condition of FSI calculation can be influenced significantly and allows a higher relaxation factor to be used. This means that computational cost can be greatly reduced by selecting a proper structural time integration scheme. However, the performance depends largely on the following factors:

- Applied numerical damping;
- Density ratio;
- Time step size;
- Geometrical properties such as radius and thickness of vessel.

The critical relaxation factor is higher when using the structural time integration scheme that does not contain any numerical damping ($\gamma = 0$). On the other hand, the choice of time integration schemes for discretizing fluid acceleration also has a strong impact on the stability condition. Our results suggest that more accurate schemes such as the second order accurate backward Euler leads to a more difficult condition for stability of FSI. Another important parameter is time step size used for computation. In particular, smaller time step size results in a more restrictive condition. However, as the time step size approaches zero, the value of the critical relaxation factor converges to a specific value. Another factor worth considering is the density ratio. It is found that this value has a considerable impact on FSI performance. In particular, the stability condition becomes invariant with the choice of structural time integration schemes in cases of high density ratio, while in the cases of low density ratio, this value depends largely on the schemes used. Finally, the condition is more restrictive when radius of the flexible vessel is greater due to an increase in maximum eigenvalue of the added mass operator. Moreover, the developement of artificial compressibility can be used to further improve FSI performance. It is found that this method can handle added mass instability efficiently and its performance does not depend on the following critical parameters listed above.

7.1.2 Performance comparision between under-relaxation technique and artificial compressibility

The performance of FSI using under-relaxation technique is compared to that using artificial compressibility by considering the amount of computational time required at various density ratio. Although, at low density ratio, the performance of under-relaxation technique appears to be slightly better than that of artificial compressibility, it is found that artificial compressibility is more efficient when density ratio is high. Therefore, it is concluded that artificial compressibility is a more applicable tools for dealing with a wide range of engineering applications whereby high density ratio is an unavoidable property.

7.1.3 Application of artificial compressibility to artherosclerosis in carotid bifurcation

Apart from being used as a demonstration of practicality of artificial compressibility for solving high density ratio problems, the analysis of artherosclerosis in carotid bifurcation using FSI also provides considerable input to this research field. The analysis serves the biomedical engineering research community in many aspects. The contributions from analysing this application can be summarized below.

- An insight on the influence of the degree of stenosis on mechanical stress experienced in carotid bifurcation. This provides an alternative explanation of how the stenotic plaque grows at the advanced stage of the disease. From the results in Chapter 6, the high level of mechanical stress is observed and can be the reason behind the growth of stenosis when the low and oscillating wall shear stress region disappears.

- An understanding of how blood flow pattern changes with the presence of stenosis with different sizes. It gives useful information about flow pattern inside carotid bifurcation at different degree of stenosis. Flow behavior dramatically changes as we increase the degree of blockage. This can be used as a future reference for other investigators in this field of biomedical engineering.

- A relationship between blood pressure, structural stress and deformation of the stenotic plaque. It establishes a firm relationship between flow pressure and mechanical stress which can be useful for determining a proper range of blood pressure in patients.

7.2 Future Work

In this work, only the generalized-α structural time integration schemes are used for the stability analysis. In the future, it may be useful to conduct a

similar study with other advanced time integration schemes such as Runge-Kutta schemes. Further analysis with other advanced schemes will provide more complete information of how the instability behaves. Moreover, it will provide guidelines to a wider range of researchers for conducting FSI problems of their interest because FSI codes use different schemes.

Artificial compressibility can be utilized efficiently for various engineering applications, and especially those involving internal incompressible flows. However, this method may not be applicable to problems in the following categories:

- External flow;
- Compressible flow.

These are potential areas which need improvements. For example, in compressible flow, the artificial compressiblity term, which is introduced to the fluid solver, may take a large number of coupling steps in order to vanish and not affect the real flow solution.

Appendix A

Detail derivation

A.1 Discretization of structural acceleration

In this section, the detail derivation of discretized structural acceleration is presented.

A.1.1 When minimum numerical damping is applied

Amplitude decay factor is set to 0 when maximum numerical damping is applied which yields $\alpha_m = 0$, $\alpha_f = 0$, $\alpha = \frac{1}{4}$ and $\delta = \frac{1}{2}$. Therefore, we get

$$\dot{d}^{n+1} = \dot{d}^n + \frac{1}{2}\ddot{d}^n \triangle t + \frac{1}{2}\ddot{d}^{n+1} \triangle t, \tag{A.1}$$

$$\ddot{d}^{n+1} = \frac{4}{\triangle t^2}\left[d^{n+1} - d^n - \triangle t \dot{d}^n - \frac{\triangle t^2}{4}\ddot{n}\right], \tag{A.2}$$

therefore,

$$\dot{d}^n = \dot{d}^{n-1} + \frac{1}{2}\ddot{d}^{n-1}\triangle t + \frac{1}{2}\ddot{d}^{n}\triangle t, \tag{A.3}$$

$$\dot{d}^{n-1} = \dot{d}^{n-2} + \frac{1}{2}\ddot{d}^{n-2}\triangle t + \frac{1}{2}\ddot{d}^{n-1}\triangle t, \tag{A.4}$$

$$\dot{d}^{n-2} = \dot{d}^{n-3} + \frac{1}{2}\ddot{d}^{n-3}\triangle t + \frac{1}{2}\ddot{d}^{n-2}\triangle t, \tag{A.5}$$

and,

$$\begin{aligned}
\ddot{d}^n &= \frac{4}{\triangle t^2}\left[d^n - d^{n-1} - \triangle t\dot{d}^{n-1} - \frac{\triangle t^2}{4}\ddot{d}^{n-1}\right] \\
&= \frac{4}{\triangle t^2}d^n - \frac{4}{\triangle t^2}d^{n-1} - \frac{4}{\triangle t}\dot{d}^{n-1} - \ddot{d}^{n-1} \\
\ddot{d}^{n-1} &= \frac{4}{\triangle t^2}\left[d^{n-1} - d^{n-2} - \triangle t\dot{d}^{n-2} - \frac{\triangle t^2}{4}\ddot{d}^{n-2}\right], \\
&= \frac{4}{\triangle t^2}d^{n-1} - \frac{4}{\triangle t^2}d^{n-2} - \frac{4}{\triangle t}\dot{d}^{n-2} - \ddot{d}^{n-2} \\
\ddot{d}^{n-2} &= \frac{4}{\triangle t^2}\left[d^{n-2} - d^{n-3} - \triangle t\dot{d}^{n-3} - \frac{\triangle t^2}{4}\ddot{d}^{n-3}\right] \\
&= \frac{4}{\triangle t^2}d^{n-2} - \frac{4}{\triangle t^2}d^{n-3} - \frac{4}{\triangle t}\dot{d}^{n-3} - \ddot{d}^{n-3}
\end{aligned} \tag{A.6}$$

$$
\begin{aligned}
\ddot{d}^{n+1,\alpha} &= \ddot{d}^{n+1} \\
&= \frac{4}{\triangle t^2}\left[d^{n+1} - d^n - \triangle t\dot{d}^n + \frac{\triangle t^2}{4}\ddot{n}\right] \\
&= \frac{1}{\triangle t^2}[4d^{n+1} - 4d^n] - \frac{4}{\triangle t}\dot{d}^{n-1} - 2\ddot{d}^{n-1} - 3\ddot{d}^n \\
&= \frac{1}{\triangle t^2}[4d^{n+1} - 4d^n] - \frac{4}{\triangle t}\dot{d}^{n-1} - 2\ddot{d}^{n-1} - \frac{12}{\triangle t^2}d^n \\
&+\frac{12}{\triangle t^2}d^{n-1} + \frac{12}{\triangle t}\dot{d}^{n-1} + 3\ddot{d}^{n-1} \\
&= \frac{1}{\triangle t^2}[4d^{n+1} - 4d^n] - \frac{4}{\triangle t}\dot{d}^{n-1} - 2\ddot{d}^{n-1} \\
&-\frac{12}{\triangle t^2}d^n + \frac{12}{\triangle t^2}d^{n-1} + \frac{12}{\triangle t}\dot{d}^{n-1} + 3\ddot{d}^{n-1} \\
&= \frac{1}{\triangle t^2}[4d^{n+1} - 16d^n + 12d^{n-1}] + \frac{8}{\triangle t}\dot{d}^{n-1} + \ddot{d}^{n-1} \\
&= \frac{1}{\triangle t^2}[4d^{n+1} - 16d^n + 12d^{n-1}] + \frac{8}{\triangle t}\dot{d}^{n-2} + 4\dot{d}^{n-2} + 4\ddot{d}^{n-1} + \ddot{d}^{n-1} \\
&= \frac{1}{\triangle t^2}[4d^{n+1} - 16d^n + 12d^{n-1}] + \frac{8}{\triangle t}\dot{d}^{n-2} + \frac{4}{\triangle t}\dot{d}^{n-2} + 5\ddot{d}^{n-1} \\
&= \frac{1}{\triangle t^2}[4d^{n+1} - 16d^n + 12d^{n-1}] + \frac{8}{\triangle t}\dot{d}^{n-2} + \frac{4}{\triangle t}\dot{d}^{n-2} + 5\ddot{d}^{n-1} \\
&= \frac{1}{\triangle t^2}[4d^{n+1} - 16d^n + 12d^{n-1}] + \frac{8}{\triangle t}\dot{d}^{n-2} + \frac{4}{\triangle t}\dot{d}^{n-2} + \frac{20}{\triangle t^2}d^{n-1} \\
&-\frac{20}{\triangle t^2}d^{n-2} - \frac{20}{\triangle t}\dot{d}^{n-2} - 5\ddot{d}^{n-2} \\
&= \frac{1}{\triangle t^2}[4d^{n+1} - 16d^n + 32d^{n-1} - 20d^{n-2}] - \frac{12}{\triangle t}\dot{d}^{n-2} - \ddot{d}^{n-2} \\
&= \frac{1}{\triangle t^2}[4d^{n+1} - 16d^n + 32d^{n-1} - 20d^{n-2}] - \frac{12}{\triangle t}\dot{d}^{n-3} - 6\ddot{d}^{n-3} - 7\ddot{d}^{n-2} \\
&= \frac{1}{\triangle t^2}[4d^{n+1} - 16d^n + 32d^{n-1} - 20d^{n-2}] - \frac{12}{\triangle t}\dot{d}^{n-3} - 6\ddot{d}^{n-3} \\
&-\frac{28}{\triangle t^2}d^{n-2} + \frac{28}{\triangle t^2}d^{n-3} + \frac{28}{\triangle t}\dot{d}^{n-3} + 7\ddot{d}^{n-3} \\
&= \frac{1}{\triangle t^2}[4d^{n+1} - 16d^n + 32d^{n-1} - 48d^{n-2} + 28d^{n-3}] \\
&-\frac{16}{\triangle t}\dot{d}^{n-3} + \ddot{d}^{n-3}. \qquad \text{(A.7)}
\end{aligned}
$$

A.1.2 When maximum numerical damping is applied

Amplitude decay factor is set to 1 when maximum numerical damping is applied which yields $\alpha_m = -1$, $\alpha_f = 0$, $\alpha = 1$ and $\delta = \frac{3}{2}$. Therefore, we get

$$\dot{d}^{n+1} = \dot{d}^n - \frac{1}{2}\ddot{d}^n \triangle t + \frac{3}{2}\ddot{d}^{n+1}\triangle t, \tag{A.8}$$

$$\ddot{d}^{n+1} = \frac{1}{\triangle t^2}\left[d^{n+1} - d^n - \triangle t\dot{d}^n + \frac{\triangle t^2}{2}\ddot{n}\right], \tag{A.9}$$

therefore,

$$\dot{d}^n = \dot{d}^{n-1} - \frac{1}{2}\ddot{d}^{n-1}\triangle t + \frac{3}{2}\ddot{d}^n\triangle t, \tag{A.10}$$

$$\dot{d}^{n-1} = \dot{d}^{n-2} - \frac{1}{2}\ddot{d}^{n-2}\triangle t + \frac{3}{2}\ddot{d}^{n-1}\triangle t, \tag{A.11}$$

$$\dot{d}^{n-2} = \dot{d}^{n-3} - \frac{1}{2}\ddot{d}^{n-3}\triangle t + \frac{3}{2}\ddot{d}^{n-2}\triangle t, \tag{A.12}$$

and,

$$\ddot{d}^n = \frac{1}{\triangle t^2}\left[d^n - d^{n-1} - \triangle t\dot{d}^{n-1} + \frac{\triangle t^2}{2}\ddot{d}^{n-1}\right], \tag{A.13}$$

$$\ddot{d}^{n-1} = \frac{1}{\triangle t^2}\left[d^{n-1} - d^{n-2} - \triangle t\dot{d}^{n-2} + \frac{\triangle t^2}{2}\ddot{d}^{n-2}\right], \tag{A.14}$$

$$\ddot{d}^{n-2} = \frac{1}{\triangle t^2}\left[d^{n-2} - d^{n-3} - \triangle t\dot{d}^{n-3} + \frac{\triangle t^2}{2}\ddot{d}^{n-3}\right] \tag{A.15}$$

$$
\begin{aligned}
\ddot{d}^{n+1,\alpha} &= 2\ddot{d}^{n+1} - \ddot{d}^{n} \\
&= \frac{2}{\triangle t^2}\left[d^{n+1} - d^{n} - \triangle t\dot{d}^{n} + \frac{\triangle t^2}{2}\ddot{n}\right] - \dot{d}^{n} \\
&= \frac{2}{\triangle t^2}d^{n+1} - \frac{2}{\triangle t^2}d^{n} - \frac{2}{\triangle t}d^{n+1} \\
&= \frac{2}{\triangle t^2}d^{n+1} - \frac{2}{\triangle t^2}d^{n} - \frac{2}{\triangle t}\dot{d}^{n-1} + \ddot{d}^{n-1} - 3\ddot{d}^{n} \\
&= \frac{2}{\triangle t^2}d^{n+1} - \frac{2}{\triangle t^2}d^{n} - \frac{2}{\triangle t}\dot{d}^{n-1} - \frac{1}{\triangle t}[d^{n-1} - d^{n-2} - \triangle t\dot{d}^{n-2} \\
&+ \frac{\triangle t^2}{2}\ddot{d}^{n-2} - 3d^{n} + 3d^{n-1} + 3\dot{d}^{n-1} - 3\frac{\triangle t^2}{2}\ddot{d}^{n-1}] \\
&= \frac{1}{\triangle t^2}[2d^{n+1} - \frac{5}{\triangle t^2}d^{n} - \frac{4}{\triangle t}d^{n-1} + \frac{2}{\triangle t}d^{n-2}] - \frac{2}{\triangle t}\dot{d}^{n-1} \\
&- \frac{1}{\triangle t}((\dot{d}^{n-2} - \frac{\triangle t}{2}\ddot{d}^{n-2} + \frac{3\triangle t}{2}\ddot{d}^{n-1}) - 3\dot{d}^{n-1}) \\
&= \frac{1}{\triangle t^2}[2d^{n+1} - \frac{5}{\triangle t^2}d^{n} - \frac{4}{\triangle t}d^{n-1} + \frac{2}{\triangle t}d^{n-2}] - \frac{2}{\triangle t}\dot{d}^{n-1} \\
&- \frac{1}{\triangle t}(\dot{d}^{n-1} - 3\dot{d}^{n-1}) \\
&= \frac{1}{\triangle t^2}[2d^{n+1} - \frac{5}{\triangle t^2}d^{n} - \frac{4}{\triangle t}d^{n-1} + \frac{2}{\triangle t}d^{n-2}] \qquad \text{(A.16)}
\end{aligned}
$$

A.2 Discretization of fluid acceleration

In this section, the detail derivation of discretized fluid acceleration is presented. The zero order accurate structural predictor is used.

$$d_{\Gamma,P}^{n+1} = d_{\Gamma}^{n}. \qquad \text{(A.17)}$$

The calculation for fluid velocity at FSI interface can be written as

$$u_{\Gamma}^{n+1} = \frac{d_{\Gamma,P}^{n+1} - d_{\Gamma,P}^{n}}{\triangle t}. \qquad \text{(A.18)}$$

A.2.1 First order accurate backward Euler

$$\begin{aligned}\dot{u}_\Gamma^{n+1} &= \frac{u_{\Gamma,P}^{n+1} - u_{\Gamma,P}^{n}}{\triangle t} \\ &= \frac{1}{\triangle t^2}(d_\Gamma^n - d_\Gamma^{n-1} - d_\Gamma^{n-1} + d_\Gamma^{n-2}) \\ &= \frac{1}{\triangle t^2}(d_\Gamma^n - 2d_\Gamma^{n-1} + d_\Gamma^{n-2}). \end{aligned} \tag{A.19}$$

A.2.2 Second order accurate backward Euler

$$\begin{aligned}\dot{u}_\Gamma^{n+1} &= \frac{1}{\triangle t^2}[\frac{3}{2}u_\Gamma^{n+1} - 2u_\Gamma^n + \frac{1}{2}u_\Gamma^{n-1}] \\ &= \frac{1}{\triangle t}[\frac{3}{2}d_\Gamma^n - \frac{3}{2}d_\Gamma^{n-1} - 2d_\Gamma^{n-1} + 2d_\Gamma^{n-2} + \frac{1}{2}d_\Gamma^{n-2} - \frac{1}{2}d_\Gamma^{n-3}] \\ &= \frac{1}{\triangle t^2}[\frac{3}{2}d_\Gamma^n - \frac{7}{2}d_\Gamma^{n-1} + \frac{5}{2}d_\Gamma^{n-2} - \frac{1}{2}d_\Gamma^{n-3}]. \end{aligned} \tag{A.20}$$

A.2.3 Trapezoidal rule

$$\begin{aligned}\dot{u}_\Gamma^{n+1} &= \frac{2}{\triangle t}(u_\Gamma^{n+1} - u_\Gamma^n) + \dot{u}_\Gamma^{n-1} \\ &= \frac{2}{\triangle t^2}(d_\Gamma^n - d_\Gamma^{n-1} - d_\Gamma^{n-1} + d_\Gamma^{n-2}) + \dot{u}_\Gamma^{n-1} \\ &= \frac{2}{\triangle t^2}(d_\Gamma^n - 2d_\Gamma^{n-1} + d_\Gamma^{n-2}) + \dot{u}_\Gamma^{n-1}. \end{aligned} \tag{A.21}$$

Appendix B

Analysis on added mass instability

In the solution procedure of fluid-structure interaction (FSI), the so-call artificial added mass effect plays an important role in determining the stability of the computation. We propose a derivation using Von Neumann stability analysis, which shows its significance as a tool for studying this numerical instability. Our derivation demonstrates that FSI solution is severely unstable when density ratio is high, solid structure is thin and flexible. It also shows that this instability can be eliminated by introducing aritificial compressibility.

B.1 Analysis

In this section, the instability of fluid-structure interaction using partitioned approach is discussed. This section is divided into two sub-sections. The first one is the derivation of instability which occurs when using Leap-Frog and forward Euler schemes without artificial compressibility. The second one is the derivation of instability which occurs when using Leap-Frog and forward Euler schemes with artificial compressibility.

B.1.1 Leap-Frog and Euler scheme with under-relaxation

We refer to the governing equation of deformation of a flexible cylindrical tube in (Causin et al., 2005), which can be written as

$$\rho_s h_s \frac{\partial^2 d_\Gamma^s}{\partial t^2} + \rho_f M_a \frac{\partial^2 d_\Gamma^f}{\partial t^2} + a_0 d_\Gamma^s - b\frac{\partial^2 d_\Gamma^s}{\partial x^2} = P_{ext,\Gamma}, \tag{B.1}$$

where $a_0 = \frac{Eh_s}{r^2(1-\nu^2)}$ and $b = K_T B h_s$.

The Leap-Frog scheme for structural acceleration is written as

$$\ddot{d}_\Gamma^{n+1,s} = \frac{1}{\Delta t^2}(d_\Gamma^{n+1} - 2d_\Gamma^n + d_\Gamma^{n-1}). \tag{B.2}$$

The Euler scheme for FSI interface acceleration for fluid domain is written as

$$\ddot{d}_\Gamma^{n+1,f} = \tfrac{1}{\Delta t}(\dot{d}_\Gamma^n - \dot{d}_\Gamma^{n-1}) = \tfrac{1}{\Delta t^2}(d_\Gamma^n - 2d_\Gamma^{n-1} + d_\Gamma^{n-2}). \tag{B.3}$$

It is noted that superscript m represents pseudo time step or stagger iteration, while n represents physical time step. Also, x and t are space and time respectively.

Due to the nature of sequential approach, the information used for calculation of FSI interface acceleration for fluid domain is always one step behind solid. From (B.1), since we are interested in added-mass instability, where the mass term is dominated the stiffness term, we will neglect some non-linearity. Therefore, (B.1) is reduced to equation (B.4) such that

$$\rho_s h_s \frac{\partial^2 d_\Gamma^s}{\partial t^2} + \rho_f M_a \frac{\partial^2 d_\Gamma^f}{\partial t^2} + a_0 d_\Gamma^s = P_{ext,\Gamma}. \tag{B.4}$$

Discretization of (B.4) is achieved by substituting (B.2) and (B.3) to give

$$\frac{\rho_s h_s}{\triangle t^2}(d_\Gamma^{n+1} - 2d_\Gamma^n + d_\Gamma^{n-1}) + \frac{\rho_f M_a}{\triangle t^2}(d_\Gamma^n - 2d_\Gamma^{n-1} + d_\Gamma^{n-2}) + a_0 d_\Gamma^n = P_{ext,\Gamma}^n. \tag{B.5}$$

To simplify it, let's look at only one position on the interface. Notice that the added-mass operator M_A can be represented by the ith eigenvalues of M_A, μ_i. This make (B.5) reduced further to (B.6) as given by

$$\frac{\rho_s h_s}{\triangle t^2}(d_i^{n+1} - 2d_i^n + d_i^{n-1}) + \frac{\rho_f \mu_i}{\triangle t^2}(d_i^n - 2d_i^{n-1} + d_i^{n-2}) + a_0 d_i^n = P_{ext,i}^n. \quad \text{(B.6)}$$

Next we will use the idea of Von Neumann stability analysis to prove stability of the system of discrete equation (Strang, 2007). This technique based on understanding in fourier analysis that any function can be represented by a superposition of basis functions like sine, cosine and exponential functions. The idea is to represent the solution in terms of initial value $e^{iat}e^{ikx}$, which depends only on spatial variation x. In other words, we are trying to separate variables x and t in our solution. This will allow us to monitor how the solution is growing with time. Initial value of solution can be written as

$$d(x,t) \approx \int_{-\infty}^{\infty} e^{iat}e^{ikx}dk$$

or

$$d(x,t) \approx \sum_{-\infty}^{\infty} e^{iat}e^{ikx}. \quad \text{(B.7)}$$

Note that a is a temporal wave frequency, which is also a function of spatial wave frequency, k. For simplicity, we drop the summation sign in equation (B.7) since our aim is to prove the instability, which can be done by monitoring only one mode of the solution. Therefore (B.7) becomes

$$d(x,t) \approx e^{iat}e^{ikx}. \quad \text{(B.8)}$$

Now we have separated the time and space variation in our solution. From (B.8), the initial solution is in the form of multiplication of complex exponential terms and our initial value $e^{iat}e^{ikx}$. The next step is to represent the other terms (d_i^n, d_i^{n-1}) in term of the initial value of the system (d_i^{n-2}). This is set to be the initial value because in the discrete equation (B.6), d_i^{n-2} is the oldest information available.

Let $d_i^{n-2} \approx e^{iat}e^{ikx}$, which is our initial value. Therefore, displacement at time step $n-1$ and n can be represented as

$$d_i^{n-1} = e^{ia(t+\Delta t)}e^{ikx} \quad \text{and} \quad d_i^n = e^{ia(t+2\Delta t)}e^{ikx}.$$

By substituting (B.9) into (B.6), we get

$$\begin{aligned}\frac{\rho_s h_s}{\triangle t^2}(d_i^{n+1} - 2\,e^{ia(t+2\Delta t)}e^{ikx} + e^{ia(t+\Delta t)}e^{ikx}) + \frac{\rho_f \mu_i}{\triangle t^2}(e^{ia(t+2\Delta t)} \\ -2e^{ia(t+\Delta t)}e^{ikx} + e^{ikx}) + \, a_0\, e^{ia(t+2\Delta t)}e^{ikx} = P_{ext,i}^n. \qquad \text{(B.9)}\end{aligned}$$

The growth factor is determined by rearranging above equation as

$$\begin{aligned} d_i^{n+1} &= \left\{ \frac{\triangle t^2}{\rho_s h_s}\left[\frac{P_{ext,i}^n}{e^{iat}e^{ikx}} - a_0 e^{ia2\Delta t} - \frac{\rho_f \mu_i}{\triangle t^2}\left(e^{ia2\Delta t} - 2e^{ia\Delta t} + 1\right)\right] + 2e^{ia2\Delta t} - e^{ia\Delta t} \right\} e^{iat}e^{ikx} \\ &= \left\{ -\frac{\rho_f \mu_i}{\rho_s h_s}\left(e^{ia2\Delta t} - 2e^{ia\Delta t} + 1\right) + 2e^{ia2\Delta t} - e^{ia\Delta t} \right\} e^{iat}e^{ikx} \because \triangle t^2 \to 0 \\ &= \left\{ -\frac{\rho_f \mu_i}{\rho_s h_s}e^{ia2\Delta t} + 2\frac{\rho_f \mu_i}{\rho_s h_s}e^{ia\Delta t} - \frac{\rho_f \mu_i}{\rho_s h_s} + 2e^{ia2\Delta t} - e^{ia\Delta t} \right\} e^{iat}e^{ikx} \\ &= \underbrace{\left\{ \left[-\frac{\rho_f \mu_i}{\rho_s h_s} + 2\right] e^{ia2\Delta t} + \left[2\frac{\rho_f \mu_i}{\rho_s h_s} - 1\right] e^{ia\Delta t} - \frac{\rho_f \mu_i}{\rho_s h_s} \right\}}_{\text{Growth Factor}} \underbrace{e^{iat}e^{ikx}}_{\text{Initial value}} . \end{aligned} \qquad \text{(B.10)}$$

The solution is unstable if the absolute value of growth factor is greater than 1. Therefore, instability occurs if (B.11) that is given as

$$\left|\left[-\frac{\rho_f \mu_i}{\rho_s h_s}+2\right] e^{ia2\Delta t}+\left[2\frac{\rho_f \mu_i}{\rho_s h_s}-1\right] e^{ia\Delta t}-\frac{\rho_f \mu_i}{\rho_s h_s}\right| > 1 \tag{B.11}$$

is satisfied.

Although the growth factor we have here is an accumulated growth over three time step, it gives us enough information for determining if the solution of considered system is stable or not. This is because if growth factor after three time steps and the corresponding growth factor after one time step will still result in the same condition. A graphical representation of (B.11) can be plotted in a complex plane and compared with a unit circle in order to demonstrate the instability of the current scheme used for FSI as illustrated in Figures B.1. The origin of a circle related to this growth factor is shifted by $-\frac{\rho_f \mu_i}{\rho_s h_s}$ in the real axis of the complex plane. The radius is $\left|\left[-\frac{\rho_f \mu_i}{\rho_s h_s}+2\right]+\left[2\frac{\rho_f \mu_i}{\rho_s h_s}-1\right]\right|$, which equal to $\left|\frac{\rho_f \mu_i}{\rho_s h_s}+1\right|$.This is because $e^{ia\Delta t}$ and $e^{ia2\Delta t}$ are both equivalent to a unit circle.

It is clear that if $\frac{\rho_f \mu_i}{\rho_s h_s}$ is greater than or equivalent to zero, the FSI solution using Leap-Frog and Euler scheme becomes unstable. It can be concluded that the explicit scheme is unconditionally unstable. It is shown in Figures B.1 that physical properties of the engineering problem being solved are crucial to stability of the solution.

B.1.2 Leap-Frog and Euler scheme with artificial compressibility

According to (Degroote et al., 2009), artificial compressibility can be successfully used to enhance stability of the system. He claims that the artificial compressibility term introduced to the system helps stabilize the solution by

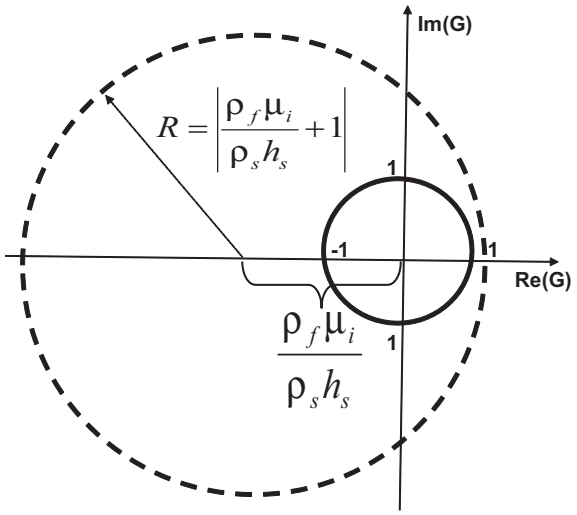

Figure B.1: $\frac{\rho_f \mu_i}{\rho_s h_s} > 0$, $R > 1$ (Unconditionally unstable)

mimic the information transferred across the interface as shown in (B.12) to (B.19).

The simplified fluid governing equation is written as

$$\frac{\partial V_m^{n+1}}{\partial t} + \int\limits_{\partial V^n} \left(\mathbf{v}_{m+1}^{n+1} - \mathbf{v}_c^n \right) dA \; = \; 0. \tag{B.12}$$

After introducing artificial compressibility, (B.12) becomes

$$\text{Artificial compressibility term} + \frac{\partial V_m}{\partial t} + \int\limits_{\partial V^n} \left(\mathbf{v}_{m+1}^{n+1} - \mathbf{v}_c^n \right) dA \; = \; 0, \tag{B.13}$$

$$\int \frac{1}{\rho c^2} \frac{p_{m+1}^{n+1} - p_m^{n+1}}{\Delta t} dV + \frac{\partial V_m^{n+1}}{\partial t} + \int\limits_{\partial V_m} \left(\mathbf{v}_{m+1}^{n+1} - \mathbf{v}_c^n \right) dA \; = \; 0. \tag{B.14}$$

According to (Degroote et al., 2009),

$$c^2 \; = \; \frac{p_b - p_a}{\Delta vol} \frac{vol}{\rho}. \tag{B.15}$$

By substituting (B.15) in (B.14), we get

$$\frac{\Delta vol}{p_b - p_a}\frac{p_{m+1}^{n+1} - p_m^{n+1}}{\Delta t} + \frac{\partial V_m^{n+1}}{\partial t} + \int\limits_{\partial V_m} \left(\mathbf{v}_{m+1}^{n+1} - \mathbf{v}_c^n\right) dA \;=\; 0. \tag{B.16}$$

To simplify,

$$\frac{\Delta vol}{p_b - p_a}\frac{p_{m+1}^{n+1} - p_m^{n+1}}{\Delta t} \approx \frac{\Delta vol}{\Delta t} \approx \frac{V_{m+1}^{n+1} - V_m^{n+1}}{\Delta t}. \tag{B.17}$$

$$\frac{\partial V_m}{\partial t} = \frac{V_m^{n+1} - V^n}{\Delta t}. \tag{B.18}$$

For validation of (B.16), we refer to (Degroote et al., 2009).

Substituting (B.17) and (B.18) in (B.16), we get

$$\frac{\partial V_{m+1}^{n+1}}{\partial t} + \int\limits_{\partial V^n} \left(\mathbf{v}^{n+1} - \mathbf{v}_c^n\right) dA \;=\; 0. \tag{B.19}$$

Therefore, It might be reason able to use $\ddot{d}_{m+1}^{n+1,f} = \frac{1}{\Delta t^2}(d_{m+1,i}^{n+1} - 2d_{m,i}^{n+1} + d_{m-1,i}^{n+1})$ instead of $\ddot{d}_{m+1}^{n+1,f} = \frac{1}{\Delta t^2}(d_{m,i}^{n+1} - 2d_{m-1,i}^{n+1} + d_{m-2,i}^{n+1})$.

By conducting a similar Von Neumann stability analysis that we have done for Leap-frog and Euler scheme, but this time with artificial compressibility, we obtain

$$\frac{\rho_s h_s}{\triangle t^2}(d_i^{n+1} - 2d_i^n + d_i^{n-1}) + \frac{\rho_f \mu_i}{\triangle t^2}(d_i^{n+1} - 2d_i^n + d_i^{n-1}) \;+\; a_0 d_i^n = P_{ext,i}^n \tag{B.20}$$

$$d_i^{n+1} - 2d_i^n + d_i^{n-1} = \frac{\triangle t^2 \left(P_{ext,i}^n - a_0 d_i^n\right)}{\rho_s h_s + \rho_f \mu_i} \tag{B.21}$$

$$d_i^{n+1} - 2d_i^n + d_i^{n-1} = 0 \cdot\!\cdot\!\cdot\; \triangle t^2 \to 0. \tag{B.22}$$

It can be further reduced to

$$d_i^{n+1} = 2d_i^n - d_i^{n-1}. \tag{B.23}$$

By recalling (B.9),

$$d_i^{n-1} = e^{ia(t+\triangle t)}e^{ikx} \text{ and } d_i^n = e^{ia(t+2\triangle t)}e^{ikx}.$$

Substituting into (B.23), we get

$$d_i^{n+1} = \left(2e^{ia2\triangle t} - e^{ia\triangle t=}\right)e^{iat}e^{ikx}, \tag{B.24}$$

and

$$|G| = \left|2e^{ia2\Delta t} - e^{ia\Delta t}\right|. \tag{B.25}$$

The growth factor in (B.25) is equivalent to a unit circle with origin at (0,0) in a complex plane. Therefore, it is determined that the solution is unconditionally stable when applying artificial compressibility.

B.2 Conclusion

In conclusion, explicit calculation of fluid-structure interaction leads to unconditional instability. On the contrary, previous studies have demonstrated that calculation in the implicit way can result in conditional stability. Our derivation also shows that properties of the problem such as density ratio and the flexibility of the solid structure can influence the stability significantly. Moreover, it is demonstrated that stability of the coupling can be maintained by applying "Artificial compressibility" technique. This numerical manipulation allows the solution to be done explicitly, which therefore reduces the computational time required to solve FSI problems.

References

Abdelaziz, O. S., Ogilvy, C. S. and Lev, M. (1999). Is there a potential role for hyoid bone compression in pathogenesis of carotid artery stenosis?, *Surgical Neurology* **51**(6): 650 – 653.

Alonso, J. J. and Jameson, A. (1994). Fully-implicit time-marching aeroelastic solutions, *AIAA Paper 91-0939* .

ANSYS Inc. 2009. ANSYS CFX-Solver Theory Guide (n.d.).

Badia, S., Quaini, A. and Quarteroni, A. (2008). Modular vs. non-modular preconditioners for fluid-structure systems with large added-mass effect, *Computer Methods in Applied Mechanics and Engineering* **197**(49-50): 4216 – 4232.

Bai, Y., Sun, D. and Lin, J. (2010). Three dimensional numerical simulations of long-span bridge aerodynamics, using block-iterative coupling and DES, *Computers & Fluids* **39**(9): 1549 – 1561.

Bathe, K. (1996). *Finite element procedures*, Prentice-Hall.

Batina, J. T. (1989). Unsteady Euler algorithm with unstructured dynamic mesh for complex-aircraft aeroelastic analysis, *AIAA* **89**: 1189.

Bendiksen, O. O. (1991). A new approach to computational aeroelasticity, *AIAA Paper 91-0939* .

Bletzinger, K. U., Gallinger, T., Kupzok, A. and Wuchner, R. (2006). Partitioned strategies for optimization in FSI, *European Conference on Computational Fluid Dynamics* .

Blom, F. J. (1998). A monolithical fluid-structure interaction algorithm applied to the piston problem, *Computer Methods in Applied Mechanics and Engineering* **167**(3-4): 369 – 391.

Boffi, D. and Gastaldi, L. (2004). Stability and geometric conservation laws for ALE formulations, *Computer Methods in Applied Mechanics and Engineering* **193**(42-44): 4717 – 4739.

Borazjani, I., Ge, L. and Sotiropoulos, F. (2008). Curvilinear immersed boundary method for simulating fluid structure interaction with complex 3D rigid bodies, *Journal of Computational Physics* **227**(16): 7587 – 7620.

Braun, A. L. and Awruch, A. M. (2009). Aerodynamic and aeroelastic analyses on the CAARC standard tall building model using numerical simulation, *Computers & Structures* **87**(9-10): 564 – 581.

Brezzi, F., Lions, J. L. and Pironneau, O. (2001). Analysis of a chimera method, *Comptes Rendus de IAcademie des Sciences. Serie I. Mathematique* **332**: 655–660.

C. Farhat, P. H. G. and Grandmont, C. (2001). The discrete geometric conservation law and the nonlinear stability of ALE schemes for the solution of flow problems on moving grids, *Journal of Computational Physics* **174**(2): 669–694.

Callaghan, F. M., Soellinger, M., Baumgartner, R. W., Boesiger, D. P. P. and Kurtcuoglu, V. (2009). The role of the carotid sinus in the reduction of arterial wall stresses due to head movements–potential implications for cervical artery dissection, *Journal of Biomechanics* **42**(6): 755–761.

Carlton, A. (2004). A summary study on arbitrary Lagrangian-Eulerian: methodology, implementation, and application, *Technical report*, Oregon State University.

Caro, C. G., Fitz-Gerald, J. M. and Schroter, R. C. (1971). Atheroma and arterial wall shear observation, correlation and proposal of a shear dependent mass transfer mechanism for atherogenesis., *Proceedings of The Royal Society of London.* **177**: 109–159.

Carter, F. D. and Baker, A. (1991). Accuracy and stability of a finite element pseudo compressibility CFD algorithm for incompressible thermal flows, *Numerical Heat Transfer* **20**: 1–23.

Causin, P., Gerbeau, J. F. and Nobile, F. (2005). Added-mass effect in the design of partitioned algorithms for fluid-structure problems, *Computer Methods in Applied Mechanics and Engineering* **194**(42-44): 4506 – 4527.

Cho, J. R., Lee, H. W., Sohn, J. S., Kim, G. J. and Woo, J. S. (2006). Numerical investigation of hydroplaning characteristics of three-dimensional patterned tire, *The European Journal of Mechanics A/Solids* **25**(6): 914 – 926.

Chorin, A. J. (1967). A numerical method for solving incompressible viscous flow problems, *Journal of Computational Physics* **2**: 12–26.

Chorin, A. J. (1968). Numerical solution of the Navier-Stokes equations, *Mathematics of Computation* **22**: 745–762.

Chung, J. and Hulbert, G. M. (1993). A time integration algorithm for structural dynamics with improved numerical dissipation: The generalized-α method., *Journal of Applied Mechanics* **60**(2): 371–375.

Daneshmand, F., Saketi, P. and Khajepour, A. (2005). 3D finite element analysis of a hydraulic engine mount including fluid-structure interaction, *in* Chakrabarti, SK and Hernandez, S and Brebbia, CA (ed.), *Fluid structure Interaction and Moving Boundary Problems*, Vol. 84 of *WIT TRANSACTIONS ON THE BUILT ENVIRONMENT*, Wessex Inst Technol; Univ La Coruna; WIT Transact Built Environm, WIT PRESS, ASHURST LODGE, SOUTHAMPTON SO40 7AA, ASHURST, ENGLAND, pp. 165–174. 3rd International Conference on Fluid Structure Interaction/8th International Conference on Computational Modelling and Experimental Measurements of Free and Moving Boundary Problems, Coruna, SPAIN, SEP 19-21, 2005.

Dang, H., Yang, Z. and Li, Y. (2010). Accelerated loosely-coupled CFD/CSD method for nonlinear static aeroelasticity analysis, *Aerospace Science and Technology* **14**(4): 250 – 258.

Degroote, J., Bathe, K. J. and Vierendeels, J. (2009). Simulation of fluid-structure interaction with the interface artificial compressibility method, *International Journal for Numerical Methods in Biomedical Engineering* **26**: 276–289.

Degroote, J., Bruggeman, P., Haelterman, R. and Vierendeels, J. (2008). Stability of a coupling technique for partitioned solvers in fsi applications, *Computers & Structures* **86**(23-24): 2224 – 2234.

Degroote, J., Haelterman, R., Annerel, S., Bruggeman, P. and Vierendeels, J. (2010). Performance of partitioned procedures in fluid-structure interaction, *Computers & Structures* **88**(7-8): 446 – 457.

Delfino, A., Stergiopulos, N., Moore, J. E. and Meister, J. J. (1997). Residual strain effects on the stress field in a thick wall finite element model of the human carotid bifurcation, *Journal of Biomechanics* **30**(8): 777–786.

Ding, Z., Wang, K., Li, J. and Cong, X. (2001). Flow field and oscillatory shear stress in a tuning-fork-shaped model of the average human carotid bifurcation, *Journal of Biomechanics* **34**(12): 1555–1562.

Donea, J., Huerta, A., Ponthot, J. P. and Rodriguez-Ferran, A. (2004). *Arbitrary Lagrangian-Eulerian methods In encyclopedia of computational mechanics Vol. 1: Fundamentals*, John Wiley & Sons.

Dowell, E. H. and Hall, K. C. (2001). Modelling of fluid-structure interaction, *Ann Rev Fluid Mech* **33**: 445–490.

Eloy, C., Souilliez, C. and Schouveiler, L. (2007). Flutter of a rectangular plate, *Journal of Fluids and Structures* **23**(6): 904 – 919.

Eriksson, L. E. (1982). Generation of boundary-conformation grids around wing-body configurations using transfinite interpolation, *AIAA* **20**: 1313–1320.

Falk, E. (1991). Coronary thrombosis: pathogenesis and clinical manifestations., *American Journal of Cardiology* **68**(7): 28–35.

Falk, E. (1992). Why do plaques rupture ?, *Monograph - American Heart Association* **86**: III.30–III.42.

Farhat, C. and Lesoinne, M. (2000). Two efficient staggered algorithms for the serial and parallel solution of three-dimensional nonlinear transient aeroelastic problems, *Computer Methods in Applied Mechanics and Engineering* **182**(3-4): 499 – 515.

Farhat, C., Lesoinne, M. and LeTallec, P. (1998). Load and motion transfer algorithms for fluid/structure interaction problems with non-matching discrete interfaces: Momentum and energy conservation, optimal discretization and application to aeroelasticity, *Computer Methods in Applied Mechanics and Engineering* **157**: 95–114.

Felippa, C. A. and Park, K. C. (1980). Staggered transient analysis procedures for coupled mechanical systems: Formulation, *Computer Methods in Applied Mechanics and Engineering* **24**(1): 61 – 111.

Felippa, C. A., Park, K. C. and Farhat, C. (2001). Partitioned analysis of coupled mechanical systems, *Computer Methods in Applied Mechanics and Engineering* **190**(24-25): 3247 – 3270.

Formaggia, L., Gerbeau, J. F., Nobile, F. and Quarteroni, A. (2001). Numerical treatment of defective boundary conditions for the navier-stokes equation, *INRIA Research Report No. 4093* .

Forster, C., Wall, W. A. and Ramm, E. (2007). Artificial added mass instabilities in sequential staggered coupling of nonlinear structures and incompressible viscous flows, *Computer Methods in Applied Mechanics and Engineering* **196**(7): 1278 – 1293.

Friedman, M. H., Deters, O. J., Bargeron, C. B. and Mark, G. M. H. F. F. (1986). Shear-dependent thickening of the human arterial intima, *Atherosclerosis* **60**: 161–171.

Friedman, M. H., Deters, O. J., Bargeron, C. B. and Mark, G. M. H. F. F. (1989). A biologically plausible model of thickening of arterial intima undershear, *Arteriosclerosis* **9**: 511–522.

Gerstenberger, A. and Wall, W. A. (2008). Enhancement of fixed-grid methods towards complex fluid-structure interaction applications, *International Journal for Numerical Methods in Fluids* **57**: 1227–1248.

Giannoglou, G. D., Chatzizisis, Y. S., Zamboulis, C., Parcharidis, G. E., Mikhailidis, D. P. and Louridas, G. E. (2008). Elevated heart rate and atherosclerosis: An overview of the pathogenetic mechanisms, *International Journal of Cardiology* **126**: 302 – 312.

Giddens, D. P., Zarin, C. K. and Glagov, S. (1993). The role of fluid mechanics in the localization and detection ofatherosclerosis., *Journal of Biomechanical Engineering* **115**(4B): 588–94.

Glagov, S., Zarins, C. K., Giddens, D. P. and Ku, D. N. (1989). *Mechanical factors in thepathogenesis, localization and evolution of atherosclerotic plaques*, Springer-Verlag, N.Y.

Glowinski, R., He, J. W., Lozinski, A., Rappaz, J. and Wagner, J. (2005). Finite element approximation of multi-scale elliptic problems using patches of elements, *Numerical Mathematics* .

Grant, E. G., Benson, C. B., Moneta, G. L., Alexandrov, A. V., Baker, J. D., Bluth, E. I., Carroll, B. A., Eliasziw, M., Gocke, J., Hertzberg, B. S., Katanick, S., Needleman, L., Pellerito, J., Polak, J. F., Rholl, K. S., Wooster, D. L. and Zierler, R. E. (2003). Carotid artery stenosis: Gray-scale and doppler US diagnosis - society of radiologists in ultrasound consensus conference 1, *Radiology* **229**(2): 340–346.

Gregory, A. F. and Michael, C. F. (2008). Arteriosclerosis: Rethinking the current classification, *Archives of Pathology and Laboratory Medicine* **133**(8): 1309–1316.

Grohmann, B. A., Dornberger, R. and Dinkler, D. (1997). Time-discontinuous stabilized space-time finite elements for aeroelasticity, *Fluid-Structure Interaction, Flow-Induced Vibrations and Noise* **3**: AD53–3.

Guidoboni, G., Glowinski, R., Cavallini, N. and Canic, S. (2009). Stable loosely-coupled-type algorithm for fluid-structure interaction in blood flow, *Journal of Computational Physics* **228**(18): 6916 – 6937.

Guillard, H. and Farhat, C. (2000). On the significance of the geometric conservation law for flow computations on moving meshes, *Comput. Methods Appl. Mech.Eng.* **190**(11-12): 1467–1482.

Hall, K. C., Thomas, J. P. and Dowell, E. H. (2000). Proper orthogonal decomposition technique for transonic unsteady aerodynamic flows, *AIAA* **38**(10): 1853–1862.

Hariton, I., deBotton, G., Gasser, T. C. and Holzapfel, G. A. (2007). Stress-modulated collagen fiber remodeling in a human carotid bifurcation, *Journal of Theoretical Biology* **248**(3): 460–470.

Hart, J. D., Baaijens, F. P. T., Peters, G. W. M. and Schreurs, P. J. G. (2003). A computational fluid-structure interaction analysis of a fiber-reinforced stentless aortic valve, *Journal of Biomechanics* **36**(5): 699 – 712. Cardiovascular Biomechanics.

Hartwich, P. M. and Agrawal, S. (1997). Method for perturbing multi-block patched grids in aeroelastic and design optimization applications, *AIAA* **97**: 2038.

Hatamura, Y. (1996). Zoku-Zoku Jissai-no Sekkei (Practical Design III), *Technical report*, The Nikkan Kogyo Shimbun, LTD.

Hieber, S. E. and Koumoutsakos, P. (2008). An immersed boundary method for smooth particle hydrodynamics of self-propelled swimmers, *Journal of Computational Physics* **227**: 8636–8654.

Hirt, C. W., Cook, J. L. and Butler, T. D. (1970). A Lagrangian method for calculating the dynamics of an incompressible fluid with free surface, *Journal of Computational Physics* **5**: 103–124.

Hron, J. and Turek, S. (2006). A monolithic FEM/multigrid solver for ALE formulation of fluid structure interaction with application in biomechanics, *Fluid-Structure Interaction: Modelling, Simulation, Optimisation* **53**: 146–170.

Hubner, B., Walhorn, E. and Dinkler, D. (2004). A monolithic approach to fluid-structure interaction using space-time finite elements, *Computer Methods in Applied Mechanics and Engineering* **193**(23-26): 2087 – 2104.

Irons, B. and Tuck, R. C. (1969). A version of the aitken accelerator for computer implementation, *International Journal for Numerical Methods in Engineering* **1**: 275–277.

Jacobson, M. (1999). *Fundamentals of atmospheric modeling*, Cambridge University Press.

Jaiman, R. J. (2007). *Accuracy and stability of transient multiphysics simulations*, PhD thesis, University of Illinois.

Jarvinen, E., Lyly, M., Ruokolainen, J. and Raback, P. (2001). Three dimensional fluid-structure interaction modeling of blood flow in elastic arteries, *Eccomas Computational Fluid Dynamics Conference* .

Joshi, A. K., Leask, R. L., Myers, J. G., Ojha, M. and Ethier, J. B. C. R. (2004). Intimal thickness is not associated with wall shear stress patterns in the human right coronary artery, *Arteriosclerosis, Thrombosis, and Vascular Biology* **24**(12): 2408–2413.

Kalro, V. and Tezduyar, T. E. (2000). A parallel 3D computational method for fluid-structure interactions in parachute systems, *Computer Methods in Applied Mechanics and Engineering* **190**(3-4): 321 – 332.

Kamakoti, R. and Shyy, W. (2004). Fluid-structure interaction for aeroelastic applications, *Progress in Aerospace Sciences* **40**(1): 535–558.

Kaunas, R. and Hsu, H. J. (2009). A kinematic model of stretch-induced stress fiber turnover and reorientation, *Journal of Theoretical Biology* **257**(2): 320–330.

Kaunas, R., Usami, S. and Chien, S. (2006). Regulation of stretch-induced JNK activation by stress fiber orientation, *Cellular Signalling* **18**(11): 1924–1931.

Kawahara, M. and Ohmiya, K. (1985). Finite element analysis of density flow using velocity correction method, *International Journal for Numerical Methods in Fluids* **5**: 981–993.

Kleinstreuer, C., Hyun, S., Buchanan, J. R., Longest, P. W., Archie, J. P. and Truskey, G. A. (2001). Hemodynamic parameters and early intimal thickening in branching blood vessels., *Critical Reviews in Biomedical Engineering* **29**(1): 1–64.

Knight, J. J., Lucey, A. D. and Shaw, C. T. (2010). Fluid-structure interaction of a two-dimensional membrane in a flow with a pressure gradient with application to convertible car roofs, *Journal of Wind Engineering and Industrial Aerodynamics* **98**(2): 65 – 72.

Koobus, B. and Farhat, C. (1999). Second-order accurate and geometrically conservative implicit schemes for flow computations on unstructured dynamic meshes, *Computer Methods in Applied Mechanics and Engineering* **170**(1-2): 103–129.

Korteweg, D. J. (1878). Uber die Fortpflanzungsgeschwindigkeit des Schalles in elastischen Rohren, *Annals of Physics* **5**: 525.

Ku, D. N. and Giddens, D. P. (1983). Pulsatile flow in a model carotid bifurcation, *Arteriosclerosis, Thrombosis, and Vascular Biology* **3**(1): 31–39.

Ku, D. N., Giddens, D. P., Zarins, C. K. and Glagov, S. (1985). Pulsatile flow and atherosclerosis in the human carotid bifurcation.positive correlation between plaque location and low oscillatingshear stress, *Arteriosclerosis, Thrombosis, and Vascular Biology* **5**(3): 293–302.

Kuttler, U. and Wall, W. (2008). Fixed-point fluid-structure interaction solvers with dynamic relaxation, *Computational Mechanics* **43**(1): 61–72.

l Farhat, C., van der Zee, K. G. and Geuzaine, P. (2006). Provably second-order time-accurate loosely-coupled solution algorithms for transient nonlinear computational aeroelasticity, *Computer Methods in Applied Mechanics and Engineering* **195**(17-18): 1973 – 2001. Fluid-Structure Interaction.

Lau, K. D., Diaz, V., Scambler, P. and Burriesci, G. (2010). Mitral valve dynamics in structural and fluid-structure interaction models, *Medical Engineering & Physics* **In Press, Corrected Proof**: –.

Lee, D. and Chiu, J. J. (1996). Intimal thickening under shear in a carotid bifurcation-a numerical study, *Journal of Biomechanics* **29**(1): 1–11.

Lee, K. W. and Xu, X. Y. (2002). Modelling of flow and wall behaviour in a mildly stenosed tube, *Medical Engineering & Physics* **24**(9): 575–586.

Lesoinne, M. and Farhat, C. (1996). Geometric conservation laws for flow problems with moving boundaries and deformation meshes, and their impact on aeroelastic computations, *Arteriosclerosis, Thrombosis, and Vascular Biology* **134**(1-2): 71–90.

Masud, A. and Hughes, T. J. R. (1997). A space-time Galerkin/least-squares finite element formulation of the navier-stokes equations for moving domain problems, *Arteriosclerosis, Thrombosis, and Vascular Biology* **146**(1-2): 91 – 126.

Matthies, H. G., Niekamp, R. and Steindorf, J. (2006). Algorithms for strong coupling procedures, *Computer Methods in Applied Mechanics and Engineering* **195**(17-18): 2028 – 2049. Fluid-Structure Interaction.

Merkle, C. and Athavale, M. (1987). Time-accurate unsteady incompressible flow algorithm based on artificial compressibility, *AIAA* **87**: 397–407.

Michler, C. (2005). *Efficient numerical methods for fluid-structure interaction*, PhD thesis, Delft University.

Michler, C., Hulshoff, S. J., van Brummelen, E. H. and de Borst, R. (2004). A monolithic approach to fluid-structure interaction, *Computers and Fluids* **33**: 839–848.

Mizukami, A. and Tsuchiya, M. (1984). A finite element method for the three dimensional non-steady Navier-Stokes equations, *International Journal for Numerical Methods in Fluids* **4**: 349–357.

Moens, A. (1878). *Die Pulskurve*, Brill, Leiden.

Nerem, R. M. (1992). Vascular fluid mechanics, the arterial wall, and atherosclerosis, *Journal of Biomechanical Engineering* **114**(3): 274–282.

Nobili, M., Morbiducci, U., Ponzini, R., Gaudio, C. D., Balducci, A., Grigioni, M., Montevecchi, F. M. and Redaelli, A. (2008). Numerical simulation of the dynamics of a bileaflet prosthetic heart valve using a fluid-structure interaction approach, *Journal of Biomechanics* **41**(11): 2539 – 2550.

Palatini, P. (1999). Heart rate as a risk factor for atherosclerosis and cardiovascular mortality: the effect of antihypertensive drugs, *Drugs* **57**: 713–724.

Patankar, S. V. (1980). *Numerical heat transfer and fluid flow*, Hemisphere.

Perktold, K., Peter, R. O., Resch, M. and Langs, G. (1991). Pulsatile non-newtonian blood flow in three-dimensional carotid bifurcationmodels: a numerical study of flow phenomena under different bifurcationangles, *Journal of Biomedical Engineering* **13**(6): 507–515.

Peskin, C. S. (2002). The immersed boundary method, *Acta Numerica* **11**: 479–517.

Peterson, N. (1999). An algorithm for assembling overlapping grid systems, *SIAM Journal on Scientific Computing* **20**: 1995–2022.

Peyret, R. (1976). Unsteady evolution of a horizontal jet in a stratified fluid, *Journal of Fluid Mechanics* **78**(1): 49–63.

Piperno, S. (1997). Explicit/implicit fluid/structure staggered procedures with a structural predictor and fluid subcycling for 2D inviscid aeroelastic simulations, *International Journal for Numerical Methods in Fluids* **25**: 12071226.

Piperno, S. (2001). Partitioned procedures for the transient solution of coupled aeroelastic problems - part II: Energy transfer analysis and three-dimensional applications, *Computer Methods in Applied Mechanics and Engineering* **190**: 31473170.

Piperno, S., Farhat, C. and Larrouturou, B. (1995). Partitioned procedures for the transient solution of coupled aeroelastic problems - part I: Model problem, theory and two-dimensional applications, *Computer Methods in Applied Mechanics and Engineering* **124**: 79112.

Price, J. F. (2006). Lagrangian and Eulerian representations of fluid flow: Kinematics and the equations of motion, *Technical report*, Woods Hole Oceanopraphic Institution, Woods Hole, MA.

Quan, L., Xu, X., Ben, A., Simon, A. and D. H. Alun, D. H. V. H. A. (2000). Reconstruction of blood flow patterns in a human carotid bifurcation: A combined CFD and MRI study, *Journal of Magnetic Resonance Imaging* **11**(3): 299–311.

Raback, P., Ruokolainen, J., Lyly, M. and Jarvinen, E. (2001). Fluid-structure interaction boundary conditions by artificial compressibility, *European Conference on Computational Fluid Dynamics ECCOMAS* .

Ramaswamy, B., Kawahara, M. and Nakayama, T. (1986). Lagrangian finite element method for the analysis of two-dimensional sloshing problems, *International Journal for Nmerical Methods in Fluids* **6**: 659–670.

Ramnarine, K., Hartshorne, T., Sensier, Y., Naylor, M., J.Walker, Naylor, A., Panerai, R. and Evans, D. (2003). Tissue doppler imaging of carotid plaque wall motion: a pilot study, *Cardiovascular Ultrasound* **1**(1): 17.

Richter, T. and Wick, T. (2010). Finite elements for fluid-structure interaction in ALE and fully Eulerian coordinates, *Computer Methods in Applied Mechanics and Engineering* **199**(41-44): 2633 – 2642.

Rifai, S. M., Johan, Z., Wang, W.-P., Grisval, J.-P., Hughes, T. J. and Ferencz, R. M. (1999). Multiphysics simulation of flow-induced vibrations and aeroelasticity on parallel computing platforms, *Computer Methods in Applied Mechanics and Engineering* **174**(3-4): 393 – 417.

Robinson, B. A., Batina, J. T. and Yang, H. T. Y. (1991). Aeroelastic analysis of wings using the euler equations with a deforming mesh, *Journal of Aircraft* **32**: 416–422.

Rogers, S. E., Kwak, D. and Kaul, U. (1987). On the accuracy of the pseudo-compressiblility method in solving the incompressible navier-stokes equations, *Applied Mathematical Modelling* **11**: 35–44.

Sagatun, S. I., Herfjord, K. and Holmas, T. (2002). Dynamic simulation of marine risers moving relative to each other due to vortex and wake effects, *Journal of Fluids and Structures* **16**(3): 375 – 390.

Salzar, R. S., Thubrikar, M. J., Eppink, R. T. and Richard, T. (1995). Pressure-induced mechanical stress in the carotid artery bifurcation:a possible correlation to atherosclerosis, *Journal of Biomechanics* **28**(11): 1333–1340.

Samuel, A., Jens, V., Nikolaj, E., andK. Anette, F. E.-T., William, P., Erling, F. and Kim, W. (2008). Mechanical stresses in carotid plaques using mri-based fluid-structure interaction models, *Journal of Biomechanics* **41**(8): 1651–1658.

Samuel, A. K., Jens, V. N., Anders, K. N., Anette, K., P.William, P., Erling, F. and Kim, W. Y. (2007). Stresses in carotid plaques using MRI-based fluid structure interaction models, *Proceedings of the COMSOL Users Conference 2007* .

Schneider, G. E., Raithby, G. D. and Yavanovich, M. M. (1978). Finite element solution procedure for solving the incompressible Navier-Stokes equations using order interpolation, *Numerical Heat Transfer* **1**: 435–451.

Schuster, D. M., Vadyak, J. and Atta, E. (1990). Static aeroelastic analysis of fighter aircraft using a three-dimensional Navier-Stokes algorithm, *Journal of Aircraft* **27**: 820–825.

Senes, S. (2006). How we manage stroke in Australia?, *Technical report*, Australian Institute of Health and Welfare, Canberra.

Shabana, A. (2008). *Computational continuum mechanics*, Cambridge University Press, New York, USA.

Shangguan, W. B. and Lu, Z. H. (2004). Modelling of a hydraulic engine mount with fluid-structure interaction finite element analysis, *Journal of sound and vibration* **275**(1-2): 193–221.

Silva, W. and Bartels, R. (2004). Development of reduced-order models for aeroelastic analysis and flutter prediction using the CFL3Dv6.0 code, *Journal of Fluids and Structures* **19**(6): 729 – 745.

Sinz, W. and Hermann, S. (2008). The development of a 3D-Navier-Stokes code for the simulation of an airbag inflation, *Simulation Modelling Practice and Theory* **16**(8): 885 – 899. EUROSIM 2007.

Solving FSI Applications using Workbench, ANSYS Mechanical and CFX (n.d.).

Souli, M., Ouahsine, A. and Lewin, L. (2000). ALE formulation for fluid-structure interaction problems, *Computer Methods in Applied Mechanics and Engineering* **190**(5-7): 659 – 675.

Steger, J., Dougherty, F. and Benek, J. (1983). A Chimera grid scheme, *in* K. N. Ghia and U. Ghia (eds), *ASME FED*, Vol. 5 of *Advances in Grid Generation*.

Storti, M. A., Nigro, N. M., Paz, R. R. and Dalcin, L. D. (2009). Strong coupling strategy for fluid-structure interaction problems in supersonic

regime via fixed point iteration, *Journal of Sound and Vibration* **320**(4-5): 859 – 877.

Strang, G. (2007). *Computational science and engineering*, Wellesley.

Sun, D., Owen, J. S., Wright, N. G. and Liaw, K. F. (2008). Fluid-structure interaction of prismatic line-like structures, using LES and block-iterative coupling, *Journal of Wind Engineering and Industrial Aerodynamics* **96**(6-7): 840 – 858. 5th International Colloquium on Bluff Body Aerodynamics and Applications.

Tada, T. and Tarbell, M. (2005). A computational study of flow in a compliant carotid bifurcation - stress phase angle correlation with shear stress, *Annals of Biomedical Engineering* **33**(9): 1202–1212.

Takashi, N. (1994). ALE finite element computations of fluid-structure interaction problems, *Computer Methods in Applied Mechanics and Engineering* **112**(1-4): 291 – 308.

Tallec, P. L. and Mouro, J. (2001). Fluid structure interaction with large structural displacements, *Computer Methods in Applied Mechanics and Engineering* **190**: 30393068.

Tang, D. (2004). 3D MRI-based multicomponent FSI models for atherosclerotic plaques, *Annals of Biomedical Engineering* **32**(7): 947–960.

Tang, D., Yang, C., Mondal, S., Liu, F., Canton, G., T.S.Hatsukami and Yuan, C. (2008). A negative correlation between human carotid atherosclerotic plaque progression and plaque wall stress: In vivo MRI-based 2D/3D FSI models, *Journal of Biomechanics* **41**(4): 727–736.

Tardif, J. (2009). Heart rate and atherosclerosis, *European Heart Journal Supplements* **11**: D8–D12.

Tezduyar, T., Sathe, S., Keedy, R. and Stein, K. (2006). Space-time finite element techniques for computation of fluid-structure interactions, *Computer Methods in Applied Mechanics and Engineering* **195**: 2002–2007.

Thubrikar, M. and Robicsek, F. (1995). Pressure-induced arterial wall stress and atherosclerosis, *Annals of Thoracic Surgery* **59**(6): 1594–1603.

Torii, R., Wood, N. B., Hadjiloizou, N., Dowsey, A. W., Wright, A. R., Hughes, A. D., Davies, J., Francis, D. P., Mayet, J., Yang, G.-Z., Thom, S. A. M. and Xu, X. Y. (2009). Fluid-structure interaction analysis of a patient-specific right coronary artery with physiological velocity and pressure waveforms, *Communications in Numerical Methods in Engineering* **25**: 565–580.

Valencia, A. (2006). Unsteady flow and mass transfer in models of stenotic arteries, *International Communications in Heat and Mass Transfer* **33**: 966–975.

van Brummelen, E. H. and de Borst, R. (2005). On the nonnormality of subiteration for a fluid-structure-interaction problem, *SIAM Journal on Scientific Computing* **27**: 599–621.

van Brummelen, E. H., Michler, C. and de Borst, R. (2003). Energy conservation under incompatibility for fluid-structure interaction problems, *Computer Methods in Applied Mechanics and Engineering* **192**: 2727–2748.

Vierendeels, J., Lanoye, L., Degroote, J. and Verdonck, P. (2007). Implicit coupling of partitioned fluid-structure interaction problems with reduced order models, *Computers & Structures* **85**(11-14): 970 – 976. Fourth MIT Conference on Computational Fluid and Solid Mechanics.

Wall, W. A., Forster, C., Neumann, M. and Ramm, E. (2006). Advances in fluid-structure interaction, *17th International Conference on the Application of Computer Science and Mathematics in Architecture and Civial Engineering* .

Wall, W. A., Gerstenberger, A., Gamnitzer, P., Forster, C. and Ramm, E. (2006). *Large deformation fluid-structure interaction: Advances in ALE methods and new fixed grid approaches in fluid-structure interaction: Modelling, simulation, optimization*, Springer: Berlin.

Wang, W. Q. and Yan, Y. (2010). Strongly coupling of partitioned fluid-solid interaction solvers using reduced-order models, *Applied Mathematical Modelling* **34**(12): 3817 – 3830.

Wentzel, J. J., Janssen, E., Vos, J., Schuurbiers, J. C. H., Krams, R., Serruys, P. W., de Feyter, P. J. and Slager, C. J. (2003). Extension of increased atherosclerotic wall thickness into high shear: stress regions is associated with loss of compensatory remodeling, *Circulation* **108**(1): 17–23.

Willcox, K. and Peraire, J. (2002). Balanced model reduction via the proper orthogonal decomposition, *AIAA* **40**(11): 2323–2330.

Wong, K. K. L., Mazumdar, J., Pincombe, B., Sanders, S. G. W. P. and Abbott, D. (2006). Theoretical modeling of micro-scale biological phenomena in humancoronary arteries, *Medical & Biological Engineering & Computing* **44**(11): 971–982.

Wong, K. K. L., Tu, J. Y., Mazumdar, J. and Abbott, D. (2010). Modelling of blood flow resistance for an atherosclerotic arterywith multiple stenoses and poststenotic dilatations, *ANZIAM Journal E* **51**: C66–C82.

Wood, C., Gil, A. J., Hassan, O. and Bonet, J. (2008). Partitioned block-gauss-seidel coupling for dynamic fluid-structure interaction, *Computers & Structures* **In Press, Corrected Proof**: –.

Wood, W. L., Bossak, M. and Zienkiewicz, O. C. (1981). An alpha modification of newmark method, *International Journal of Numerical Method in Engineering* **15**: 1562.

Wuchner, R., Kupzok, A. and Bletzinger, K. U. (2007). A framwork for stabilized partitioned analysis of thin membrane-wind interaction, *International Journal of Numerical Methods in Fluids* **54**: 945–963.

Wylie, E. B. and Streeter, V. L. (1983). *Fluid transients*, FEB Press, Michigan.

Xia, G. H., Zhao, Y. and Yeo, J. H. (2009). Parallel unstructured multigrid simulation of 3D unsteady flows and fluid-structure interaction in mechanical heart valve using immersed membrane method, *Computers &*

Fluids **38**(1): 71 – 79.

Xue, Y. J., Gao, P. Y., Duan, Q., Lin, Y. and Dai, C. B. (2008). Preliminary study of hemodynamic distribution in patient-specific stenotic carotid bifurcation by image-based computational fluid dynamics, *Acta Radiologica* **49**(5): 558–565.

Yamamoto, C. T., Meneghini, J. R., Saltara, F., Fregonesi, R. A. and Ferrari, J. A. (2004). Numerical simulations of vortex-induced vibration on flexible cylinders, *Journal of Fluids and Structures* **19**(4): 467 – 489.

Zarins, C. K., Giddens, D. P., Bharadvaj, B. K., Mabon, V. S. S. R. F. and Glagov, S. (1983). Carotid bifurcation atherosclerosis. quantitative correlation ofplaque localization with flow velocity profiles and wall shear stress., *Circulation Research* **53**(4): 502–14.

Zhang, L., Gerstenberger, A., Wang, X. and Liu, W. K. (2004). Immersed finite element method, *Computer Methods in Applied Mechanics and Engineering* **193**: 2051–2067.

Zhang, Q. and Hisada, T. (2001). Analysis of fluid-structure interaction problems with structural buckling and large domain changes by ALE finite element method, *Computer Methods in Applied Mechanics and Engineering* **190**(48): 6341 – 6357.

Zhao, S. Z., Ariff, B., Long, Q., Hughes, A. D., Thom, S. A., Stanton, A. V. and Xu, X. Y. (2002). Inter-individual variations in wall shear stress and mechanical stress distributions at the carotid artery bifurcation of healthy humans, *Journal of Biomechanics* **35**(10): 1367 – 1377.